
Politecnico di Torino

ScuDo
Scuola di Dottorato ~ Doctoral School
WHAT YOU ARE, TAKES YOU FAR

Doctoral Dissertation
Doctoral Program in Management, Production and Design ($38^{th}$cycle)

# Sensor-based Monitoring of Laser and Hybrid Laser–Arc Welding:

## From Process Dynamics to Component Distortions

By

**Dario Basile**

******

**Supervisor(s):**
Prof. De Maddis Manuela, Superivsor
Prof. Russo Spena Pasquale, Co-Supervisor

Politecnico di Torino
2026

# Declaration

I hereby declare that, the contents and organization of this dissertation constitute my own original work and does not compromise in any way the rights of third parties, including those relating to the security of personal data.

Dario Basile
2026

* This dissertation is presented in partial fulfillment of the requirements for **Ph.D. degree** in the Graduate School of Politecnico di Torino (ScuDo).

# Acknowledgements

I miei ringraziamenti vanno alla Prof.ssa Manuela De Maddis e al Prof. Pasquale Russo Spena, per il loro supporto durante l'intero percorso di dottorato.

Un ringraziamento speciale al Prof. Pasquale Franciosa del Laser Beam Welding Group alla WMG di Coventry, per avermi ospitato 6 mesi presso il suo laboratorio e svolgere un periodo di visiting. In quei mesi ho avuto la possibiltà di confrotnarmi con nuove realtà, lavorare con tecnologie allo stato dell'arte e espandare le mie competenze tecniche e relazionali.

Desidero ringraziare Optoprim e in particolare il Dott. Stefano Zarini per avermi offerto l'opportunità di collaborare e di svolgere parte dell'attività sperimentale di questa tesi. Questa esperienza mi ha permesso di vivere da vicino un contesto industriale reale, comprendendone meglio limiti e applicazioni rispetto ai temi di dottorato che sto approfondendo. Un ringraziamento speciale va anche ai miei amici e colleghi, Andrea e Tugay, per la loro disponibilità e il sostegno costante.

Un grosso ringraziamento va a tutti i miei colleghi dottorandi e dottorati del Politecnico di Torino, con cui ho condiviso gioie e fatiche di questo percorso: senza di loro le giornate non sarebbero state le stesse. Grazie a: Gabriel, Luigi, Danilo, Andrea, Chiara, Paolo, Alessandro.

Un enorme ringraziamento va alla mia famiglia: ai miei genitori, per aver sempre sostenuto le mie scelte e per avermi supportato, moralmente ed economicamente, con discrezione e senza mai farmelo pesare, permettendomi di concentrarmi pienamente sul mio percorso. Un grazie speciale a mia sorella Vale e a mio cognato Corrado, per il loro affetto incondizionato e la loro presenza costante, e al piccolo Edo: il regalo più bello che potessero farmi.

Infine, grazie a Beatrice, la mia compagna di vita, che mi è stata accanto fin dall'inizio di questo percorso. Con enorme pazienza ha accettato il tempo e le energie

che ho sottratto a noi, e mi ha sostenuto sempre, credendo in me e spronandomi a dare il meglio. Senza di lei, tutto questo non sarebbe stato possibile.

# Abstract

Welding is a fundamental joining technology, with estimates suggesting involvement in up to 60% of industrial manufacturing. As component complexity increases and production volumes rise, joining processes must deliver higher productivity while meeting increasingly stringent quality requirements. Laser welding and hybrid laser–arc welding are increasingly adopted in this context, offering high precision, low heat input, and excellent suitability for automation in high-throughput manufacturing. In parallel, industrial quality assurance is trending toward higher inspection coverage (up to 100% in some applications). Achieving such coverage solely through offline non-destructive testing is costly and slow, motivating in-process sensing and real-time monitoring to reduce scrap, rework, and inspection effort. At the same time, multiple coupled physical mechanisms govern these processes, making weld-quality variations difficult to interpret and attribute to a single cause.

Monitoring systems are typically based on measurable process signals, including optical, acoustic, and thermal responses. Weld quality is governed by phenomena spanning multiple length and time scales: different mechanisms dominate from the process zone to the component level, and no single observable is sufficient to characterise quality. Accordingly, this thesis develops and validates in-process monitoring strategies for laser and hybrid laser–arc welding through three complementary case studies spanning local process behaviour, weld-section integrity, and component-level dimensional response, and evaluates whether acoustic, optical, and thermal sensing can provide quantitative, application-relevant indicators suitable for production-oriented monitoring.

At the process scale, a membrane-free optical microphone was used to monitor remote laser welding of AA1050 aluminium overlap joints, demonstrating sensitivity to keyhole-regime transitions, including blind-to-passing-through keyhole; feature-level fusion with photodiode spectral emissions provided complementary

information but did not consistently outperform acoustic features alone. At the weld-section scale, OCT enabled in-situ penetration-depth monitoring in hybrid laser–arc welding of S355 steel, capturing depth trends up to an effective depth of $\sim$6 mm. At the component scale, infrared thermography provided in-process thermal histories that constrained a thermo-mechanical FEM model, enabling prediction of angular distortion in thin aluminium welding with errors below 0.3% for representative conditions.

Overall, the results show that quantitative monitoring outputs can be obtained across complementary decision levels and can support a more comprehensive assessment of weld quality than single-sensor monitoring alone. The thesis provides validated workflows and operating envelopes and complements the technical results with a deployment-oriented discussion of industrial applicability, scalability, and limitations, laying the groundwork for future integrated monitoring and, where feasible, closed-loop quality control.

# Contents

# List of Figures

# List of Tables

# Nomenclature

### Abbreviations

| | |
|---|---|
| *CW* | Continuous Wave |
| *GMAW* | Gas Metal Arc Welding |
| *GTAW* | Gas Tungsten Arc Welding |
| *HLAW* | Hybrid Laser-Arc Welding |
| *LW* | Laser Welding |
| IR | Infrared |
| ML | Machine Learning |
| NDT | Non-Destructive Testing |
| NIR | Near Infrared |
| OCT | Optical Coherence Tomography |
| UV | Ultraviolet |
| VIS | Visible Light |

### Symbols

| | |
|---|---|
| $p_{\sigma}$ | Standard deviation feature from the plasma emission signal |
| $p_{IQR}$ | Interquartile range (IQR) feature from the plasma emission signal |
| $p_{kurt}$ | Kurtosis feature from the plasma emission signal |

$p_{MAD}$ Median Absolute Deviation (MAD) feature from the plasma emission signal

$p_{mean}$ Mean value feature from the plasma emission signal

$p_{median}$ Median value feature from the plasma emission signal

$p_{mode}$ Mode feature from the plasma emission signal

$p_{skew}$ Skewness feature from the plasma emission signal

$p_{STE}$ Short-Time Energy (STE) feature from the plasma emission signal

$p_{ZCR}$ Zero Crossing Rate (ZCR) feature from the plasma emission signal

$r_{\sigma}$ Standard deviation feature from the back-reflection signal

$r_{IQR}$ Interquartile range (IQR) feature from the back-reflection signal

$r_{kurt}$ Kurtosis feature from the back-reflection signal

$r_{MAD}$ Median Absolute Deviation (MAD) feature from the back-reflection signal

$r_{mean}$ Mean value feature from the back-reflection signal

$r_{median}$ Median value feature from the back-reflection signal

$r_{mode}$ Mode feature from the back-reflection signal

$r_{skew}$ Skewness feature from the back-reflection signal

$r_{STE}$ Short-Time Energy (STE) feature from the back-reflection signal

$r_{ZCR}$ Zero Crossing Rate (ZCR) feature from the back-reflection signal

$s_{\sigma}$ Standard deviation feature from the acoustic emission signal

$s_{IQR}$ Interquartile range (IQR) feature from the acoustic emission signal

$s_{kurt}$ Kurtosis feature from the acoustic emission signal

$s_{MAD}$ Median Absolute Deviation (MAD) feature from the acoustic emission signal

$s_{mean}$ Mean value feature from the acoustic emission signal

$s_{median}$ Median value feature from the acoustic emission signal

$s_{mode}$ Mode feature from the acoustic emission signal

$s_{p,0\text{-}8}$ Spectral power feature of the acoustic emission signal in the 0–8 band

$s_{p,26\text{-}end}$ Spectral power feature of the acoustic emission signal in the 26–end band

$s_{p,8\text{-}26}$ Spectral power feature of the acoustic emission signal in the 8–26 band

$s_{p,\text{filt}}$ Power feature of the filtered acoustic emission signal

$s_p$ Total spectral power feature of the acoustic emission signal

$s_{skew}$ Skewness feature from the acoustic emission signal

$s_{STE}$ Short-Time Energy (STE) feature from the acoustic emission signal

$s_{ZCR}$ Zero Crossing Rate (ZCR) feature from the acoustic emission signal

$z_{OCT}$ Weld depth measured by OCT

$\alpha$ Laser beam inclination

$\beta$ GMAW torch inclination

$\theta$ Divergence angle

$A$ Absorptivity

$BPP$ Beam Parameter Product

$D_f$ Diameter of optical fiber

$D_{LT}$ Distance between laser beam and GMAW torch

$f_c$ Focal length of collimating lens

$f_F$ Focal length of focusing lens

$P_L$ Laser Power

$R$ Reflectivity

$v$ Welding Speed (mm/s)

$w(z)$ Beam waist radius at a given $z$

| | |
|---|---|
| $w_0$ | Minimum beam waist radius |
| $z_R$ | Rayleigh length |
| LoC | Lack of Connection |
| LoF | Lack of Fusion |
| LSW | Local Support Algorithm |
| MAD | Median absolute deviation |
| ROI | Region of Interest |
| SNR | Signal-to-Noise Ratio |
| SoC | Sound Connection |

# Chapter 1

# Introduction

## 1.1 Background and motivation

Welding is a permanent joining process that plays a crucial role across many industrial sectors, including automotive, aerospace, energy, infrastructure, shipbuilding, oil&gas pipelines, and electronics. Industry and government sources estimate that more than 50 % of manufactured items depend on welding at some stage in their production, underlining its importance for industrial value generation [1]. Recent market analyses estimate the global welding market at about USD 10.7 billion in 2024, with projected growth to roughly USD 17.7 billion by 2034. Demand is concentrated in a few application areas: construction accounts for approximately 21 % of global welding consumables (2024), automotive for around 30 %, and oil&gas for about 15 %, with the remainder distributed across heavy machinery, shipbuilding, aerospace, and electronics [2].

Among the various welding technologies, laser-based welding has attracted significant attention owing to its high productivity, ease of automation, and ability to deliver high-quality joints. Laser welding provides a highly concentrated and precisely controllable heat source, which enables high welding speeds, small heat-affected zones, and reduced distortion. These characteristics make laser welding particularly attractive for applications with stringent dimensional tolerances and tight quality requirements. In the automotive sector, for example, laser welding is widely used in body-in-white production and is increasingly adopted for the manufacturing

of components for electric vehicles, where repeatability, throughput, and pack-level dimensional control are critical [3].

To extend the applicability of laser-based processes to thicker sections and more demanding joint configurations, hybrid strategies have been developed that combine lasers with conventional arc welding processes. Hybrid laser–arc welding (HLAW), which couples a laser beam with a gas metal arc, enables higher penetration depths, improved gap-bridging capability, and stabilised molten pool behaviour. This process is used, for instance, in the welding of heavy-plate steels for shipbuilding, offshore structures, and oil&gas pipelines. HLAW can also reduce filler wire consumption and improve overall process efficiency compared with conventional arc welding alone, contributing to more sustainable fabrication [4].

Sustainability requirements further increase the need to optimise manufacturing processes. The iron and steel sector accounts for about 8% of global final energy demand and roughly 7% of energy-sector $CO_2$ emissions, corresponding to around 2.6,Gt,$CO_2$/year. To meet decarbonisation goals such as the European Green Deal, emissions from steel production must decrease substantially in the coming decades. Beyond changes in primary steelmaking and improved material efficiency, downstream processes—including welding—also matter: more stable and productive welding with fewer defects reduces rework and scrap, lowers the use of consumables, and can reduce fume generation, leading to measurable energy and emissions savings when applied at industrial scale.

In this context, maintaining tight control over welding processes becomes essential. Robust process control minimises scrap and rework, lowers energy and filler consumption, and stabilises dimensional quality, thereby improving yield, cost-effectiveness, and sustainability. Traditional non-destructive testing (NDT) methods, however, are typically applied offline and on a sampling basis. They provide only after-the-fact assessment and limited visibility into transient process instabilities or parameter drifts. As a result, defects may propagate through a large number of welds before they are detected, driving rework, delays, and cost.

By contrast, modern in-process sensing offers the possibility to observe the weld in real time, detect instabilities, and ultimately enable closed-loop control. A variety of sensing modalities—such as photodiodes, acoustic sensors, optical coherence tomography (OCT), and vision or thermographic systems—can capture process emissions related to plume dynamics, keyhole behavior, penetration depth, and

thermal fields. Appropriate signal processing and decision logic can then translate these emissions into qualitative and quantitative indicators of weld quality and process stability.

Laser- and hybrid laser–arc welding are governed by strongly coupled thermal, fluid-flow, and metallurgical phenomena. Consequently, weld quality does not depend on a single observable, but emerges from mechanisms acting at different spatial and temporal scales: short-lived process instabilities influence local defect formation, weld-section geometry governs joint integrity, and the accumulation of thermal strains drives component-scale distortion. From an industrial perspective, monitoring must therefore provide indicators that are not only physically meaningful, but also actionable for reducing scrap, rework, and reliance on offline inspection.

To motivate the multi-scale approach adopted in this thesis, three representative application contexts are considered.

**Local process scale: EV battery interconnections** Battery-module manufacturing involves very high weld counts, while inspection is often based on sampling and/or destructive testing. In this setting, even rare instabilities can translate into a non-negligible number of weak or defective joints. In-process monitoring at the local scale is therefore needed to detect keyhole-regime changes and transient disturbances as they occur, enabling immediate screening of welds and reducing downstream rework.

**Weld-section scale: penetration in pipe and panel welding** In thick-section steel fabrication, hybrid laser–arc welding is adopted for productivity, but quality is highly sensitive to penetration and fusion along the joint. Deviations in fit-up or heat input can create local lack-of-fusion regions that may be costly to repair if detected late. Direct in-process estimation of weld geometry—in particular penetration depth—can reduce inspection burden and mitigate the risk of late defect discovery.

**Component scale: distortion in panel and module fabrication** Even when weld quality is sound, accumulated thermal can cause thermal strains leading to out-of-tolerance distortion in thin plates and assemblies, driving straightening operations or scrapping of large components. While thermo-mechanical simulation can predict distortion, industrial adoption is limited by the effort required to calibrate and validate

thermal inputs. In this context,, feeding calculators with thermal measurements offers a route to efficient and reliable distortion prediction, supporting reduced correction work and improved dimensional yield.

These examples motivate the need for monitoring strategies that deliver quantitative indicators across complementary scales, linking process signatures to weld integrity and component-level performance.

Despite substantial technical progress, the adoption of in-process monitoring in real production contexts remains limited. A primary barrier is the limited evidence base: comparatively few studies quantify robustness, false-alarm rates, and reliability across materials, optics, joint geometries, and parameter windows, and production-oriented evaluations are especially scarce for hybrid laser–arc welding. In the absence of validated performance metrics, decision thresholds, and practical qualification guidance, manufacturers face integration risk (e.g. nuisance alarms and process interruptions) and lack clear acceptance criteria. This motivates the validation-focused monitoring workflows developed in this thesis.

## 1.2 Objectives of the thesis

The overall objective of this thesis is to develop and validate in-process monitoring strategies for laser and hybrid laser–arc welding in an industrial context, addressing increasingly stringent quality requirements in high-throughput manufacturing. The work aims to translate multi-modal process observations (acoustic, optical and thermal) into quantitative, application-relevant indicators of weld quality and process stability that can support reduced scrap, rework, and reliance on offline inspection.

The specific objectives are:

- to design practical signal-processing and feature-extraction pipelines that yield robust monitoring outputs under industrial constraints (e.g. process variability, optical disturbances, and measurement noise);
- to quantify the performance and limitations of selected sensing modalities, and to assess whether multi-sensor integration provides complementary information compared with single-sensor monitoring;

- to validate monitoring outputs against appropriate reference measurements (e.g. metallography and dimensional metrology), defining operating envelopes and error bounds suitable for qualification;
- to provide experimentally grounded workflows and decision metrics that can inform the deployment of monitoring systems and constitute a basis for future closed-loop quality control.

### 1.2.1 Research question

The overarching research question addressed in this thesis is:

> **RQ:** To what extent can acoustic, optical, and thermal sensing be translated into robust, quantitative, and industrially actionable indicators of weld quality and process stability in laser and hybrid laser–arc welding?

This overall question is decomposed into the following sub-questions:

- **RQ1:** What information on process stability and keyhole-regime transitions can be extracted from acoustic and optical emissions during remote laser welding of thin aluminium sheets?
- **RQ2:** Under which process conditions and configurations can optical coherence tomography provide accurate and reliable in-situ measurements of penetration depth during hybrid laser–arc welding of steels?
- **RQ3:** Can infrared thermography provide in-process thermal constraints that enable reliable thermo-mechanical prediction of welding-induced distortion?

### 1.2.2 Scope and case studies

Motivated by the identified gaps and guided by RQ and RQ1–RQ3, this thesis is organised around three case studies that address monitoring tasks in laser-based welding:

- **Case study 1 (local process scale):** Investigation of an *optical microphone* for monitoring remote laser welding of thin aluminium busbars, representative of EV battery interconnections. Acoustic emissions are analysed to detect power variations and part-to-part gap conditions, and their combination with optical emissions from photodiodes is explored to improve defect classification.
- **Case study 2 (weld-section scale):** Evaluation of *optical coherence tomography (OCT)* for in-situ monitoring of penetration depth in hybrid laser–arc welding of structural steels. The study assesses the influence of process parameters and arc-related disturbances on OCT signal quality and quantifies the achievable accuracy and robustness of weld-depth measurements.
- **Case study 3 (component scale):** Development of a *thermography-assisted modelling* approach in which infrared thermal camera measurements of the weld thermal field are used to constrain finite element (FE) simulations for predicting welding-induced distortions in laser-welded thin plates. The focus is on leveraging measured thermal histories to define physically grounded thermal constraints while maintaining acceptable predictive accuracy relative to conventional simulation workflows.

Together, these case studies delineate the scope of the thesis and provide evidence on the feasibility, benefits, and limitations of the considered sensing approaches in manufacturing-relevant scenarios.

## 1.3 Thesis progression and structure

The remainder of this dissertation is organised as follows:

- **Chapter 2** introduces the fundamentals of laser welding and hybrid laser–arc welding, including process physics, common joint configurations, and typical weld defects relevant to monitoring.
- **Chapter 3** reviews process emissions and in-line monitoring approaches for laser-based welding. It presents the working principles, advantages, and limitations of the sensing technologies considered in this thesis, namely acoustic sensing (optical microphone), photodiode-based optical emissions, OCT, and infrared thermography.

- **Chapter 4** presents Case study 1 on remote laser welding of thin aluminium overlap joints, showing how acoustic and optical emissions can be processed into indicators of process stability and keyhole-regime transitions.
- **Chapter 5** presents Case study 2 on hybrid laser–arc welding of steel, evaluating OCT-based in-situ penetration-depth monitoring and its reliability under representative configurations and disturbances.
- **Chapter 6** presents Case study 3 on thin aluminium laser welding, where infrared thermography is used to extract thermal histories that constrain a thermo-mechanical finite-element model for distortion prediction.
- **Chapter 7** provides a cross-case discussion, gives consolidated answers to the research questions, and examines industrial applicability and scalability. It includes a scenario-based cost analysis for deploying a full monitoring framework across the three application contexts and discusses practical deployment constraints and limitations.
- **Chapter 8** concludes the thesis by summarising the main contributions and findings, outlining the principal limitations of the work, and highlighting priorities for future developments toward integrated, production-ready monitoring frameworks.

# Chapter 2

# Laser beam welding process

## 2.1 Fundamentals of Lasers

LASER ("Light Amplification by Stimulated Emission of Radiation") denotes a light source based on optical amplification through stimulated emission of electromagnetic radiation, where the emitted energy is carried by discrete packets called photons [5].

Laser radiation is an electromagnetic wave in which energy is associated with mutually orthogonal electric ($E$) and magnetic ($H$) fields that vary in space and time. Such waves are characterised by wavelength ($\lambda$), phase ($\phi$), and amplitude ($A$), as illustrated in Figure 2.1. Lasers are often classified by their emission wavelength, which typically falls in the ultraviolet (UV), visible (VIS), or infrared (IR) ranges (Figure 2.2).

Compared with diffuse light sources (e.g. incandescent lamps), laser beams can be delivered and focused with high precision because of three intrinsic properties: high monochromaticity, high coherence, and low divergence.

Laser generation requires (i) a gain medium, where population inversion is established by a pumping mechanism, and (ii) an optical resonator that provides feedback by reflecting light back and forth through the medium, enabling amplification.

A simplified schematic of the generation mechanism is shown in Figure 2.3. Pumping excites electrons in the gain medium to higher energy states. As these excited states relax, photons are emitted; through stimulated emission, additional photons are generated with the same phase and direction. Multiple passes between

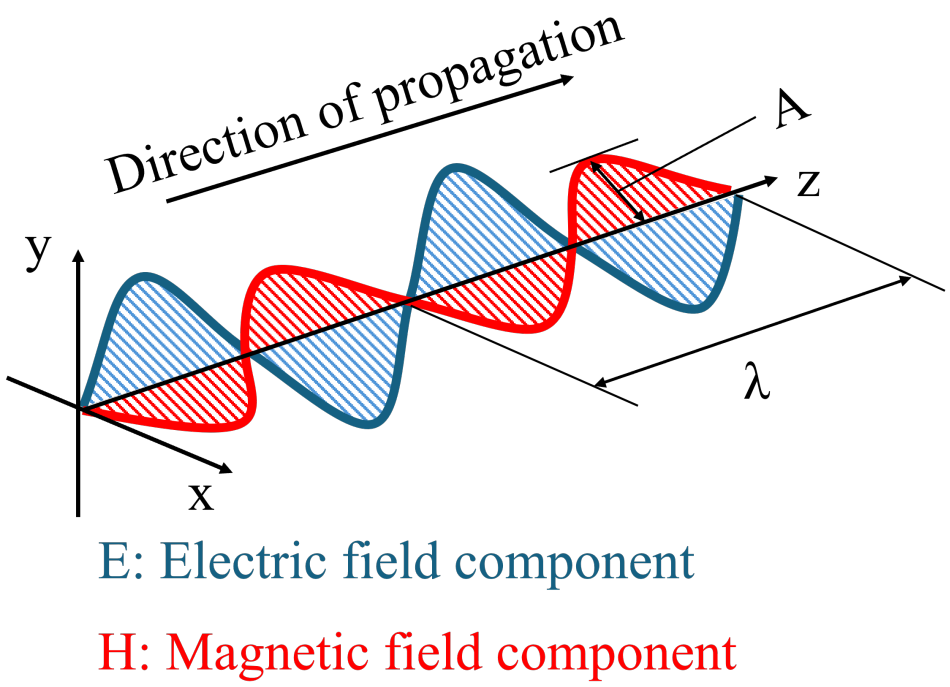


Fig. 2.1 Electromagnetic wave scheme.

the cavity mirrors amplify the radiation, and a fraction exits through a partially reflective mirror as the laser beam [5].

Lasers can also be classified by the nature of the gain medium, pumping mechanism, and resonator design (e.g. solid-state, diode, fibre, and gas lasers). The selection of a specific source depends on the application constraints, including the material to be processed, required penetration depth, and economic considerations.

Once generated, the beam must be delivered to the processing head. For $CO_2$ lasers, beam delivery is typically realised through mirror-based beam paths, whereas many other sources can be coupled into optical fibres and guided directly to the head. There, optical elements collimate and focus the beam to a small spot, creating a high power-density heat source.

Figure 2.4 shows a conventional fibre-delivered configuration: the fibre output is collimated by a lens and then focused by a second lens to achieve the desired spot size at the workpiece. Under a geometrical approximation, the minimum beam-waist

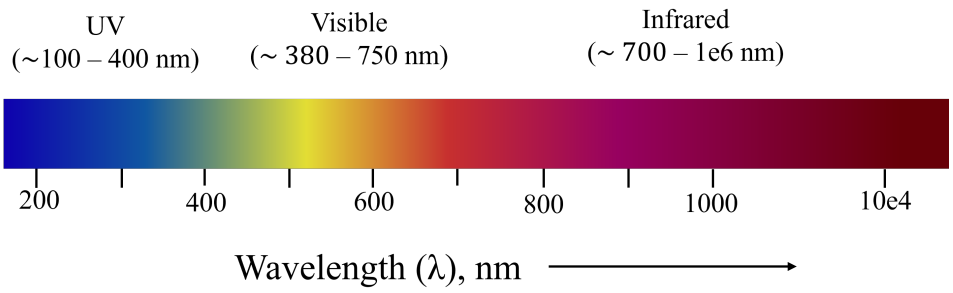


Fig. 2.2 Electromagnetic spectrum.

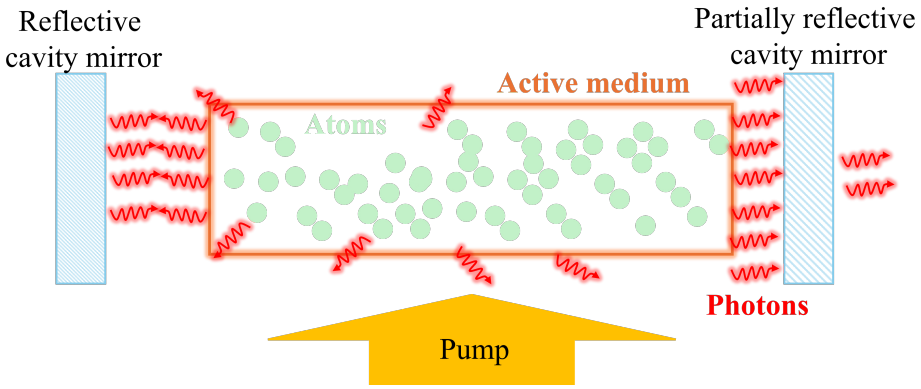


Fig. 2.3 Simplified scheme of laser-beam generation in an optical cavity.

radius $w_0$ scales with the fibre core diameter $D_f$ and the telescope magnification $f_F/f_c$ as

$$w_0 = \frac{f_F}{f_c} D_f. \tag{2.1}$$

Beam propagation is commonly described through the beam parameter product (BPP),

$$BPP = w_0\,\theta, \tag{2.2}$$

where $\theta$ is the beam divergence half-angle. Lower BPP corresponds to higher beam quality (i.e. tighter focusing for a given divergence). The depth of focus is characterised by the Rayleigh length $z_R$: for a Gaussian beam, $z_R$ is the distance from the waist at which the beam radius increases by a factor $\sqrt{2}$, corresponding to

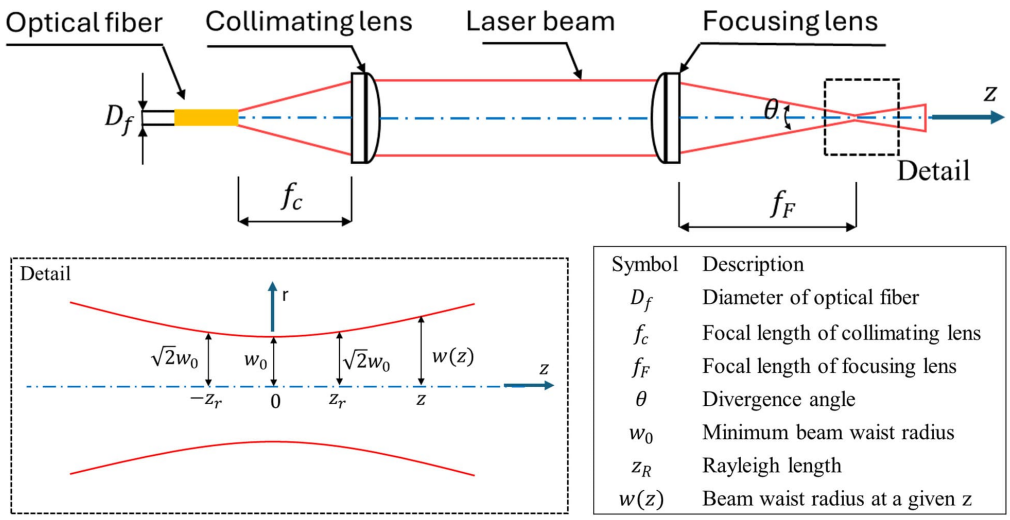


Fig. 2.4 Schematic of a typical laser-beam focusing system.

a doubling of the beam cross-sectional area. Within this region, the beam remains tightly focused.

A larger focal spot can be obtained by increasing the effective magnification $f_F/f_c$ or by using a fibre with a larger core diameter, although these choices typically require larger optics and may reduce achievable power density. As indicated in Figure 2.4, the transverse intensity profile is well approximated by a Gaussian distribution, narrowing towards the waist and diverging symmetrically with propagation distance.

$$\Delta f_F \approx \left(\frac{f_F}{f_c}\right)^2 \Delta f_c. \tag{2.3}$$

## 2.2 Laser welding

In material processing, lasers enable a range of thermal operations, including surface texturing, hardening, welding, and cutting. This section summarises the fundamentals of laser welding, which is the exclusive focus of this thesis.

In laser welding, a focused beam impinges on the workpiece and the absorbed energy generates intense local heating. Depending on the delivered power density and interaction time, the material can melt and partially vaporise, producing a molten

pool and, in some conditions, a vapour cavity. During the laser–material interaction, multiple coupled phenomena occur simultaneously, including heat conduction, fluid flow within the molten pool, evaporation, and plume/plasma formation.

Laser welding is commonly described in three interaction regimes as a function of power density and coupling conditions: conduction mode, transition (conduction–keyhole) mode, and keyhole mode.

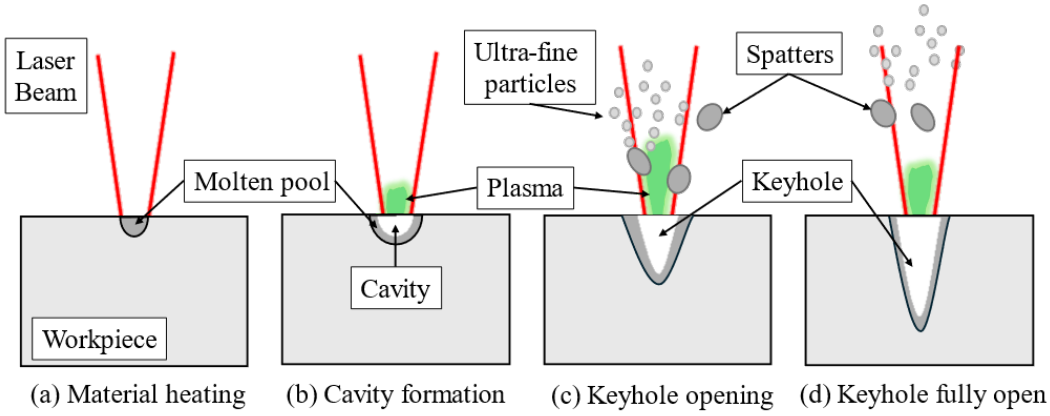


Fig. 2.5 Laser–material interaction phases.

In conduction mode, the power density is relatively low: the surface is heated and thermal energy diffuses into the bulk mainly by conduction. Melting is shallow and the pool is typically wide with a low aspect ratio. In the transition regime, a vapour depression may form intermittently and deepen locally; penetration increases, but the cavity is not yet fully stable. In keyhole mode, recoil pressure from evaporation sustains a narrow vapour cavity. Multiple internal reflections inside the cavity enhance absorption, enabling deep and narrow penetration with a high aspect ratio. The phases sketched in Figure 2.5 (absorption, melting, vapour depression, plume/plasma formation, and solidification) occur with different relative importance depending on the regime [5–7].

During laser welding, process parameters influence molten-pool dynamics as well as the resulting joint geometry and quality, and their effects are strongly coupled through the underlying thermo-fluid phenomena. Restricting the discussion to continuous-wave (CW) operation, the main parameters are:

- *Laser power* ($P_L$): optical power delivered to the workpiece;
- *Welding speed* ($v$): relative travel speed of the beam over the joint;

- *Focal position* ($f_F$): location of the focus relative to the workpiece surface;
- *Shielding gas* (type and flow rate): typically argon, helium, or mixtures, affecting plume behaviour, oxidation, and spatter.

Many defects in laser welding arise from the same mechanisms that govern energy coupling and the stability of the conduction–keyhole transition. In conduction/transition regimes, insufficient heat input and unfavourable coupling or surface conditions can lead to lack of fusion and lack of penetration. Surface-profile defects such as underfill and undercut are often associated with unbalanced melt flow and solidification at the top and bottom surfaces. In keyhole-mode welding, volumetric porosity is commonly linked to unstable cavity dynamics and gas entrapment. Keyhole blowout and plume-driven events can generate spatter, which may damage both the workpiece and protective optics. At higher travel speeds, periodic bulging and rippling can occur when the molten pool cannot provide sufficient support before solidification. In thin sections, excessive penetration can result in root collapse or drop-out. High thermal gradients and alloy sensitivity increase susceptibility to metallurgical cracking (e.g. hot/solidification cracking), while oxidation or discolouration typically indicates insufficient shielding. Selecting process parameters that mitigate these mechanisms while meeting joint requirements is therefore a central challenge when qualifying laser-welding procedures across different materials and operating envelopes [5–8].

## 2.3 Hybrid Laser–Arc Welding

Hybrid laser–arc welding (HLAW) combines a high-power laser and an electrical arc to generate a coupled thermal interaction in which both sources contribute to a single weld pool. In the hybrid regime, the keyhole, arc plasma, and molten-pool flow interact thermally and electromagnetically, enabling process windows that are not achievable with either source alone. Although the concept was investigated already in the 1970s, HLAW became commercially viable mainly with the availability of high-power solid-state and fibre lasers from the early 2000s; early industrial uptake is reported in heavy fabrication, including oil-tank production [9].

HLAW combines the laser's high energy density and penetration capability with the arc's filler addition and gap-bridging capacity. Compared with conventional

arc welding, reported benefits include higher productivity and reduced overall heat input, with demonstrated applicability to steels, aluminium alloys, magnesium alloys, and nickel-based alloys [4]. These characteristics have supported adoption across several sectors. In automotive manufacturing, HLAW has been applied to body-in-white assemblies to increase productivity and reduce filler consumption while maintaining joint quality [10]. In shipbuilding, it is used on large structural panels to limit distortion and reduce post-weld rectification and rework [11]. In energy and heavy manufacturing, including boiler, pressure-vessel, and pipeline fabrication, HLAW is attractive for thick-section joints due to its penetration capability and potential for shorter production cycles [12]. Aerospace and rail applications also report consistent weld quality in lightweight materials while preserving mechanical performance [13, 14].

HLAW can operate in configurations ranging from *pure hybrid* to more *tandem-like* behaviour, depending primarily on the spatial offset between the laser spot and the arc (and thus on the extent to which both sources act on the same molten pool).

Figure 2.6 illustrates the working principle of HLAW.

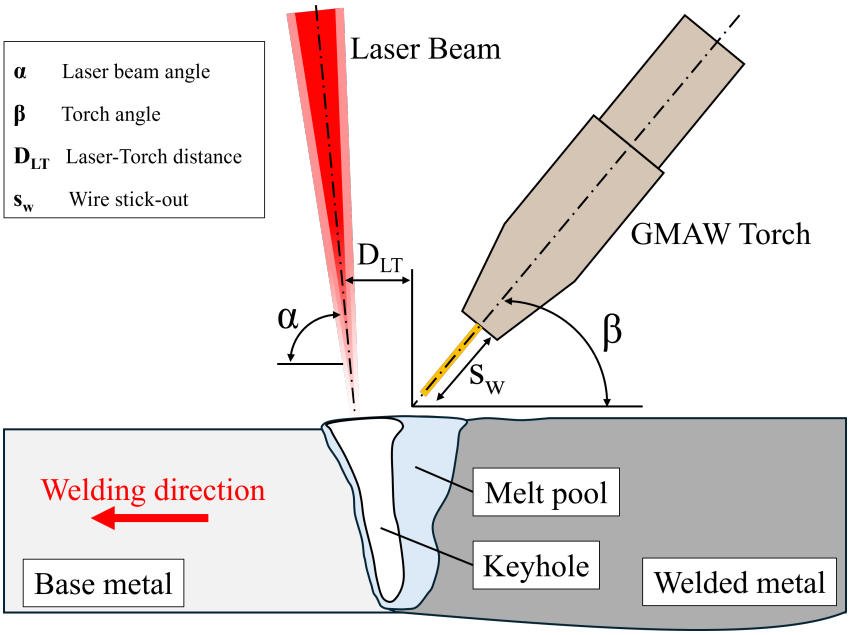


Fig. 2.6 Schematic of HLAW.

In a *pure hybrid* arrangement, the laser and arc are positioned in close proximity (often characterised by a laser–torch distance $D_{LT} \leq 3$ mm), so that both sources act on a common molten pool. Under these conditions, mutual interaction is strongest:

arc-related effects can increase the effective laser coupling, while the laser-induced vapour depression and recoil pressure influence arc attachment and pool dynamics. The resulting weld pool combines the laser's deep, narrow penetration with the broader melt region and filler contribution of the arc, improving wetting and gap tolerance.

In a *tandem* configuration, the sources are separated by a larger offset (typically $D_{LT} > 6$ mm), and they tend to act on distinct melt regions. Although synergy is reduced, the separation allows more independent tuning of each source—for example, using the laser primarily for penetration and the arc primarily for deposition and gap bridging—which can be advantageous for thicker sections, complex joint geometries, and larger joint gaps [15–17].

Industrial implementations include pairings such as $CO_2$-laser/MAG, fibre-laser/MAG, and Nd:YAG-laser/TIG. System layouts span coaxial configurations, which simplify alignment by combining laser and arc axes, and paraxial configurations, which allow flexible spatial offsets between the sources [4]. Directionality also affects performance: laser-leading configurations generally favour penetration, whereas arc-leading configurations are often preferred for gap filling, particularly for thinner or more sensitive materials such as aluminium alloys [18].

The coupled interaction modifies energy deposition relative to the standalone processes. For example, arc plasma and plume dynamics can alter laser coupling, while laser-induced recoil pressure can influence arc constriction and heat distribution in the pool. As a result, the temperature field and flow can exhibit a combined behaviour in which deep penetration is sustained while the arc contribution improves side-wall wetting and joint-gap tolerance [19].

In addition to the parameters relevant to laser welding, HLAW requires consideration of arc-specific and coupling-related parameters, including:

- **Wire feed rate:** controls deposition rate and influences melt-pool volume and bead shape.
- **Relative positioning of torch and laser (offset $D_{LT}$ and orientation):** affects heat distribution and the degree of interaction; laser-leading tends to favour penetration, while arc-leading improves gap bridging.

- **Torch angle:** influences arc deflection and arc attachment, thereby affecting coupling conditions and weld-pool flow.
- **Filler material:** affects metallurgy, mechanical properties, and susceptibility to defects (e.g. cracking and porosity).

# Chapter 3

# Monitoring of Laser Welding Processes

The demand for reduced manufacturing lead times and improved welding quality has driven the development of non-destructive testing (NDT) and monitoring techniques aimed at detecting welding defects in real time and enabling automated quality assessment [20, 21]. In production, this need is amplified by high weld counts and tight quality requirements, which make purely offline inspection costly and slow.

Figure 3.1 illustrates a typical integration of monitoring functions within a laser-welding line. Monitoring can be organised into three stages: *pre-process*, *in-process*, and *post-process*. Pre-process sensing supports seam tracking and joint preparation control (e.g. gap and misalignment), ensuring correct beam positioning. Post-process sensing assesses the final weld condition, including surface and internal defects such as porosity, cracking, and geometric imperfections [22]. In all cases, the aim is to translate sensor outputs into a clear quality decision, as exemplified by the dashboard concept in Figure 3.1.

This thesis focuses on *in-process* monitoring, i.e. the analysis of process emissions and sensor signals acquired while welding is ongoing. The goal is to extract indicators of process stability and deviations from quality standards that can support real-time or near-real-time actions such as intervention, early rejection, or targeted follow-up inspection, depending on the manufacturing context [23].

In laser welding, monitoring commonly aims to distinguish the operating regime (conduction/transition/keyhole) and to detect transient instabilities that can precede

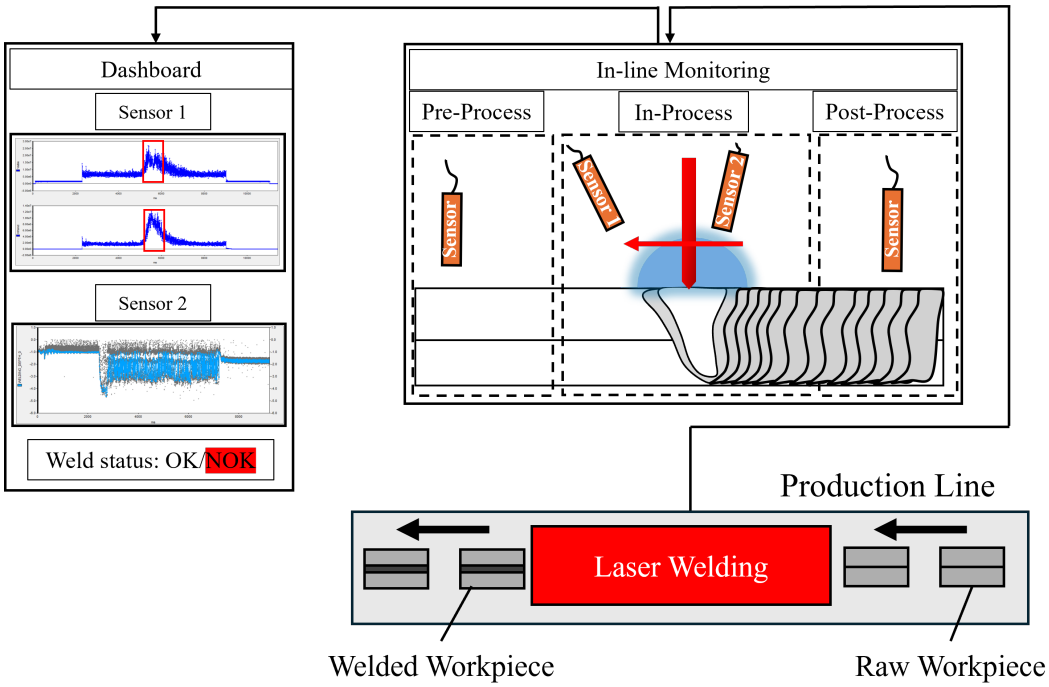


Fig. 3.1 Example of monitoring concept during a laser welding process.

defects. Depending on the application, targets include internal quality (e.g. instability signatures linked to porosity), weld geometry and penetration state, and surface integrity (e.g. surface profile irregularities or oxidation). Thermal indicators are also used to track heat input and cooling behaviour, which are relevant to distortion and, in susceptible alloys, to cracking driven by thermal strains. In addition, deviations in surface condition (e.g., contamination or edge misalignments) may be monitored indirectly because they can affect coupling and promote inclusions or violent ejection events [24].

A useful distinction is between *direct* measurements, which provide geometrically or physically interpretable quantities in metric units, and *indirect* measurements, which capture process emissions that must be correlated to weld states or defects through signal processing and/or feature extraction [25]. Indirect monitoring is often implemented through process-emission sensing: photodiodes capture optical radiance variations from the interaction zone, while acoustic sensing captures airborne or structure-borne signatures linked to keyhole dynamics and transient events. Direct monitoring is pursued through geometric or field measurements: coherent metrology (notably OCT) can provide weld-depth-related observables [26], and

infrared thermography provides access to the surface temperature field for heat-input- and cooling-related indicators [27]. Camera-based monitoring provides spatially resolved surface observations of the melt pool, plume/spatter, and seam appearance [28].

A more detailed discussion of process emissions and the working principles of the sensors used in this thesis is provided in Sections 3.1 and 3.2.

Most monitoring systems follow a common pipeline: acquisition, preprocessing, feature extraction, and decision-making. Preprocessing typically includes synchronisation with the weld cycle, time-windowing, filtering and outlier handling, and normalisation relative to baseline conditions. Feature extraction then compresses the signal into a small set of descriptors computed over short windows (e.g. band-power, intensity ratios, dispersion metrics, or ROI-based thermal features), which are mapped to decisions using either threshold-based logic or supervised models. In practice, robustness is improved by adding a signal-validity check ("quality gate") and periodic baseline monitoring to reduce nuisance alarms and detect sensor degradation [25].

Figure 3.2 illustrates a simple example of threshold-based monitoring, where a stable trace is classified as acceptable and a transient deviation triggers a reject decision.

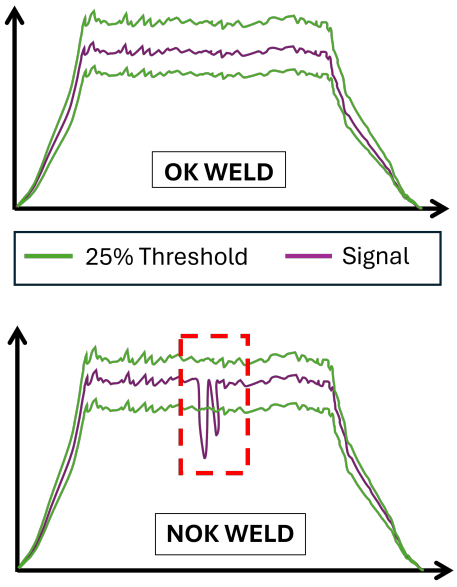


Fig. 3.2 Illustrative example of threshold-based in-process monitoring

Compared with laser welding, hybrid laser–arc welding introduces additional disturbances due to arc plasma, droplet transfer, and increased spatter and fume generation. This can degrade optical-path stability and increase the burden on optics protection and filtering. The monitoring literature for HLAW is less extensive, and many studies focus on surface-observable monitoring (often camera-based) [28, 29].

## 3.1 Process emissions

### 3.1.1 Acoustic emissions

During laser welding, acoustic emissions (AE) arise from multiple coupled sources, including keyhole dynamics, rapid vaporisation, and plume-related phenomena, and are generally associated with localised energy release [30]. A dominant contribution is often attributed to keyhole fluctuations and intermittent collapses, which generate pressure waves that propagate through the surrounding medium (airborne AE) or the structure (structure-borne AE). Reported characteristic frequency content varies across studies and depends on material and process regime; theoretical models have suggested natural frequencies on the order of kHz, while experimental measurements frequently report dominant bands in the low-kHz range [31–34]. Importantly, the spectrum captured by microphones also reflects coupling conditions, resonances, boundary effects, and the measurement setup. As noted in the literature, significant AE generation may occur when keyhole geometry and pressure conditions support resonance behaviour (e.g. cavity-like response) [35]. Additional AE contributions can originate from plume dynamics and surface evaporation events [36, 37]. Overall, AE signals represent a convolution of process events and system transfer functions, which motivates careful feature design and validation.

### 3.1.2 Optical emissions

When a laser beam interacts with a metal surface, a fraction of the incident radiation is absorbed while the remainder is reflected. The absorbed energy drives melting and, at sufficiently high power density, evaporation and keyhole formation [24]. Vapour and ejected particles form a luminous plume above the interaction zone, which contributes to the measured optical emissions [7]. In monitoring practice,

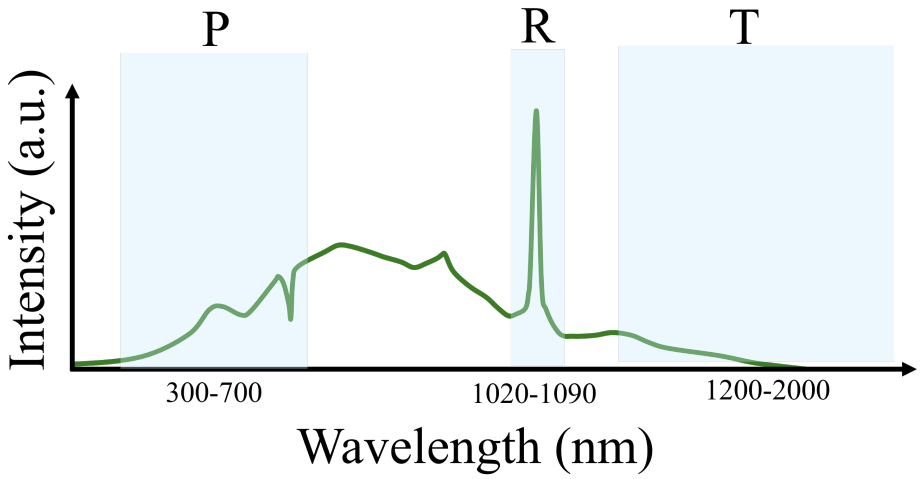


Fig. 3.3 Typical intensity distribution and wavelength ranges of electromagnetic emissions.

optical signals are typically acquired using photodiodes (often with optical filters) or spectrometers, and their temporal evolution is used as an indirect indicator of coupling conditions, keyhole/plume behavior, and process stability.

Optical signals measured during laser welding generally contain multiple contributions. A broadband component is associated with thermal radiation from the hot workpiece and melt pool, while plume/plasma radiation can add both continuum emission and line emission depending on the process regime and shielding atmosphere [7]. In addition, a narrowband component can arise from reflected or scattered process radiation near the laser wavelength, which is particularly relevant when monitoring coupling changes and optical-path disturbances [38]. Because these contributions overlap in time, practical monitoring often separates them by selecting wavelength bands (Figure 3.3) and by using multi-channel acquisition or intensity ratios to reduce sensitivity to absolute signal level and optics transmission changes [39].

The coupling between the laser and the material is often described through absorptivity $A$, defined as

$$A = 1 - R, \tag{3.1}$$

where $R$ is the material reflectivity. Absorptivity generally increases when wavelength decreases, and it typically increases in the molten state and during keyhole

formation due to multi-reflection inside the cavity [5]. These dependencies help explain why optical-emission signals are sensitive to regime transitions and surface state, but they also highlight an important limitation: the measured photodiode signal is not a direct measurement of weld quality. It integrates line-of-sight radiance and can be strongly influenced by viewing geometry, optics contamination, plume shielding, and sensor saturation. Consequently, optical-emission monitoring is most reliable when it is validated against a clearly defined decision target and when signal conditioning (band selection, normalisation, and quality checks) is used to manage process- and setup-dependent variability [40].

### 3.1.3 Thermal emissions

Thermal emissions in laser welding arise from the infrared radiation emitted by the workpiece surface as it is heated, melts, and subsequently cools. The measured radiance is governed by temperature but also by surface emissivity and by the optical path (viewing angle, reflections from the environment, and any attenuation by protective windows or fumes). In the grey-body approximation commonly used for engineering thermography, the emitted radiative power scales with $\varepsilon\sigma T^4$, so relatively small temperature changes near the melt pool can produce measurable changes in IR signal, provided that emissivity and reflections are sufficiently controlled [41, 42].

In monitoring practice, thermal emissions can be interpreted as a proxy for the *surface* thermal field and its temporal evolution, and therefore relate to heat input, thermal gradients, and cooling-rate conditions that influence microstructure, residual stress, and distortion risk [43]. Depending on the sensor (single-point pyrometry versus IR imaging), the output can describe either local peak temperatures or spatially resolved temperature maps along and around the seam. Typical monitoring descriptors include peak and mean temperature in a region of interest, the spatial extent of elevated-temperature zones, temperature gradients, and cooling-rate indicators extracted from thermal cycles [43]. Importantly, the most informative regions are not always the brightest pixels in the molten pool: plume radiation, specular reflections, and saturation can bias measurements, so many industrial and research implementations use an offset ROI adjacent to the pool and rely on relative trends rather than absolute temperature unless careful emissivity calibration is available [44].

A key limitation is that thermal emission sensing is inherently surface-limited: the camera observes surface radiance, whereas critical weld outcomes (penetration state, through-thickness thermal field, and distortion driving stresses) depend on subsurface conditions. Quantitative temperature inference is further complicated by emissivity variations with alloy, surface finish, oxidation, and phase state, as well as by reflected radiation from the hot environment and by line-of-sight disturbances (smoke/fume, spatter, protective glass contamination). For these reasons, thermal emissions are highly valuable for tracking heat-input-related behaviour and for constraining or validating thermal models, but their direct translation into internal weld quality requires either strong empirical correlation or the support of modelling assumptions that connect surface temperature histories to the underlying thermal field [45].

## 3.2 Monitoring sensors

This section summarizes the working principles of the sensors used in this thesis and clarifies the type of process information each can provide. A qualitative comparison of the main sensing options is provided in Table 3.1, and the sensors used in this thesis are detailed in the following section.

Table 3.1 Summary of representative sensing technologies for laser-welding monitoring

| Sensor | Detected object | Pro - Cons | Production readiness |
|---|---|---|---|
| **Photodiodes** | Optical emission | • Low cost<br>• *Plug&Play*<br>• Low resolution | Production setup<br>Widely used in industry |
| **HS Camera** | • Seam surface<br>• Keyhole surface oscillations | • Direct measurement<br>• Algorithm-driven<br>• Bulky<br>• High-cost | Production setup<br>Widely used in industry |
| **IR Camera** | Surface temperature | • Direct measurement<br>• Emissivity-dependent<br>• Mid-/High-cost | Few applications available;<br>research ongoing |
| **Opt. Microphone** | Acoustic emission | • High resolution<br>• Algorithm-driven<br>• High-cost | Research ongoing |
| **OCT** | • Keyhole depth<br>• Seam surface | • Direct measurement<br>• *Plug&Play*<br>• Process dependent<br>• Mid-cost | Few applications available;<br>research ongoing |

### 3.2.1 Optical Microphone

Acoustic emissions have long been investigated for monitoring laser welding, but conventional microphones can be strongly affected by background noise in industrial environments, limiting practical deployment. Optical microphones address some of these limitations by operating without moving parts and without a membrane, thereby avoiding sensitivity to mechanical properties of a vibrating diaphragm [46].

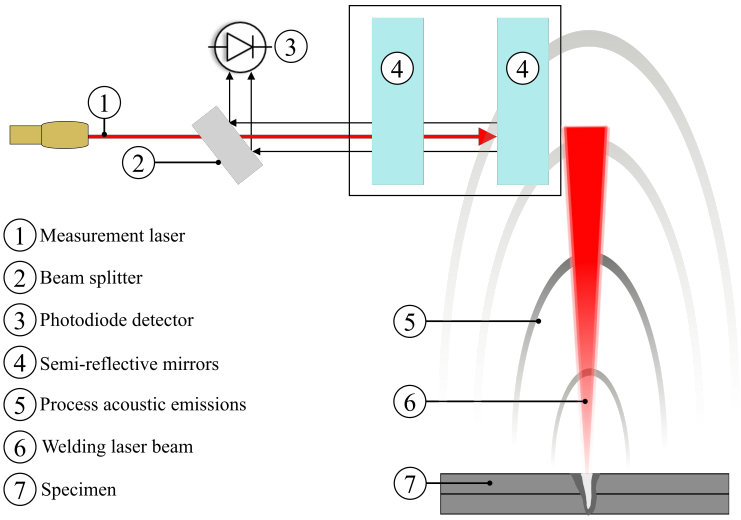


Fig. 3.4 Schematic of the working principle of the optical microphone.

As illustrated in Figure 3.4, a measurement laser is directed into a small cavity formed by two semi-reflective mirrors. Pressure waves passing through the cavity modulate the refractive index of the medium, which in turn modulates the intensity or phase of the reflected light. A photodiode converts this modulation into an electrical signal corresponding to acoustic emission. Optical microphones can cover a wide bandwidth (up to several MHz), which supports improved separation between process-related content and low-frequency background noise [47].

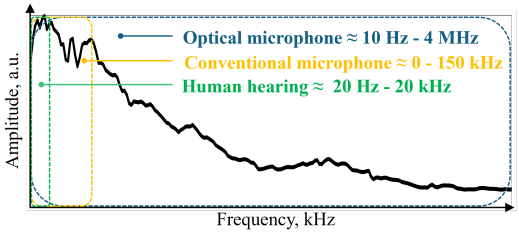


Fig. 3.5 Comparison of acoustic spectrum.

Their compact size also supports placement closer to the interaction zone without interfering with the machine, which can further reduce the influence of distant environmental noise. Figure 3.6 shows the sensor scale and an example of acquisition output (spectrogram) in the vendor software.

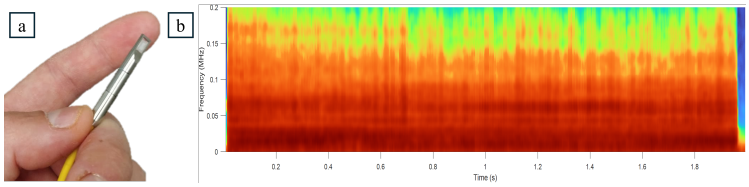


Fig. 3.6 (a) Optical microphone compared to a human finger for scale; (b) example of signal acquisition (spectrogram) displayed in the commercial software interface.

### 3.2.2 Photodiodes

Photodiodes are semiconductor sensors that convert incident optical radiation into an electrical signal through the generation of electron–hole pairs in a p–n (or p–i–n) junction. When photons with energy above the bandgap are absorbed in the active region, a photocurrent proportional to the incident radiant power is produced [48]. Because the conversion is purely electronic, photodiodes offer high bandwidth, compact form factor, and robust operation, making them widely used for in-process monitoring of laser welding [40].

In laser-welding monitoring, photodiodes are employed as *passive* sensors that measure the time-varying optical radiance emitted by the interaction zone. Depending on detector material and optical filtering, the measured signal can include contributions from: (i) broadband thermal radiation from the hot workpiece and melt pool, (ii) plume/plasma radiation (continuum and line emission), and (iii) back-reflected or scattered process radiation near the laser wavelength. For practical implementation, multi-channel arrangements are common, where different detector materials and filters are combined to isolate distinct spectral bands and to improve interpretability via ratios or differential metrics.

Figure 3.7 illustrates a representative three-channel configuration, where a set of beam splitters and filters directs the collected process light to three photodiodes with different spectral sensitivity: a Si photodiode for the visible/near-visible band, an InGaAs photodiode for the near-infrared band, and a Ge photodiode for the

extended near-infrared range. This architecture enables simultaneous acquisition of complementary emission bands (e.g. plume-dominated versus thermal-dominated components), while keeping acquisition weld-synchronous and at high sampling rates.

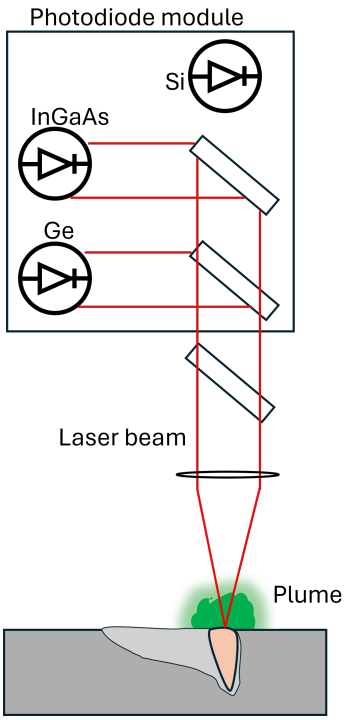


Fig. 3.7 Example of a multi-channel photodiode monitoring head using three detector materials (Si, InGaAs, Ge) to capture complementary wavelength bands via optical splitting and filtering.

The main capability of photodiode monitoring is to provide a high-sampling-rate signal that is sensitive to changes in process state. In stable operation, trends in emission intensity and its temporal modulation can reflect changes in coupling, keyhole/plume behaviour, and heat input. This makes photodiodes attractive for weld-by-weld screening and for detecting transient disturbances (e.g. loss of coupling, plume bursts, spatter-related events), particularly when the decision target is defined within a fixed operating envelope and the sensing geometry is controlled. In addition, because the hardware is inexpensive and integration is relatively straightforward (often coaxial or near-coaxial with the processing head), photodiodes are among the most production-ready sensing options for laser-welding monitoring.

However, photodiode signals are inherently *indirect* proxies of weld quality. The measured current integrates line-of-sight radiance over the sensor field-of-view and is shaped by viewing geometry, optics transmission, and the relative contributions of thermal radiation and plume/plasma emission. As a result, absolute signal levels are sensitive to confounders such as surface condition, oxide state, shielding effectiveness, plume attenuation, and contamination of protective windows. Saturation can also occur under intense process light, requiring appropriate attenuation and dynamic-range management. Moreover, changes in measured emission do not map uniquely to a single defect mechanism: similar intensity variations can arise from different combinations of penetration state, plume dynamics, or surface reflectivity changes. For this reason, robust deployment typically relies on (i) controlled and repeatable sensor placement and optical filtering, (ii) normalisation strategies (e.g. baseline referencing or ratios between bands), and (iii) decision logic validated against ground truth within a representative process window.

### 3.2.3 Optical Coherence Tomography

Optical Coherence Tomography (OCT) is a non-contact optical measurement technique originally developed for medical imaging applications [49]. Due to its high axial resolution and rapid acquisition, OCT has also been investigated for laser-welding monitoring [50, 51].

OCT is based on low-coherence interferometry (Michelson configuration). Light from a broadband source is split into a reference arm and a sample arm. Backscattered light from the specimen recombines with the reference signal to form an interference spectrum, which is converted into depth-resolved information through spectral analysis (typically via FFT) [26]. In welding applications, OCT can support pre-process seam tracking, in-process depth-related observables (under favourable optical conditions), and post-process surface profiling. In contrast to purely emission-based sensors, OCT provides measurements in metric units (mm) with micrometre-scale axial resolution; however, signal quality can degrade due to multiple reflections, plume/spatter disturbances, and optical-path instability.

Figure 3.9 shows a representative measurement from commercial software, where scatter is visible in segments affected by process disturbances and internal reflections.

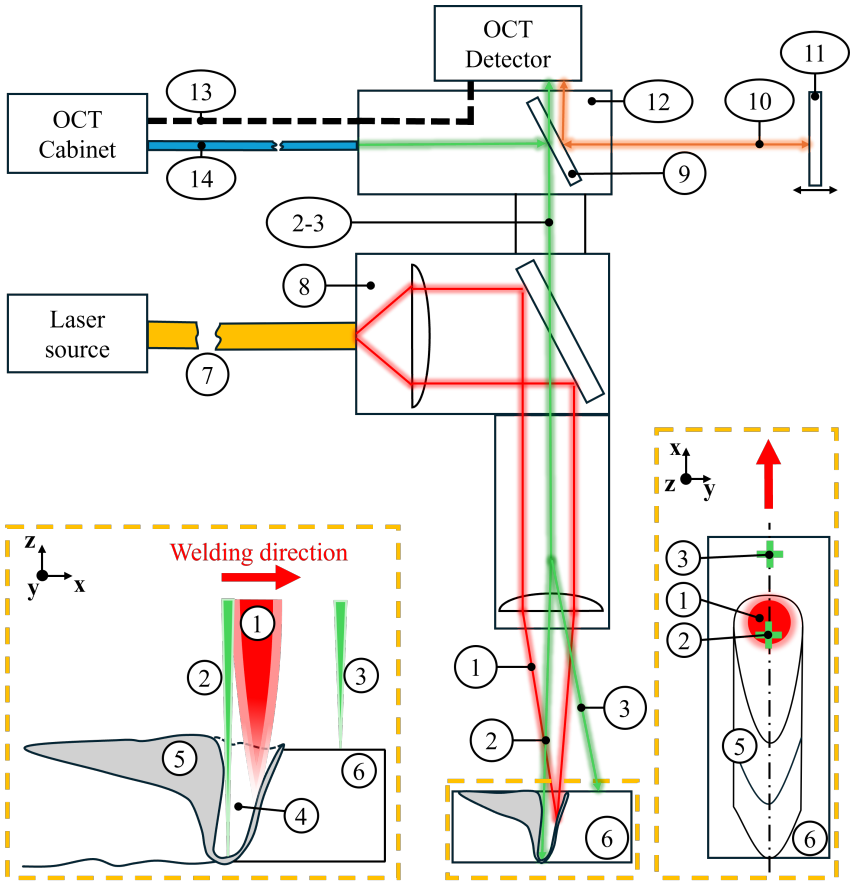


Fig. 3.8 Schematic of OCT working principle.

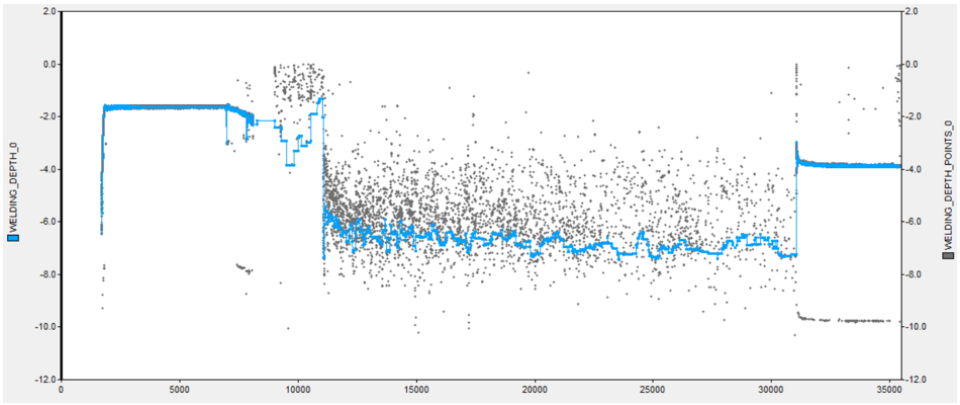


Fig. 3.9 Example of OCT measurement from commercial software.

### 3.2.4 Thermal Camera

Infrared (IR) thermal cameras are passive sensors that measure the thermal radiation emitted by the workpiece surface (and, unavoidably, reflected radiation from the surrounding scene). By recording radiance within a defined spectral band, the camera provides a spatially resolved radiometric measurement that can be converted into an apparent surface temperature field when emissivity and reflected-background terms are specified. In laser welding, this enables time-resolved observation of the thermal footprint around the seam and supports the extraction of thermal-cycle descriptors (e.g. peak temperature, heating/cooling rates, and spatial gradients) that relate to heat input and heat flow [27].

Figure 3.10 shows a representative schematic of the working principle of a thermal camera.

IR imaging for industrial thermography is commonly implemented in near-/short-wave IR (NIR/SWIR), medium-wave IR (MWIR), and long-wave IR (LWIR) bands. For laser welding with typical processing wavelengths around $\sim 1\ \mu$m, LWIR cameras ($\sim 7.5$–$14\ \mu$m) are frequently selected because their detection band is spectrally separated from the laser emission, which reduces direct interference from process light. In addition, using a fixed acquisition geometry (stand-off distance and viewing angle) improves repeatability and supports consistent spatial sampling and ROI placement along the seam [52].

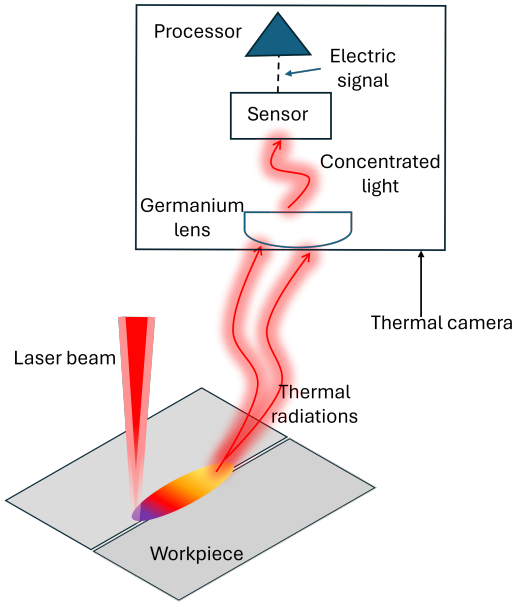


Fig. 3.10 Schematic of IR-thermography acquisition in laser welding, illustrating an oblique viewing geometry and a representative ROI around the seam.

From a monitoring perspective, thermography is primarily informative about the *surface* thermal field. Typical monitoring outputs derived from thermograms include:

- ROI-based temperature statistics (mean/median/percentiles, peak temperature);
- thermal gradients across the seam (spatial temperature drop-off);
- cooling-rate proxies obtained from temporal derivatives or from paired ROIs (e.g. upstream/downstream, centre/tail);
- geometrical cues from isotherms (e.g. apparent molten-pool width), when saturation is avoided.

These indicators can be used for weld-by-weld screening, trend monitoring (e.g. drift in heat input), and, in modelling-oriented workflows, to extract representative thermal cycles that constrain thermo-mechanical simulations for distortion assessment [53].

Key practical limitations arise because the camera measures radiance rather than temperature. Quantitative temperature retrieval is therefore sensitive to (i) emissivity, which depends on material, surface condition, oxidation, and phase state (solid vs.

liquid), (ii) reflected radiation from the environment and hot process sources, and (iii) line-of-sight disturbances such as plume, fumes, and spatter. In high-intensity regions (inside/near the molten pool), emissivity transients and pixel saturation can further degrade reliability. For robust monitoring, thermal-cycle extraction is therefore often performed in solid material adjacent to the molten zone, where emissivity is comparatively more stable and the sensor response remains within range; spatial averaging over a fixed ROI is commonly used to improve repeatability. Finally, optics protection (e.g. windows, purging) and periodic baseline checks are typically required to mitigate contamination-related drift in industrial conditions.

# Chapter 4

# Case study 1 – Monitoring process stability in remote laser welding using an optical microphone

## 4.1 Introduction

This chapter examines acoustic emissions measured by a membrane-free optical microphone for in-process monitoring of laser welding, with the aim of linking acoustic signatures to keyhole dynamics at the local process scale. Subsequently, feature-level fusion is evaluated by combining optical-microphone features with spectral-emission features from a photodiode system to improve joint-quality detection and classification.

This section establishes the industrial context by outlining the motivation for monitoring in electric-vehicle battery manufacturing. It then reviews prior work on optical-microphone-based acoustic monitoring and complementary multi-sensor strategies.

In the automotive transition toward Battery Electric Vehicles (BEVs), production processes face increasing pressure to satisfy strict safety and functional requirements. The battery pack is one of the most important subsystems of a BEV and requires stringent production standards to ensure safety and performance [54].

In this context, laser beam welding is widely adopted to connect terminals and busbars because it enables high throughput and comparatively low heat input with respect to alternative joining methods [55]. However, a battery pack can contain thousands to millions of welded interconnections, and even a single defective weld may compromise the assembly's performance or safety [56]. To maintain high standards of quality and reliability, robust strategies for detecting defects in real time during manufacturing are therefore essential [57].

Several studies have investigated in-situ monitoring for reliable quality assessment in laser welding [22]. Because key quality outcomes such as penetration and internal discontinuities are not always directly observable from surface imagery alone, indirect monitoring of process emissions provides an attractive route to in-line indicators of weld process state and, ultimately, joint quality.

Indirect monitoring relies on process emissions that can be correlated with variations in welding status. Two common examples are spectral-emission monitoring and acoustic-emission monitoring. For instance, Chianese [58] reported that variations in process conditions can be reflected in changes in ultraviolet-to-visible spectral emissions. Similarly, acoustic signals have been shown to reflect the rapid thermal and mechanical variations occurring in the weld zone [59]. However, the practical use of acoustic methods has historically faced obstacles, mainly due to their high sensitivity to background noise, which makes it difficult to extract weld-relevant information from acoustic signals.

Recent innovations have renewed interest in acoustic monitoring, particularly through the development of optical microphones with frequency bandwidths up to several MHz. Optical microphones may exhibit superior resistance to background noise in certain operating conditions due to their distinct detection principle [47]. A detailed description of the optical microphone is provided in Section 3.2.1.

Optical microphones have demonstrated significant potential across diverse laser-based manufacturing applications. Nasab et al. [60] associated acoustic signatures with different process regimes during Laser Powder Bed Fusion (LPBF), and showed that acoustic emissions in the 40–82 kHz range capture the transition from conduction to keyhole regime. In a similar study, De Formanoir et al. [61] correlated the acoustic signal within the 30–100 kHz frequency range with successful porosity elimination during LPBF re-work. Prieto et al. [62] employed an optical microphone

to detect crack formation during Laser Metal Deposition (LMD), associating acoustic signatures in the 350–1000 kHz range with crack formation.

Beyond additive manufacturing, optical microphones have also been applied to ultra-short pulse (USP) laser ablation processes, which demand high-resolution temporal and spectral monitoring due to rapid material transformation. Lutz et al. [63, 64] employed an optical microphone to detect material transitions between copper and polyimide layers during USP laser ablation and found corresponding acoustic signatures in the 100–20000 kHz range.

Optical microphones have also demonstrated good capability in laser welding applications. Kramer et al. [65] studied how sensor positioning influences the detected laser-welding signal, showing that distance, angle, and orientation affect the signal-to-noise ratio, and that positioning the sensor at a 10° angle relative to the surface improved signal strength, especially for frequencies exceeding 10 kHz. Omlor et al. [66] utilized an optical microphone together with a high-speed camera to evaluate the weld quality of hairpins in electric motor stators through acoustic emission (AE) analysis. Their regression analysis demonstrated that AE signals in the 10–800 kHz band correlated with laser power ($R^2 = 0.805$) and the laser focus position ($R^2 = 0.835$). Heilmeier et al. [67] reported substantial fluctuations in statistical features of AE caused by the introduction of defects such as oil contamination or joint misalignment. Kramer et al. [68] also investigated the effect of surface contamination during T-joint welding, finding a significant shift in the 50–175 kHz AE frequency range; the observed changes were closely linked to higher porosity, underfilling, and lower penetration depth.

Several studies have further focused on penetration depth during laser welding. Authier et al. [47] fused features from an optical microphone and Optical Coherence Tomography (OCT), identifying a correlation between AE in the 40–90 kHz range and penetration depth. Similar conclusions were reported by Tomcic et al. [69], who analyzed 17 acoustic features to identify correspondence with penetration depth. They found that zero-crossing-rate features, in particular within the 40–90 kHz frequency range, were among the strongest predictors. Table 4.1 summarizes studies focused on laser-material process monitoring with optical microphones.

Other monitoring strategies employ multiple sensors to capture complementary process information and combine their outputs to improve defect detection and classification. For example, Liu et al. [71] used photodiodes and cameras, principal

Table 4.1 Key research contributions using optical microphones in laser-material processing

| Material | Application | Weld feature | AE Freq. (kHz) | REF. |
|---|---|---|---|---|
| AISI 304 SS | LPBF | Keyhole instabilities | 40, 60, 70, 77, 82, 250 | [60] |
| 316L SS | LPBF | Porosity | 30-100 | [61] |
| 316L SS, M2 Steel | LMD | Cracks | 350 | [62] |
| Cu, Polyimide | LA | Layer transitions | 100-2000 | [64] |
| Cu, Polyimide | LA | • Layer transitions<br>• Ablation volume<br>• Focus position | • 50-2000<br>• 50-2000<br>• 97.5-98.5 | [63] |
| Carbon-based Diffusion Media | LA | Ablation volume | 50 | [70] |
| 316L SS, TA6V Ti | LW | Penetration depth | 40-90 | [47] |
| Cu-OF | LW | • Spatters<br>• Beam deviations | 10-800 | [66] |
| Cu | LW | Penetration depth | 40-90 | [69] |
| Cu, Ni-Steel | LW | • Penetration depth<br>• Contamination<br>• Burn-through | N.A. | [67] |
| 316L SS | LW | • Connection status<br>• Humping<br>• Focus position | N.A. | [70] |
| Ni | LW | Contamination | 50-175 | [68] |

component analysis (PCA) for feature extraction, and a support vector machine (SVM) to classify the welding status. Zhang et al. [72] used a multi-sensor system including photodiodes, a spectrometer, and visual systems to capture spatial and spectral features, extracting features via wavelet decomposition, statistical analysis, and image processing, followed by classification with a convolutional neural network (CNN). In another study, Zhang et al. [73] combined five sensors and employed a stacked sparse autoencoder (SSAE) to discriminate welding classes, achieving an average accuracy of 95.07%. Ma et al. [74] developed a system using a high-speed camera and coherent light measurement to estimate keyhole geometry; time–frequency features were derived and used to train a CNN for porosity localization. Brežan et al. [75] integrated photodiodes and Optical Coherence Tomography (OCT) for remote laser welding of Cu–Al joints and used a random forest model to identify OK and NOK welds. Cao et al. [76] proposed a cross-attention fusion network that learns temporal features directly from photodiodes and a microphone sensor, reporting high accuracy under imbalanced data.

Taken together, prior work supports the sensitivity of both acoustic and optical emissions to process variations, yet the evidence base remains uneven across materials, joint configurations, and defect mechanisms. In particular, optical-microphone studies in laser welding have primarily addressed specific alloys and setups, and fewer investigations target thin aluminium electrical interconnections produced by remote laser welding, where part-to-part gaps and power variations can drive distinct keyhole conditions and joint-quality outcomes. Moreover, while multi-sensor approaches are increasingly explored, it remains important to clarify when feature-level fusion provides a consistent advantage over a single-sensor pipeline, especially under controlled and interpretable defect mechanisms.

For this reason, this activity aims to validate literature findings on a material that remains underexplored for acoustic-emission-based laser-welding monitoring, to investigate additional joint configurations, and to compare performance with and without feature-level fusion.

Part of the information contained in this chapter is extracted from the paper: "**D. Basile**, R. Al Botros, M. De Maddis, V. Razza, P. Franciosa, *Monitoring part-to-part gap and laser power effects in remote laser welding of 1050 aluminum busbar-to-terminal connections via optical microphone sensing*, 2025" (reference [30]).

## 4.2 Objectives

This chapter addresses **RQ1:** *What information on process stability can be extracted from acoustic and optical emissions during remote laser welding of thin aluminum sheets?*

To answer RQ1, the study pursues the following objectives:

- Assess the sensitivity of optical-microphone acoustic emissions to process-state variations associated with keyhole dynamics during remote laser welding, and identify quantitative acoustic indicators linked to process stability;
- Evaluate how representative sources of variation in battery-interconnection welding (in particular part-to-part gap and laser power changes) affect the measured emissions and the resulting joint-quality outcomes;
- Develop and compare data-driven classification pipelines using (i) acoustic features only and (ii) feature-level fusion of acoustic and photodiode-derived spectral features, to determine whether multi-sensor integration yields consistent gains in detection and classification performance;
- Quantify performance and discuss practical robustness limits relevant to in-line deployment, including sensitivity to background noise and sensor positioning.

## 4.3 Experimental program

The experimental program comprised two stages:

1. First, the capability of the optical microphone alone was evaluated to assess whether variations in laser power and part-to-part gap can be detected during remote laser welding of AA1050 in an overlap configuration. A full-factorial design was adopted, with 12 laser-power levels (800–1350 W) and 5 part-to-part gap levels (0–1 mm), for a total of 180 runs. In addition, a supplementary test at 2000 W with zero gap was conducted to assess whether the microphone can detect a piercing event (excessive penetration).
2. Second, the same factorial dataset (180 runs) was analysed using feature-level fusion, by combining quantitative features extracted from the optical

microphone and photodiode signals. The objective was to evaluate whether multi-sensor integration improves the classification of weld conditions (lack of fusion, lack of connection, and sound connection).

## 4.4 Experimental setup

The material employed in this investigation was aluminium AA1050. The specimens had dimensions of $120 \times 38 \times 1$ mm. The experiments were conducted in an overlap configuration with a weld length of 30 mm. The laser source was a Coherent HighLight FL-ARM 10000 with a 100 µm core-fibre diameter. Although the source can generate a combined core-to-ring beam, only the core beam was used in this study. Beam delivery and scanning were performed using a K-Lab SCOUT-200 2D scanner. The specifications of the welding equipment are detailed in Table 4.2, and the experimental configuration is illustrated in Figure 4.1.

All experiments were conducted without shielding gas or filler wire. A cross-jet was not employed, as its use would have introduced additional flow-induced acoustic components requiring separate filtering and analysis. Samples were cleaned with acetone prior to welding to remove surface contaminants.

Acoustic emissions (AE) generated during laser welding were recorded using an Eta250 ultra optical microphone (Xarion, Austria). The microphone was positioned 70 mm above the weld zone (along $z$) and 30 mm laterally from the beam path (along $y$), with the sensing face oriented toward the laser–material interaction region. The position was selected based on preliminary tests to maximize the signal-to-noise ratio while maintaining a safe stand-off distance. To ensure repeatability, the microphone position was kept fixed throughout all experiments.

Optical emissions were monitored using an LWM 4.0 photodiode system (Precitec, Germany), providing three wavelength channels to capture emissions in the ultraviolet, visible, and infrared ranges. Synchronization of acoustic and optical signals with the process start was achieved using an MSO3014 oscilloscope (Tektronix, Oregon). The analogue scanner signal transmitted to the laser source was used as the main trigger.

Acoustic signals were acquired at a sampling frequency of 2.5 MHz; 5 million samples were recorded, corresponding to a total acquisition duration of 2 s. Optical

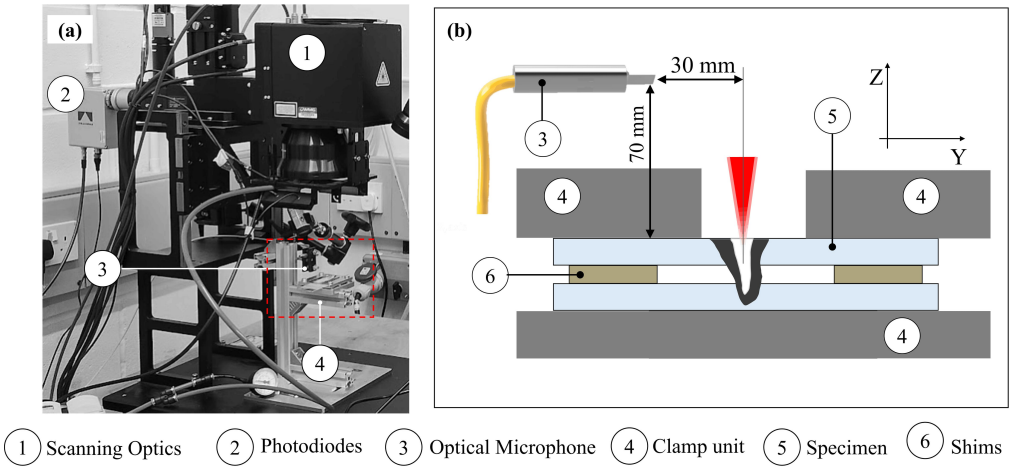


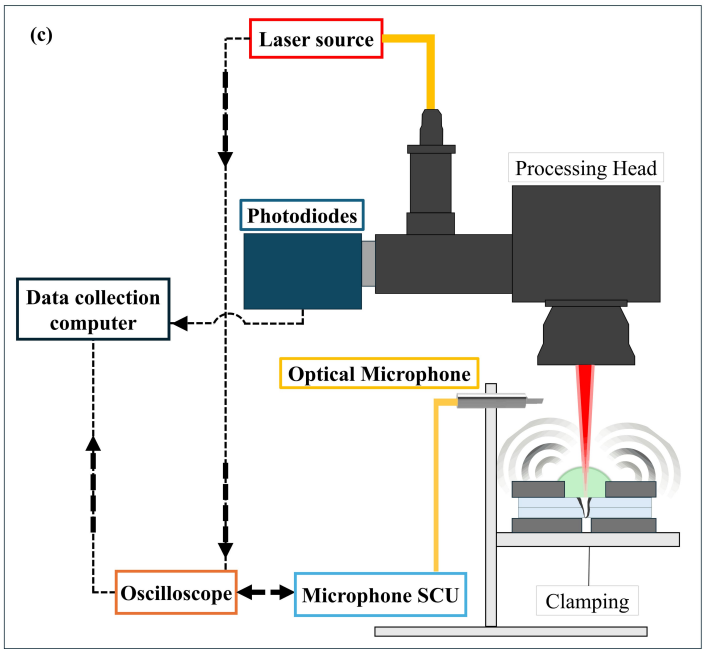


Fig. 4.1 (a)–Experimental setup. (b)–Detailed schematic. (c)–Connection setup scheme.

Table 4.2 Specifications of the laser welding system.

| **Coherent HighLight FL-ARM 10000** | | **K-Lab SCOUT-200** | |
|---|---|---|---|
| Maximum power | 10 kW | Max. allowed power | 2 kW |
| Core maximum power | 5 kW | Scanning field | $70 \times 70$ mm$^2$ |
| Wavelength | $1070 \pm 10$ nm | Collimating length | 100 mm |
| Fibre core diameter | 100 µm | Focusing length | 254 mm |
| BPP | 4 mm·mrad | Rayleigh length | 0.8 mm |
| Laser mode | Multi-mode | Spot size | 254 µm |

signals were acquired at a sampling frequency of 50 kHz over the same 2 s window. Figure 4.2 shows the alignment of the acquired signals and the corresponding regions of interest (ROI) used for subsequent analysis.

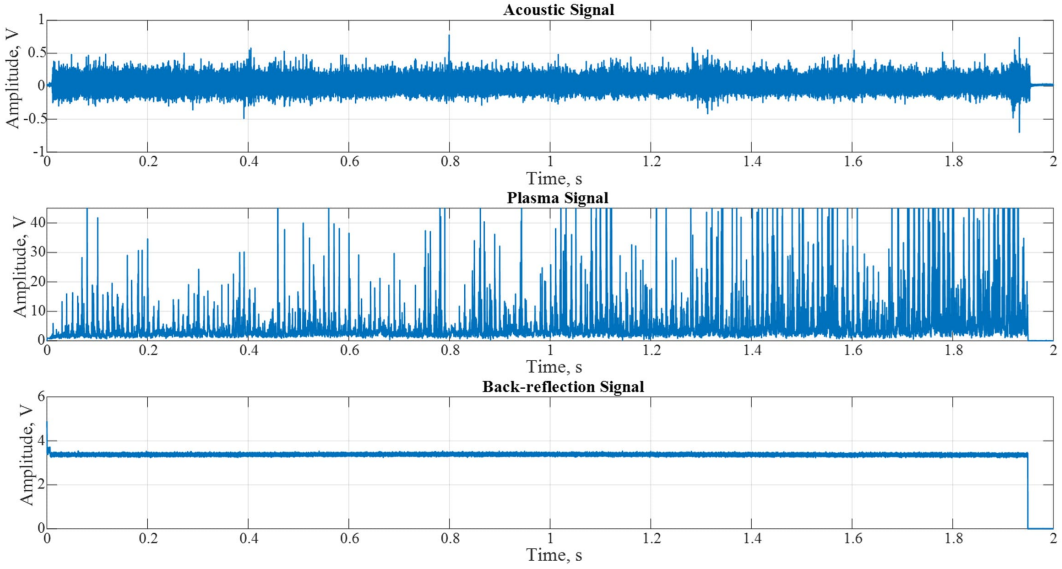


Fig. 4.2 Acquired acoustic and spectral signals, with the corresponding regions of interest (ROI) used for analysis.

### 4.4.1 Design of Experiments and Data Preparation

A full-factorial experimental plan was adopted in which two parameters were varied: laser power and part-to-part gap. These factors were selected because their variations represent major sources of disturbance for the targeted application. Laser power is critical in battery welding: insufficient power reduces the effective power density and can hinder stable keyhole formation, resulting in lack of fusion or incomplete

connection, whereas excessive power may lead to over-penetration or burn-through, with the potential to damage underlying components. The part-to-part gap was included because precise fit-up is essential in overlap welding of battery connectors; an excessive gap can inhibit contact and lead to lack of connection or weak joints, which may appear acceptable from the outside despite insufficient metallurgical bonding [77].

The laser power ($P_L$) was varied between 800 and 1350 W in 50 W steps, while the part-to-part gap was varied from 0 to 1 mm in 0.25 mm steps (Table 4.3). Each parameter combination in the full-factorial matrix was repeated three times, for a total of 180 welding trials.

In addition to the factorial campaign, a dedicated set of tests was carried out at $P_L = 2000$ W and zero part-to-part gap using the optical microphone only, to evaluate whether the microphone can detect the onset of piercing. Photodiode acquisition was not included in this supplementary set because the goal was to isolate the acoustic signature of piercing under a controlled configuration consistent with the baseline optical-microphone setup; multi-sensor comparisons were restricted to the factorial campaign. Under the tested conditions, $P_L = 2000$ W was identified experimentally as the threshold at which the laser beam fully penetrated the bottom sheet, corresponding to a clear transition from a blind to a passing-through keyhole. These tests were replicated three times to verify repeatability.

It is worth noting that full penetration does not necessarily imply a piercing event. As illustrated in Figure 4.3(a–b), both cases correspond to full penetration in the sense that the molten layer extends to the bottom surface. However, in Figure 4.3(a) the keyhole remains blind and does not propagate through the bottom sheet. As such, the laser beam (schematically shown as small arrows in Figure 4.3(a–b)) is ultimately absorbed by the keyhole walls (or back-reflected toward the top surface) and does not pierce through the bottom.

Following this logic, only Figure 4.3(b) is associated with a piercing event. To identify piercing experimentally, a stainless-steel foil, labelled “check-surface” in Figure 4.1(b), was positioned 50 mm below the bottom sheet. The 50 mm offset was selected to reflect a representative battery-module design, accounting for the spacing between the busbar and the cells as well as the presence of plastic harnesses used to secure the busbar. If the laser pierced the bottom sheet, a marking would be produced on the stainless-steel foil. Although piercing occurred at 2000 W under

Table 4.3 List of process parameters varied in the welding trials.

| **Parameters** | **Unit** | **Value** |
|---|---|---|
| Laser Power, $P_L$ | W | 800, 850, 900, 950, 1000, 1050, 1100, 1150, 1200, 1250, 1300, 1350 |
| Part-to-part gap | mm | 0, 0.25, 0.5, 0.75, 1.0 |

Table 4.4 Constant welding process parameters.

| **Parameters** | **Unit** | **Value** |
|---|---|---|
| Welding speed | mm/s | 15 |
| Wobbling trajectory | - | Circular |
| Wobbling frequency | kHz | 1 |
| Wobbling radius | mm | 0.2 |
| Seam length | mm | 30 |

the tested conditions, this threshold is not assumed to be universal. Piercing may depend on additional factors such as material properties, optical configuration, and other process parameters; future work should therefore investigate whether piercing induced by different conditions can be detected using the same approach.

Shim packs (Meusburger, Germany) of 12.5 mm width were employed to precisely control part-to-part gaps. To ensure a consistent laser spot size, and thus maintain a constant power density, the focal position along $z$ was adjusted by an amount equal to the shim-pack thickness used in each welding configuration. All welds were produced with a circular wobbling pattern of 0.2 mm radius at 1 kHz frequency (Table 4.4).

Metallographic analysis was performed by cutting each seam into two cross-sections, 10 mm from both the start and the end of the weld. The cross-sections were then hot-mounted, ground, polished, and etched with a 20% NaOH solution. Images were acquired using a Nikon Eclipse LV150N.

Cross-sections of the welded samples were examined, and the following weld features were extracted (see Figure 4.3(c)): weld width at the top of the weld bead ($W_T$), weld width at the interface between the two sheets ($W_I$), and effective penetration depth ($D_E$), measured from the top of the bottom sheet to the lowest point of the weld. $D_E$ was used as the key geometrical feature to evaluate the effectiveness of the connection between the upper and bottom sheets. In this study, the weld connection was considered effective when $D_E$ exceeded 25% of the thickness of the

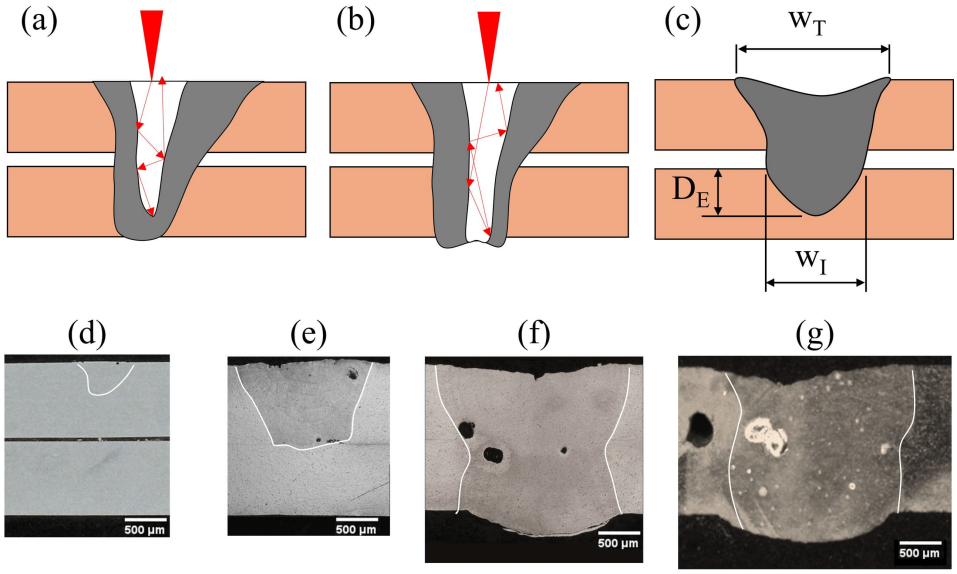


Fig. 4.3 (a, b) Conceptual representation of the transition from a blind to a passing-through keyhole; (c) schematics of the weld features; representative weld (at zero part-to-part gap) of (d) lack of fusion, (e) lack of connection, (f) sound connection, (g) weld where piercing occurred.

lower sheet. The acceptance limit on $D_E$ was adapted from previous studies [78, 79]. Four classes of weld joints were introduced (Figure 4.3(d–g)):

- **Lack of fusion (LoF)**: no significant fusion was achieved in the upper sheet, and only a superficial marking was observed.
- **Lack of connection (LoC)**: (1) effective weld depth $D_E$ lower than 25% of the sheet thickness (1 mm), indicating insufficient penetration; **or** (2) full penetration through the bottom sheet, but lack of material bridging due to excessive part-to-part gap.
- **Sound connection (SoC)**: acceptable weld with $D_E$ greater than 25% of the sheet thickness (1 mm), and not exceeding the threshold for a piercing event (marking on the "check-surface"), indicating an effective connection between the sheets.
- **Piercing**: visible mark left on the "check-surface".

The original dataset comprised 30 samples labelled as LoF, 90 samples labelled as LoC, and 60 samples labelled as SoC. The performance of a classification model can

be influenced by the composition of the dataset; in this case, the class imbalance led to poor model performance. This was because a wide parameter space was explored through the full-factorial design, resulting in a non-uniform distribution of joint-quality outcomes. Several techniques can be implemented to handle class imbalance, including cost-sensitive learning, signal manipulation, and over- or under-sampling [80].

In this study, class imbalance was addressed via data augmentation using a linear combination of signals from the same minority class. Augmented signals were generated by selecting two signals within the same class and computing the element-wise average at each time index. After balancing, the dataset comprised 90 samples labelled as LoF, 90 samples labelled as LoC, and 90 samples labelled as SoC.

Table 4.5 Class count before and after class balancing.

| **Class** | **Before (%)** | **After (%)** |
|---|---|---|
| LoF | 30 (16.67) | 90 (33.33) |
| LoC | 90 (50) | 90 (33.33) |
| SoC | 60 (33.33) | 90 (33.33) |

### 4.4.2 Acoustic Signal Processing

Preliminary trials were performed to assess the influence of background-noise sources (ventilation hood, water circuit, and compressed-air circuit) on the acoustic signal acquired by the optical microphone. To quantify potential noise contamination, the signal-to-noise ratio (SNR) was computed according to Eq. 4.1, where $RMS_{signal}$ denotes the root mean square of the recorded acoustic signal and $RMS_{background}$ denotes the root mean square of the background noise.

$$SNR = 20\log_{10}\left(\frac{RMS_{signal}}{RMS_{background}}\right) \tag{4.1}$$

Three denoising approaches—wavelet denoising, spectral subtraction, and Wiener filtering—were considered because they are commonly used for non-stationary

acoustic-emission (AE) signals [81–83]. Each technique was applied to the same region of interest (ROI), and the resulting SNR values were compared. The raw recordings yielded an SNR of approximately 17.93 dB, indicating limited background-noise interference under the present laboratory conditions. Wavelet denoising and spectral subtraction did not improve the SNR (17.93 dB), whereas Wiener filtering reduced it to 14.49 dB. This behaviour suggests that the background noise and the signal of interest occupy partially overlapping frequency bands; therefore, attempting noise removal may also attenuate weld-relevant content. The SNR decrease obtained with Wiener filtering is consistent with its inherent trade-off between noise attenuation and signal preservation [84]. Overall, the initial acquisition configuration proved suitable for capturing AE without substantial background-noise contribution. Nevertheless, production environments may introduce additional noise sources (machinery and auxiliary equipment) beyond those present in the laboratory. Moreover, while cross-jet flow was intentionally excluded in this study to isolate the effects of part-to-part gap and laser power, introducing cross-jet could modify the noise spectrum and should be examined in future work.

Figure 4.4 reports a representative microphone signal together with the analog output of the laser source. After a ramp-up phase of 7 ms (Figure 4.4(b)), the laser analog signal reaches its maximum value (1 V corresponding to 1000 W). The acoustic signal becomes evident from 11 ms onward, indicating a delay of approximately 4 ms between the laser reaching peak power and the measurable onset of acoustic emissions. This delay can be attributed to the transient phase during which the laser interacts with the workpiece and deposits sufficient energy for the material to reach its melting point; this stage is not instantaneous because it involves thermal propagation within the material volume. To avoid bias due to transient effects, only the central portion of the acoustic signal (0.5–1.5 s) was retained, excluding the initial and final phases. This ROI corresponds to the portion of the seam where the specimen cross-sections were evaluated (at 10 mm, 0.66 s and 20 mm, 1.33 s).

Power spectral density ($\hat{P}_{xx}(f)$) estimates were computed using Welch's method, which increases robustness by averaging spectra obtained from overlapping segments [85]. A Hann window was applied to each segment [84]. The corresponding estimator is given in Eq. 4.2, where $X_i(f)$ is the DFT of the $i$-th segment, $L$ is the number of overlapped segments, and $U$ is the window normalization factor ($U \sim 0.375$ for the Hann window).

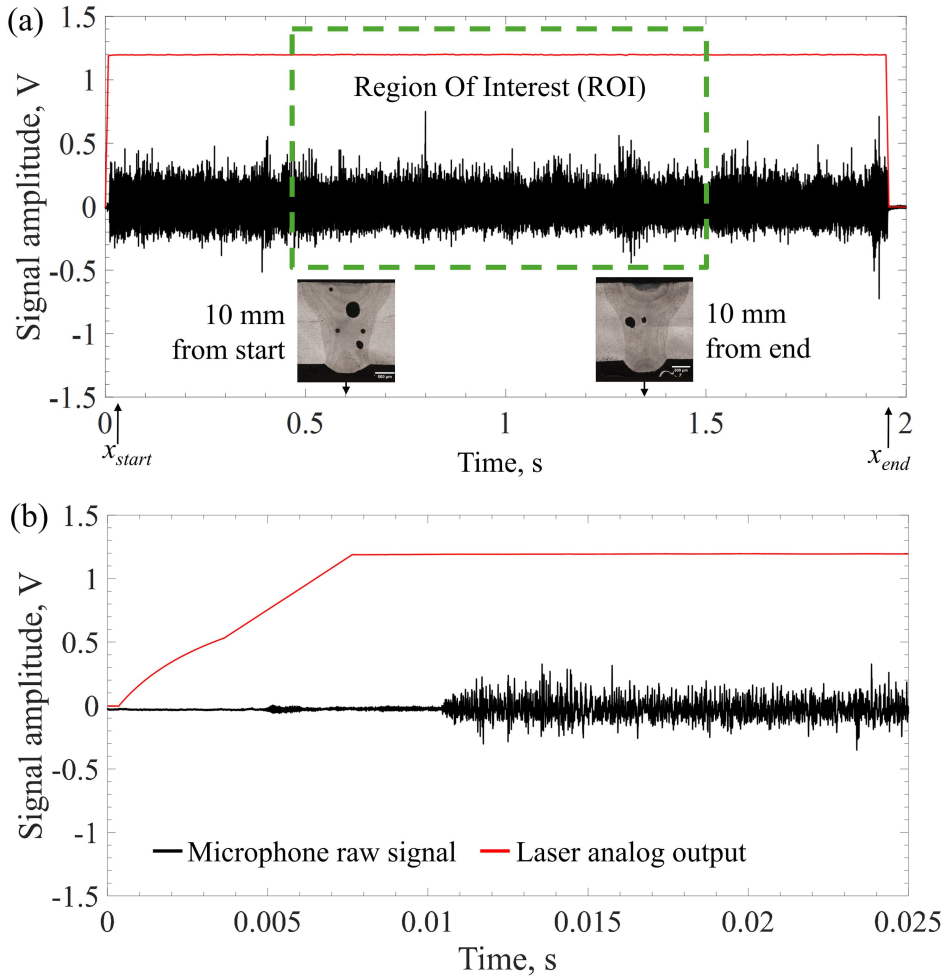


Fig. 4.4 (a) Example of optical-microphone raw signal and analog signal of the laser output; (b) zoom-in view between 0 and 0.02 s to highlight the delay between the laser output and the acoustic signal.

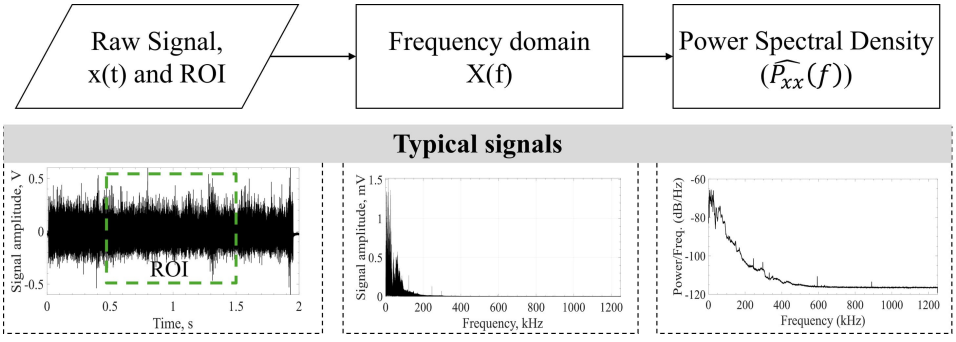


Fig. 4.5 Methodological flowchart of the procedure implemented for signal processing.

$$\hat{P}_{xx}(f) = \frac{1}{L \cdot U} \sum_{i=0}^{L-1} |X_i(f)|^2 \tag{4.2}$$

For the AE signals, 4 ms segments (10,000 samples at a 2.5 MHz sampling rate) with a 2 ms (50%) overlap were selected. This setting provides a 250 Hz frequency resolution, which is sufficient to resolve the relevant spectral content while maintaining a detailed representation. The 50% overlap improves the statistical reliability of the estimate through increased averaging without excessive computational burden. The selected parameters were confirmed in preliminary trials to preserve signal characteristics and to reduce spectral leakage and estimator variance.

The relationship between extracted signal features and weld features was quantified using Pearson's correlation coefficient. Correlation values range from $-1$ to 1, with 0 indicating no linear correlation. In addition, a two-way analysis of variance (ANOVA) was performed to test the statistical significance of the process parameters with respect to the extracted signal features, using a significance level of 5%.

### 4.4.3 Feature extraction

From the acoustic and spectral signals, several features were extracted. Features are named using the convention "signal namefeature name/symbol"; for example, $s_p$ denotes the sound power. For further details, the reader is referred to the nomenclature section. The features were extracted considering the ROI segment $\{x(n)\}_{n=1}^{N}$, where $x(n)$ denotes the amplitude at sample index $n$, and $N$ is the total number of samples in the ROI.

The *mean* was defined as

$$\mu \;=\; \frac{1}{N} \sum_{n=1}^{N} x(n). \tag{4.3}$$

The *standard deviation* was computed using the unbiased estimator

$$\sigma \;=\; \sqrt{\frac{1}{N-1} \sum_{n=1}^{N} \big[x(n) - \mu\big]^2}. \tag{4.4}$$

The standard deviation $\sigma$ quantifies the dispersion of the amplitudes around the mean and therefore captures the variability (spread) of the signal within the ROI.

The *median* is a robust measure of central tendency defined as the middle value of the sorted samples. Let $x_{(1)} \leq \cdots \leq x_{(N)}$ be the ordered samples; then

$$\text{median}(x) \;=\; \begin{cases} x_{(\frac{N+1}{2})}, & N \text{ odd}, \\ \frac{1}{2}\Big(x_{(\frac{N}{2})} + x_{(\frac{N}{2}+1)}\Big), & N \text{ even}. \end{cases} \tag{4.5}$$

Furthermore, the *mode* was included, i.e. the most frequently occurring amplitude value within the ROI. For continuous-valued signals, the mode was estimated from the amplitude histogram as the center of the bin with maximum count.

A robust dispersion proxy was also computed via the *mean absolute deviation* (MAD) about the mean:

$$\text{MAD}(x) \;=\; \frac{1}{N}\sum_{n=1}^{N}\Big|x(n)-\mu\Big|. \tag{4.6}$$

Unlike variance-based dispersion measures, $\text{MAD}(x)$ reduces the influence of outliers by using absolute deviations rather than squared deviations.

The *interquartile range* (IQR) was defined as the difference between the $75^{\text{th}}$ percentile $(Q_3)$ and the $25^{\text{th}}$ percentile $(Q_1)$:

$$\text{IQR}(x) \;=\; Q_3 - Q_1. \tag{4.7}$$

The IQR measures the spread of the central 50% of the samples and is therefore robust to extreme values.

Higher-order moments were used to characterise the shape of the amplitude distribution. The *skewness* quantifies asymmetry about the mean:

$$\text{Skew}(x) \;=\; \frac{1}{N\sigma^3}\sum_{n=1}^{N}\big[x(n)-\mu\big]^3, \tag{4.8}$$

where $\sigma$ is the standard deviation. Positive skewness indicates a heavier right tail, whereas negative skewness indicates a heavier left tail.

In parallel, the *kurtosis* captures the "peakedness" (or tail heaviness) relative to a Gaussian-like profile:

$$\mathrm{Kurt}(x) \;=\; \frac{1}{N\,\sigma^4}\sum_{n=1}^{N}\big[x(n)-\mu\big]^4. \tag{4.9}$$

Beyond distributional descriptors, the *zero-crossing rate* (ZCR) was included, a common feature in acoustic signal analysis. It measures how frequently the signal changes sign:

$$\mathrm{ZCR}(x) \;=\; \frac{1}{2\,(N-1)}\sum_{n=2}^{N}\Big|\mathrm{sgn}\big(x(n)\big)-\mathrm{sgn}\big(x(n-1)\big)\Big|, \tag{4.10}$$

where $\mathrm{sgn}(y)\in\{-1,0,+1\}$ denotes the sign of $y$. A larger ZCR typically reflects higher predominant frequency content or more rapid oscillations. For photodiode-based signals (plasma emission $p$ and back-reflection $r$), the waveform is typically positively biased and remains above zero; consequently, the ZCR tends to be identically (or approximately) zero and carries limited discriminative information (as reflected by the negligible feature importance in Table 4.14).

Additionally, the *short-time energy* (STE) was computed as an intensity-related descriptor of the ROI:

$$\mathrm{STE}(x) \;=\; \frac{1}{N}\sum_{n=1}^{N}\big[x(n)\big]^2. \tag{4.11}$$

This feature increases with both signal amplitude and sustained activity within the interval.

**Acoustic emissions spectral features** Finally, for the acoustic-emission signal (prefix $s$), spectral power features were extracted to capture the frequency content of the ROI. Sound power was obtained by integrating the estimated one-sided power spectral density $\hat{P}_{xx}(f)$ over a frequency interval $[f_1, f_2]$:

$$s_{p,\{f_1,f_2\}} \;=\; \int_{f_1}^{f_2}\hat{P}_{xx}(f)\,\mathrm{d}f, \tag{4.12}$$

with $0 \leq f_1 < f_2 \leq f_{\text{Nyq}}$ and $f_{\text{Nyq}} = f_s/2$ the Nyquist frequency for sampling rate $f_s$. In discrete form, for frequency bins $f_k$ with spacing $\Delta f$,

$$s_{p,\{f_1,f_2\}} \approx \sum_{k:\, f_1 \leq f_k \leq f_2} \hat{P}_{xx}(f_k)\,\Delta f. \tag{4.13}$$

Accordingly, the following sound-power features were considered for the microphone signal: $s_{p,\text{0-8}}$ over $[0,8]$, $s_{p,\text{8-26}}$ over $[8,26]$, $s_{p,\text{26-}end}$ over $[26, f_{\text{Nyq}}]$, and the total sound power $s_p$ over $[0, f_{\text{Nyq}}]$, where frequency limits are expressed in the same units used for the PSD (typically kHz when $f_s$ is specified in kHz). An additional sound-power feature, motivated by the experimental observations discussed in Sec. 4.5.2, was also introduced. This feature, denoted $s_{p,\text{filt}}$, was computed as the sum of the integrated power in the low- and high-frequency bands, i.e. over 0–8 and 26–$f_{\text{Nyq}}$. These frequency ranges were selected empirically during the analysis of the acoustic signals, and the corresponding feature was then included in the subsequent ML modelling. For the analysis of acoustic signatures as a function of process parameters, $s_p$ was selected.

Although it was not included in the subsequent ML modelling, a further spectral descriptor was computed for comparative analysis between welding conditions, namely the power spectral density quotient $Q$. This metric was evaluated *only for the acoustic emission (microphone) signal*, as it is intended to emphasise frequency-dependent differences in the emitted acoustic content. It quantifies, in decibels, the relative deviation of one spectrum with respect to a reference spectrum across the frequency axis [84]. Given two power spectral densities, $\hat{P}_1(f)$ (reference condition) and $\hat{P}_2(f)$ (comparison condition), the quotient is defined as

$$Q(f) = 10\log_{10}\left(\frac{\hat{P}_2(f)}{\hat{P}_1(f)}\right). \tag{4.14}$$

Positive values of $Q(f)$ indicate frequency bands where $\hat{P}_2(f)$ exhibits higher spectral content than $\hat{P}_1(f)$, whereas negative values denote the opposite, thereby highlighting the bands that contribute most to the spectral separation between the two welding conditions.

The features used for model training were selected using the Minimum Redundancy Maximum Relevance (MRMR) method. MRMR quantifies the mutual information between the class and each feature, defining the relevance of each fea-

ture. Simultaneously, MRMR evaluates redundancy between features. This method ranks features to maximise relevance while minimising redundant information. By reducing the feature space to a subset that is both informative and non-redundant, MRMR facilitates improved classifier performance and enhances interpretability of the underlying data structure [86].

### 4.4.4 Machine learning classification models

To classify the weld seams using features extracted from the acoustic and spectral signals, all available classification models in the MATLAB library were evaluated. For an initial pre-selection of suitable models, ten repetitions were performed. In each repetition, all models were trained and evaluated using stratified 5-fold cross-validation (CV). For each repetition, only the best-performing model (highest cross-validation accuracy, CVA) was retained. The final classifier for each task was selected as the model that occurred most frequently among the ten retained models. Model performance was assessed using CVA, F1 score, and recall. For selected classification tasks, class-wise metrics were additionally reported to provide a more detailed evaluation. Table 4.6 summarizes the considered models grouped by their underlying approach.

To ensure a fair and efficient evaluation, a two-stage approach to hyperparameter optimisation was adopted. In the first stage, all classifier algorithms were tested using the default (recommended) hyperparameters provided by the MATLAB implementations to identify models with the highest classification performance on the dataset. In the second stage, the analysis was restricted to the subset of top-performing models, for which targeted hyperparameter optimisation was carried out to further improve predictive performance. This step used MATLAB's built-in automated hyperparameter optimisation ("Optimize Hyperparameters"), which combines Bayesian optimisation with cross-validation to explore the hyperparameter space and identify a suitable configuration. The maximum number of objective evaluations (`MaxObjectiveEvaluations`) was set to 100.

For model training, the number of retained features was increased iteratively. The point at which classification performance ceased to improve (or began to decrease) was taken as the threshold for selecting the final number of features used in the model.

Table 4.6 Overview of ML classification models considered.

| **Category** | **Models** |
|---|---|
| Decision Trees | Coarse, Medium, Fine |
| Discriminant Analysis | Linear Discriminant, Quadratic Discriminant |
| Logistic Regression | Efficient Logistic Regression |
| Support Vector Machines (SVM) | Linear, Quadratic, Cubic, Fine Gaussian, Medium Gaussian, Coarse Gaussian |
| Naïve Bayes | Gaussian, Multinomial, Kernel Naive Bayes |
| Nearest Neighbors (k-NN) | Fine, Medium, Coarse, Cosine, Cubic, Weighted |
| Kernel Approximation | SVM Kernel, Logistic Regression Kernel |
| Ensembles | Boosted Trees, Bagged Trees, Subspace Discriminant, Subspace KNN, RUSBoost |
| Neural Networks (NNs) | Narrow, Medium, Wide, Bilayered, Trilayered |

## 4.5 Analysis of acoustic emissions

The following sections present the results of the acoustic-emission analysis acquired with the optical microphone, with the objective of linking variations in acoustic features to changes in welding regime and joint quality. The discussion is structured as follows. First, the effect of laser power at zero part-to-part gap is examined through the evolution of the sound-power feature $s_p$ and the corresponding spectral differences quantified via the PSD quotient $Q$. Second, the acoustic signature associated with piercing is isolated by introducing the filtered metric $s_{p,\mathrm{filt}}$. Finally, the influence of part-to-part gap—and its interaction with laser power—is analysed, and the observed cause–effect relationships are consolidated in a summary of the key phenomena.

### 4.5.1 Varying laser power

The results are organized to first examine the isolated effect of laser power at zero part-to-part gap, followed by the combined influence of laser power and part-to-part gap. Figure 4.6 shows how the weld geometrical features vary with laser power ($P_L$) under zero part-to-part gap conditions. At $P_L$ below 850 W, no melting was observed and only superficial marking appeared on the upper sheet. In the range 900–1000 W, the upper sheet melted, but the joint remained unconnected. Specifically, at 900 W the bottom sheet did not melt, whereas at 950 W melting initiated in the bottom sheet but remained insufficient to produce a sound connection. Sound connections were obtained between 1050 and 1350 W. At $P_L$ = 2000 W, laser piercing occurred, leading to a marked increase in weld width at the interface ($W_I$) and an excessive penetration depth ($D_E$).

Figure 4.7 depicts how the total sound power ($s_p$) evolves with increasing laser power ($P_L$) at zero part-to-part gap. At $P_L$ = 850 W, the sound power is minimal, consistent with a lack-of-fusion event. At $P_L$ = 900 W, the upper sheet starts melting, which is associated with a pronounced increase in acoustic emissions despite the lack of a sound connection. In the power range 1000–1050 W, the AE power continues to rise, corresponding to the transition from lack of connection to sound connection. The sound power then increases further between 1050 W and 1350 W. This behaviour is consistent with an increasingly energetic and sustained interaction, while the joint-quality class remains unchanged within the sound-connection regime. The trend is

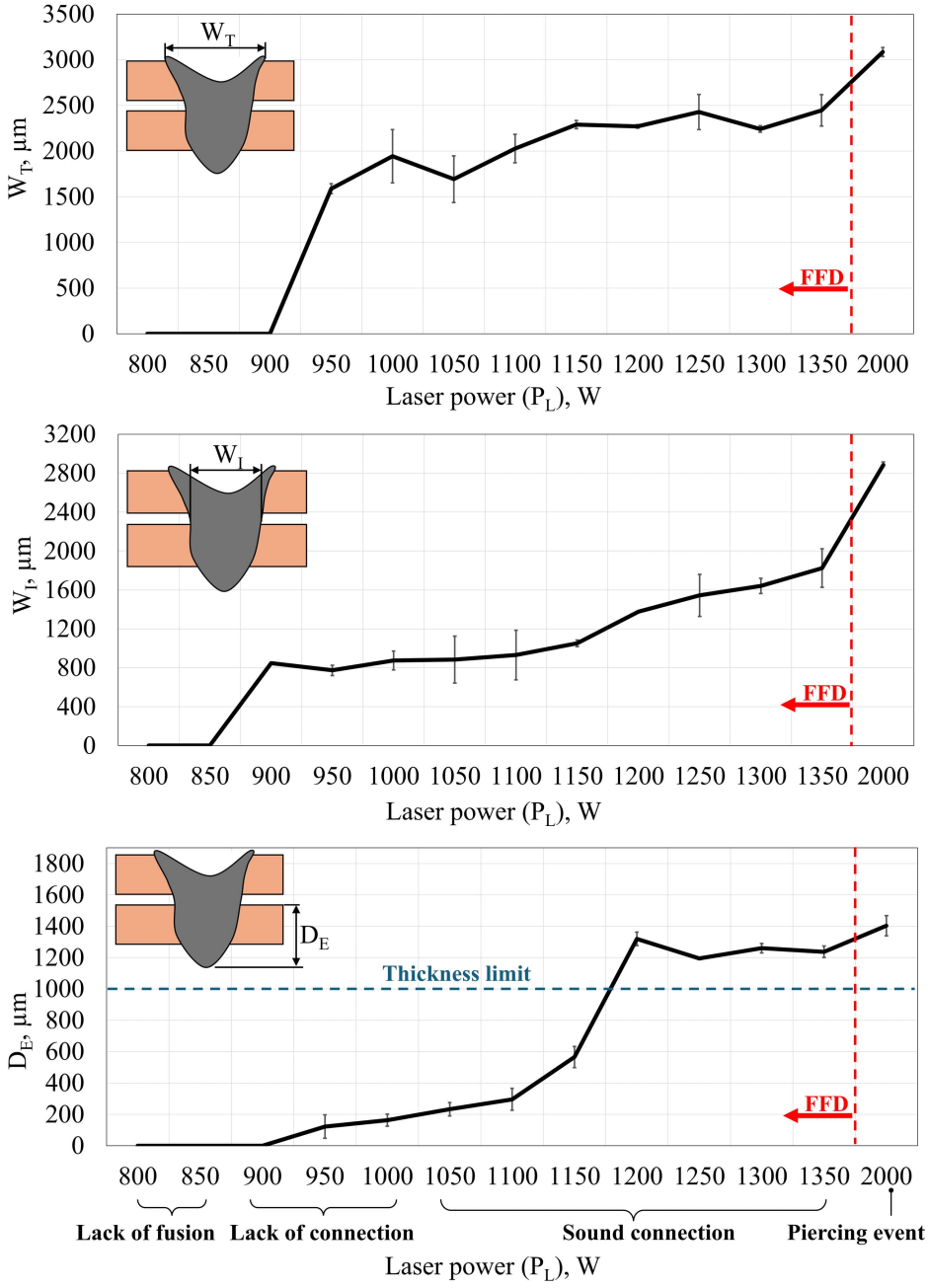


Fig. 4.6 Results of metallographic analysis at zero part-to-part gap. Pearson's correlation coefficients between $P_L$ and the weld features are 88% ($W_T$), 95% ($W_I$), and 93% ($D_E$). "FFD" indicates the process window tested by the full factorial design.

in line with earlier reports in the literature [69, 47]. A distinct jump in $s_p$ occurs at $P_L$ = 2000 W. Despite the relatively small changes in $s_p$ between adjacent power levels within the factorial window, a strong positive correlation (95%) is observed between $s_p$ and $P_L$, which is also mirrored by the variations in the geometrical features (Figure 4.6).

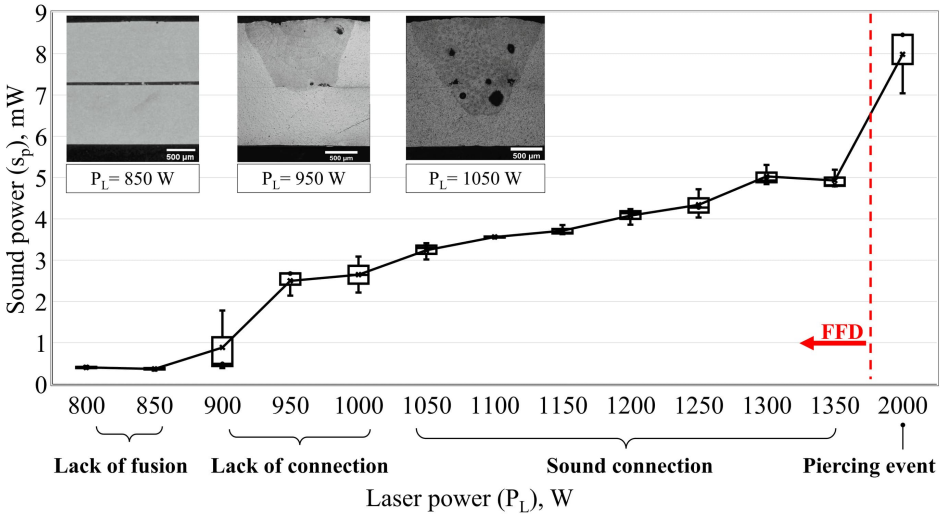


Fig. 4.7 Sound power ($s_p$) extracted from the ROI (all welds at zero part-to-part gap). "FFD" indicates the process window tested by the full factorial design. The selected cross-sections correspond to lack of fusion (850 W), lack of connection (950 W), and sound connection (1050 W).

The overall trend is consistent with the expectation that higher laser power induces more pronounced AE due to increased energy transfer to the material. To further analyse spectral differences in acoustic emissions between distinct welding regimes, PSD quotients ($Q$) were calculated between pairs of representative weld conditions. Three power levels were selected—850 W, 950 W, and 1050 W—corresponding to the key weld conditions identified through metallographic analysis: lack of fusion (850 W), lack of connection (950 W), and sound connection (1050 W). The first PSD quotient was computed between $P_L$ = 850 W and $P_L$ = 950 W and is shown in Figure 4.8(a). At $P_L$ = 850 W, the interaction is limited to superficial marking, with no melting and minimal acoustic activity. In contrast, $P_L$ = 950 W initiates melting of the upper sheet, even though no sound connection is achieved. This transition is consistent with the activation of additional mechanisms (e.g., melt-pool dynamics and plume-related phenomena), resulting in a broader and more

intense acoustic response. The PSD quotient highlights this shift, particularly in the 0–400 kHz range, with differences reaching up to 31 dB.

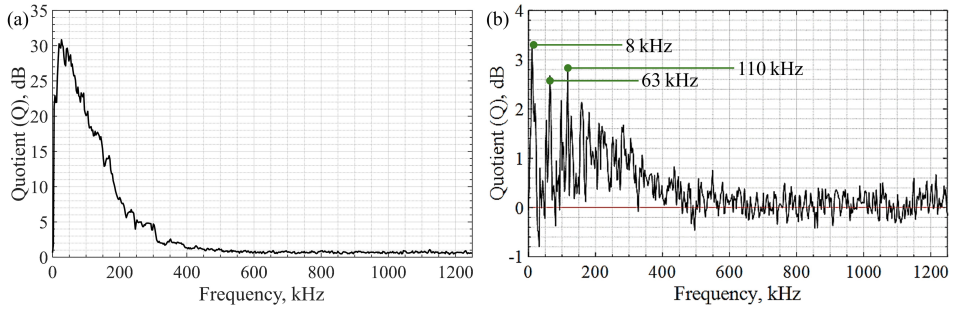


Fig. 4.8 (a) PSD quotient for $P_L$ = [850, 950] W; (b) PSD quotient for $P_L$ = [950, 1050] W (all welds at a zero part-to-part gap).

A second PSD quotient was computed between $P_L$ = 950 W ($PSD_1$) and $P_L$ = 1050 W ($PSD_2$) and is reported in Figure 4.8(b). For readability, a horizontal line at 0 dB is included to mark no difference between the two spectra. Positive values of $Q$ ($PSD_2 > PSD_1$) indicate that the frequency contribution in $PSD_2$ exceeds that of $PSD_1$, whereas negative values ($PSD_2 < PSD_1$) denote a lower contribution in $PSD_2$ compared to $PSD_1$.

At $P_L$ = 950 W, as noted earlier, both sheets melt but penetration remains insufficient; at $P_L$ = 1050 W, a sound connection is achieved. Within the 0–400 kHz range, the difference in dB is generally smaller than in the previous comparison (Figure 4.8(a)), with a maximum of 3.2 dB, suggesting that this band may carry information related to penetration changes around the transition to a sound connection. Three prominent peaks are present at 8 kHz, 63 kHz, and 110 kHz. The 63 kHz peak lies in a band often associated with keyhole penetration and has been linked to the onset of stable keyhole formation [47, 60, 69]. In this study, the appearance of a similar peak at $P_L$ = 1050 W suggests that a stable keyhole is more likely to form under these conditions. At higher frequencies, the PSD-quotient difference oscillates around zero, indicating reduced sensitivity of the higher-frequency content to this specific regime change.

The peaks at 8 kHz and 110 kHz observed at $P_L$ = 1050 W—where both upper and lower sheets are melted and an effective connection is established—indicate a slightly greater acoustic contribution at these frequencies compared to $P_L$ = 950 W, where melting is less effective in producing a connection. This behaviour may be associated with changes in melt volume and oscillatory dynamics as the interaction

becomes more stable. Nevertheless, a more detailed examination of these peaks is recommended in future studies.

### 4.5.2 Detection of piercing event at zero part-to-part gap

While the previous analysis described the progressive influence of increasing laser power on AE, a qualitatively different behaviour emerges when the process transitions from a blind to a passing-through keyhole, and therefore warrants separate evaluation. As shown in Figure 4.9, the 8–26 kHz band is the only frequency interval in which the spectrum at $P_L$ = 2000 W exceeds those at lower power levels. Over the remaining frequency range, the $P_L$ = 2000 W spectrum falls below the $P_L$ = 1350 W trace, which corresponds to full penetration without piercing. To analyse the AE trend while excluding the 8–26 kHz contribution, the sound power was recalculated by integrating the PSD over two bands (0–8 kHz and 26 kHz–$f_{\mathrm{Nyq}}$), and the resulting metric was denoted $s_{p,\mathrm{filt}}$:

$$s_{p,\mathrm{filt}} = s_{p,0\text{-}8} + s_{p,26\text{-}f_{\mathrm{Nyq}}}. \tag{4.15}$$

The trend of $s_{p,\mathrm{filt}}$ versus laser power is reported in Figure 4.10. Within the full-factorial window, $s_{p,\mathrm{filt}}$ increases with $P_L$; however, at $P_L$ = 2000 W (piercing), the filtered sound power exhibits a clear drop.

The observed drop indicates that, once a passing-through keyhole forms, the laser–material interaction is altered and broadband AE decreases, except within specific frequency bands. This behaviour is consistent with a reduction in energy confinement and a change in melt-pool/plume dynamics when the keyhole breaks through the bottom sheet. In particular, a passing-through keyhole can reduce effective absorptance and modify the distribution of recoil pressure and flow instabilities, which may in turn lower vibration-driven acoustic output over a large portion of the spectrum [87, 88]. Previous studies report similar observations. Li et al. [89] observed reduced AE under excessive penetration (piercing), attributing the effect to reduced confinement of vapour and plume when vapour can vent through the underside. Wei et al. [90] reported that, after variational mode decomposition, the amplitude in the 7.78–12.46 kHz band decreased markedly under excessive penetration relative to under- and nominal-penetration conditions. Consistent trends have also been reported in optical-emission studies during over-penetration. Jie et al. [91]

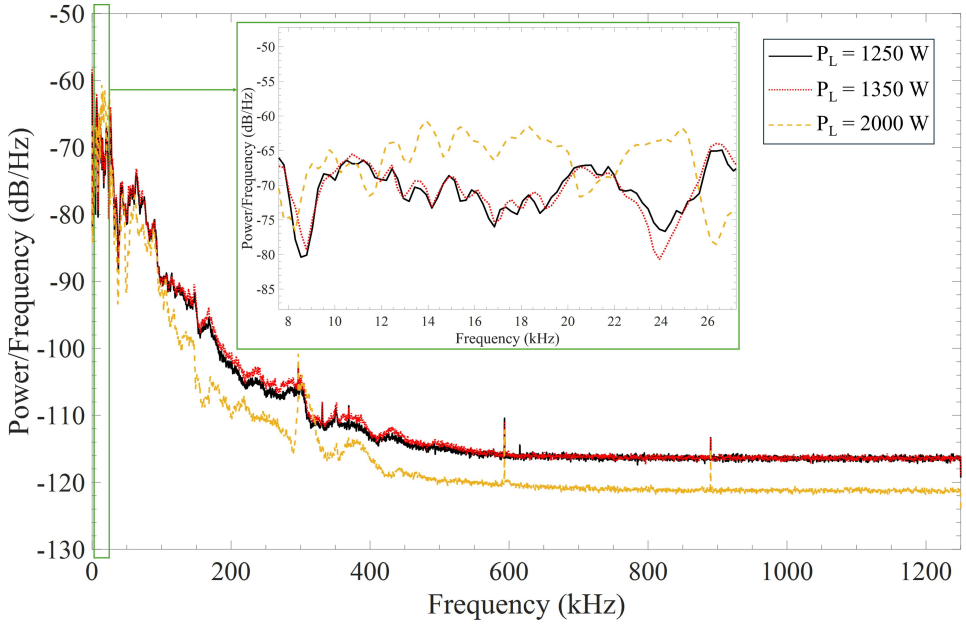


Fig. 4.9 PSD comparison for $P_L$ = 1250, 1350, 2000 W (all welds at zero part-to-part gap). The zoom-in view shows details in the 8–26 kHz range.

showed that plume area, centroid height, and radiance contract once excessive penetration occurs, attributing this to vapour venting through the underside such that the topside plume becomes smaller and cooler. Huang et al. [92] likewise reported an abrupt fall in electron temperature after the transition to over-penetration in Al–Mg arc welding, and Zhang et al. [93] observed a concomitant collapse of plume centroid height together with a redistribution of low-frequency dynamic content. The correlation between spectral emissions and AE is particularly noteworthy: Luo et al. [94] concurrently measured plasma electron temperature and both airborne and structure-borne acoustic signals and found that the three traces rise and fall together as the process shifts between conduction and keyhole regimes, indicating a direct coupling between plume dynamics and emitted acoustic energy. Collectively, these observations support the interpretation that keyhole breakthrough (piercing) reduces energy confinement and topside vapour/plume activity, which in turn weakens both plume signatures and broadband acoustic emissions.

While the filtered metric reveals a clear reduction in broadband AE at piercing, a distinct behaviour is observed within the 8–26 kHz range, where spectral content increases with laser power and remains elevated at $P_L$ = 2000 W (Figure 4.9). This contrasting trend suggests that additional mechanisms, partially decoupled from the

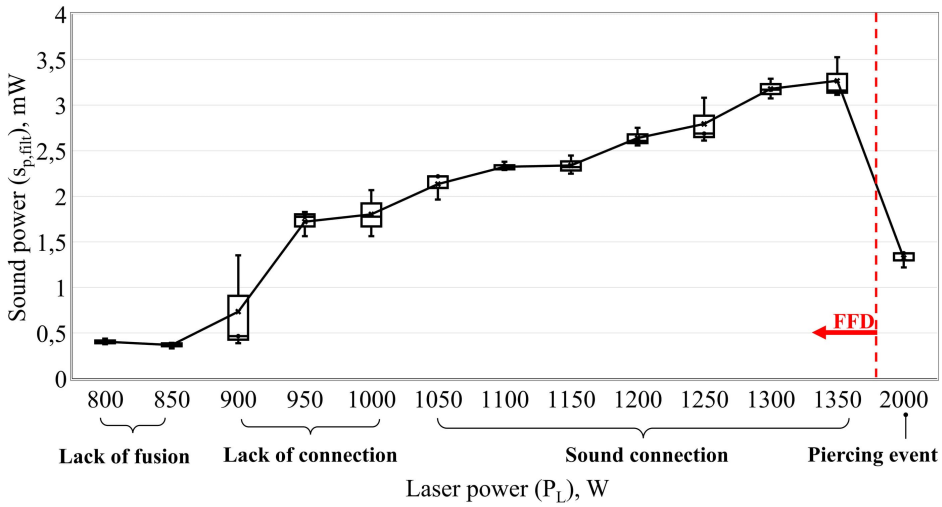


Fig. 4.10 Filtered sound power ($s_{p,\text{filt}}$), computed by excluding the 8–26 kHz band (all welds at zero part-to-part gap). "FFD" indicates the process window tested by the full factorial design.

broadband attenuation associated with breakthrough, contribute to acoustic activity in this band. Plausible contributors include:

- *Molten-pool dynamics and vapour-driven fluctuations:* increasing $P_L$ enhances melt-pool motion and vapour generation, which can increase low-frequency acoustic components linked to surface oscillations and plume–pool interactions [31].
- *Thermo-mechanical transients:* higher power intensifies thermal gradients and associated expansion/contraction dynamics, which can contribute to acoustic content in the low-kHz range, particularly in thin-sheet configurations where structural compliance is high [89, 95].

Therefore, while piercing attenuates broadband acoustic emissions (captured by $s_{p,\text{filt}}$), the 8–26 kHz band appears to retain sensitivity to high-energy interaction dynamics around breakthrough, highlighting its potential value for discriminating piercing events. Future work should validate whether the acoustic signatures observed during piercing remain consistent across broader materials, optical configurations, and process windows.

### 4.5.3 Varying part-to-part gap

This section investigates the influence of part-to-part gap on AE. For the sake of discussion, the metallographic analysis of two representative laser-power levels is reported in Figure 4.11 (a). At $P_L$ = 1150 W, a connection occurred only for gap levels of 0, 0.25, and 0.5 mm, whereas no connection was achieved for larger gaps. At $P_L$ = 1350 W, a connection between the two parts was achieved for all gap levels except 1 mm.

The effectiveness of the weld connection is governed by the interaction between delivered laser energy, molten-pool transport, and gap size. Small gaps (0–0.25 mm) promote thermal coupling between the upper and bottom sheets and facilitate localized melting at the interface, enabling metallurgical bonding. As the gap increases, interfacial heat transfer becomes less efficient and the molten material must bridge a larger discontinuity, which increases the likelihood of incomplete fusion and lack of connection [96]. For gaps above 0.5 mm, the melt volume and flow can become insufficient to maintain a continuous bridge, particularly at lower power, so the joint remains unconnected. At $P_L$ = 1350 W, the higher energy input increases melt-pool volume and fluidity, thereby improving the ability to bridge larger gaps (up to 0.75 mm) through a combination of wetting/capillary effects and gravity-driven flow [97]. Nevertheless, at the extreme gap of 1 mm the molten-pool dynamics remain insufficient to sustain bridging, leading again to lack of connection.

To maintain consistency with the findings discussed in Section 4.5.1, the acoustic metric was computed by excluding the 8–26 kHz band, and $s_{p,\mathrm{filt}}$ was evaluated accordingly. Figure 4.11 (b) shows the variation of $s_{p,\mathrm{filt}}$ as a function of part-to-part gap for the power levels that produced a sound connection at zero gap (Figure 4.10). A relatively strong negative correlation (Pearson's correlation coefficient = 79.7%) was found between part-to-part gap (considering all tested power levels) and $s_{p,\mathrm{filt}}$, indicating that AE decrease as the gap increases. This trend is consistent with the sensitivity of acoustic emissions to interfacial conditions: increasing gap introduces an open path at the faying interface that can promote venting and reduce pressure build-up, thereby decreasing confinement of the vapour/plume above the weld zone and lowering the associated broadband acoustic energy [96, 58].

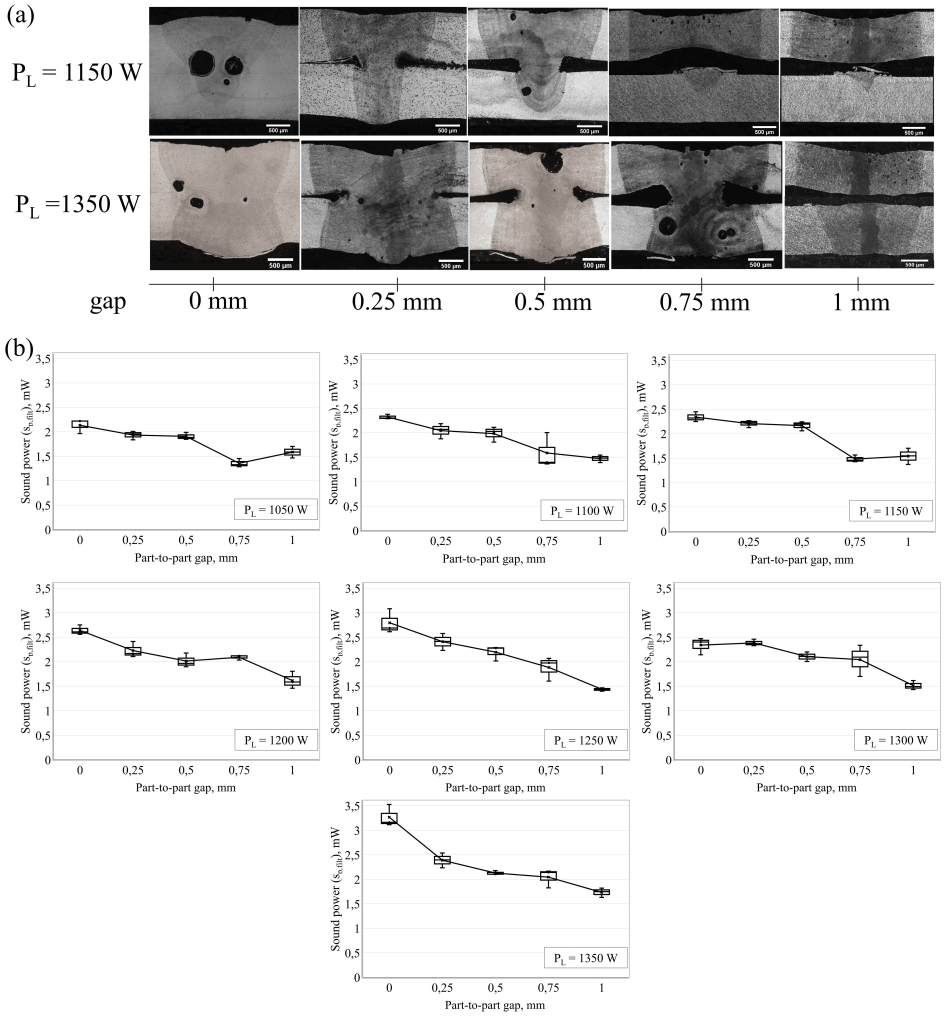


Fig. 4.11 (a) Macro-sections for $P_L$ = 1150 and 1350 W at variable gap levels; (b) filtered sound power ($s_{p,\mathrm{filt}}$) computed by excluding the 8–26 kHz band at varying part-to-part gap.

### 4.5.4 Combined effect of laser power and part-to-part gap on acoustic emissions

This section evaluates how the interaction between laser power and part-to-part gap influences AE and weld quality. To maintain consistency with the metrics introduced in the previous sections, sound power was computed from the acoustic signals by excluding the 8–26 kHz band (denoted $s_{p,\text{filt}}$). To quantify the combined influence of laser power and part-to-part gap on the acoustic response measured by the optical microphone, a two-way ANOVA was conducted. This approach allows testing both the main effects of part-to-part gap (five levels: 0–1 mm) and laser power ($P_L$, twelve levels: 800–1350 W) and their interaction. The interaction term is particularly relevant because the effect of laser power is expected to depend on the gap level, e.g. due to changes in interfacial heat transfer, melt-pool bridging, and venting at the faying interface. The ANOVA results, summarized in Table 4.7, show that both main factors and their interaction (all p-values below the 5% significance level) significantly affect $s_{p,\text{filt}}$. The corresponding partial effect sizes ($\eta^2$) indicate that laser power explains the largest portion of variance, followed by part-to-part gap, with a moderate yet statistically significant interaction effect.

Table 4.7 Two-way ANOVA results of laser power, part-to-part gap and related interaction.

| **Source** | **df** | **Sum Sq** | **Mean Sq** | **F** | **p** | **Partial $\eta^2$** |
|---|---|---|---|---|---|---|
| Part-to-part gap | 4.0 | 0.06084 | 0.01521 | 31.99 | 0.0001 | 0.42 |
| $P_L$ | 11.0 | 0.32225 | 0.02930 | 61.57 | 0.0001 | 0.73 |
| Part-to-part gap × $P_L$ | 44.0 | 0.04879 | 0.00111 | 2.33 | 0.0001 | 0.28 |
| Residual | 120.0 | 0.05714 | 0.00048 | | | |

Table 4.8 reports the marginal means (with 95% confidence intervals) for each gap level, averaged over all laser-power levels.

Overall, $s_{p,\text{filt}}$ spans a relatively narrow numerical range (approximately 0.05–0.06 mW), yet systematic trends are observed with both process parameters. In aggregate, $s_{p,\text{filt}}$ increases with rising $P_L$ (Pearson's correlation coefficient = 82%), which is consistent with the expectation that higher energy input intensifies the acoustic response and agrees with the zero-gap trend discussed in Section 4.5.1. The interaction effect is reflected in the differing slopes of $s_{p,\text{filt}}$ versus $P_L$ at different gaps. For small gaps (0.00 and 0.25 mm), $s_{p,\text{filt}}$ increases more steeply with laser power

Table 4.8 Marginal means of sound power by gap level with 95% CI.

| **Part-to-part gap** | **Mean $s_{p,\mathrm{filt}}$** | **95% CI Lower** | **95% CI Upper** |
|---|---|---|---|
| 0.00 | 0.0548 | 0.0526 | 0.0570 |
| 0.25 | 0.0579 | 0.0558 | 0.0601 |
| 0.50 | 0.0607 | 0.0585 | 0.0629 |
| 0.75 | 0.0534 | 0.0513 | 0.0555 |
| 1.00 | 0.0541 | 0.0520 | 0.0562 |

(Figure 4.11 (b)), consistent with stronger thermal coupling and a more efficient transfer of energy across the interface, which can amplify molten-pool dynamics and associated acoustic activity. Conversely, at larger gaps (0.75 and 1.00 mm), $s_{p,\mathrm{filt}}$ increases more gradually with $P_L$, and for a given power level the mean acoustic response tends to decrease with increasing gap. This trend is consistent with reduced melt bridging and enhanced venting at the faying interface, which can relieve pressure build-up and reduce plume confinement, attenuating broadband acoustic emissions [58]. The combined observations can be summarized as follows:

- For small gaps ($\lesssim 0.5$ mm), laser power is the dominant factor and $s_{p,\mathrm{filt}}$ increases approximately monotonically with $P_L$.
- For larger gaps, the effectiveness of gap bridging decreases and venting at the interface becomes more pronounced, which attenuates the acoustic response and reduces the sensitivity of $s_{p,\mathrm{filt}}$ to increasing $P_L$ [58].

Figure 4.12 summarises $s_{p,\mathrm{filt}}$ for all combinations of laser power and gap evaluated in this study, visually reinforcing the trends discussed above. The variability (error bars) is more pronounced in combinations close to regime transitions (intermediate power and gap levels), suggesting less stable process conditions and greater sensitivity to small perturbations.

Based on empirical inspection of the acoustic-emission dataset, two indicative $s_{p,\mathrm{filt}}$ thresholds were identified for separating weld-quality classes:

- A lower threshold of 0.5 mW separates lack of fusion ($s_{p,\mathrm{filt}} < 0.5$ mW) from conditions with melting but insufficient connection (lack of connection, 0.5 mW $< s_{p,\mathrm{filt}} <$ 1.8 mW).

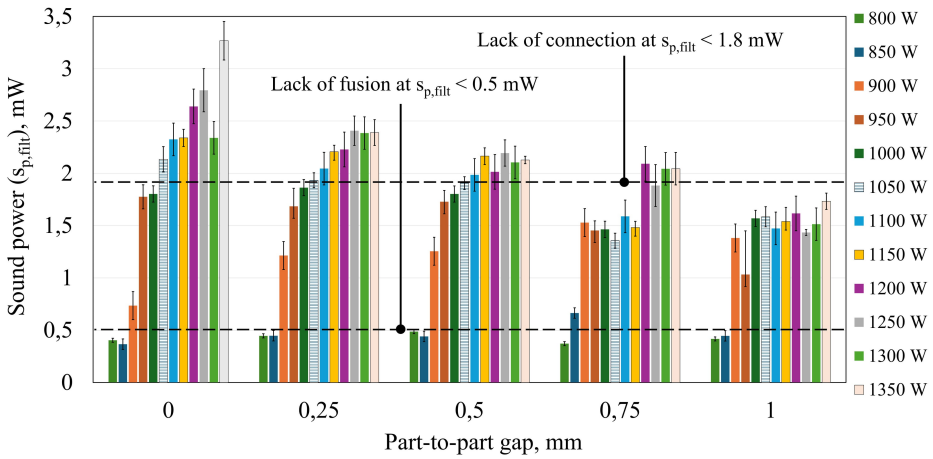


Fig. 4.12 Sound power ($s_{p,\text{filt}}$) computed by excluding the 8–26 kHz band, shown for all combinations of laser power (800–1350 W) and part-to-part gap (0–1 mm).

- A higher threshold of 1.8 mW separates lack of connection from stable, effective weld conditions (sound connection, $s_{p,\text{filt}} > 1.8$ mW).

While these thresholds provide a compact acoustic criterion for weld-quality discrimination, cases close to the boundaries—particularly between lack of connection and sound connection—may still be misclassified. This is expected when joint morphology and process dynamics lead to partially overlapping acoustic responses that are not fully captured by a single scalar feature. Accordingly, the subsequent classification analysis complements thresholding by combining multiple acoustic descriptors (and, where applicable, feature-level fusion with photodiode features) to improve robustness across the full process window.

### 4.5.5 Summary of observed cause–effect phenomena

The key findings are summarized in Table 4.9, highlighting the relationships between laser power, part-to-part gap, the resulting welding phenomena, and the corresponding AE signatures.

The observed variations in acoustic emissions recorded by the optical microphone are strongly influenced by the interplay between laser power, part-to-part gap, and the resulting keyhole and melt-pool dynamics. At low laser powers ($P_L < 800$ W), insufficient energy delivery leads to lack of fusion, manifested by low-amplitude

Table 4.9 Summary of welding events and corresponding cause–effect relationships observed during laser welding of 1 mm 1050 aluminium.

| Event | Cause | Effect |
|---|---|---|
| **LoF** | Low laser power | No melting; only surface marking<br>$s_{p,\mathrm{filt}} \approx 0.5$ mW |
| **LoC** | Low laser power<br>Large part-to-part gap | Weak or unstable melt-pool dynamics<br>Attenuation of acoustic emissions due to venting at the part-to-part interface<br>$s_{p,\mathrm{filt}}$ decreases below $\sim 1.8$ mW (after excluding 8–26 kHz) |
| **SoC** | Adequate laser power<br>Small/medium gap | Effective and stable weld fusion<br>$s_{p,\mathrm{filt}} \gtrsim 1.8$ mW<br>A peak around 63 kHz is consistent with stable keyhole dynamics |
| **Piercing** | Excessive laser power | Transition to a passing-through keyhole reduces energy confinement and can decrease broadband AE<br>$s_{p,\mathrm{filt}}$ decreases below $\sim 1.8$ mW |

acoustic signals. This is consistent with prior work indicating that minimal or absent melting produces weak pressure fluctuations and therefore limited acoustic activity [70]. As laser power increases beyond the melting threshold and sound connections are obtained ($P_L = 1050$–$1350$ W), the development of a stable keyhole and more energetic melt-pool oscillations is accompanied by a pronounced increase in acoustic amplitude and structured spectral content. In particular, the emergence of a characteristic peak around 63 kHz is consistent with a resonance-like response of the keyhole cavity and has been associated with keyhole-related dynamics in previous studies [69, 47].

At substantially higher power ($P_L = 2000$ W), the transition from a blind to a passing-through keyhole (piercing) is marked by a drop in broadband acoustic emissions after excluding the 8–26 kHz band, in agreement with the "venting" interpretation reported in the literature [89, 90]. Once a continuous channel forms through the sheets, pressure confinement above the weld is reduced and vapor/plume can vent through the underside, which weakens both acoustic and optical emissions observed from the topside [91]. Notably, this loss-of-confinement mechanism produces an acoustic attenuation that is qualitatively similar to that observed when the part-to-part

gap becomes large, underscoring that distinct fault scenarios can converge to similar AE trends when they reduce vapor and pressure confinement.

The response of the acoustic signal to variations in gap size can be rationalized in the same framework. Small to moderate gaps (up to 0.5 mm) preserve interfacial coupling and promote heat transfer and melt bridging, which are reflected by larger and more repeatable acoustic responses. For larger gaps ($> 0.5$ mm), the interface increasingly acts as a vent, dispersing vapor and reducing confinement, thereby suppressing the acoustic amplitude and its sensitivity to process variations, consistent with observations reported for gap-related instabilities [96, 58]. From a monitoring perspective, these results demonstrate the feasibility of using membrane-free optical microphones for real-time detection of critical weld conditions, including transitions associated with insufficient fusion and piercing. The strong links observed between acoustic features and weld outcomes provide a quantitative basis for in-process monitoring, while further work should address industrial deployment aspects such as increased ambient noise and broader process variability.

## 4.6 Machine learning classification and feature-level fusion

The following sections evaluate supervised classification performance obtained from the two sensing modalities considered in this study—photodiode-based spectral emissions and optical-microphone acoustic emissions—and then quantify the impact of combining them through feature-level fusion. Results are presented first using photodiode-derived features only and then using acoustic-derived features only. In both cases, the same feature-selection and model-selection workflow is applied to establish modality-specific baselines. Finally, the fused feature set is analysed and benchmarked against the single-sensor cases to determine whether combining complementary emissions improves discrimination of the weld-quality classes.

### 4.6.1 Spectral features: classification performance

This subsection reports the supervised classification results obtained using only the photodiode-derived features (plasma emission $p$ and back-reflection $r$). Following

the feature extraction procedure described in Sec. 4.4.3, the resulting feature vectors were ranked using the mRMR criterion, and model development was performed using the top-ranked subset to limit dimensionality and reduce overfitting risk. Model performance was assessed through $k$-fold cross-validation (CV) on the training set and subsequently evaluated on a hold-out test set, which was not used during training. Finally, an automated hyperparameter optimisation step was carried out for the best-performing classifiers, and the tuned models were re-trained and re-evaluated using the same protocol.

The mRMR ranking obtained after class balancing is reported in Table 4.10. The top positions are dominated by robust dispersion and distribution-shape descriptors, notably $r_{IQR}$, $r_{kurt}$, and $p_{kurt}$. This indicates that the discriminative information for weld-quality classes is primarily encoded in changes of the amplitude distribution of both photodiode signals within the selected ROI, rather than in a single absolute intensity metric. Several ranked features (e.g., *IQR*, *MAD*, $\sigma$, skewness, kurtosis, median/mode) are expected to be partially correlated because they describe related aspects of the same underlying distribution; in this sense, mRMR is advantageous because it promotes features that are simultaneously relevant to the class labels while penalising redundant candidates. A further consistent observation is that the zero-crossing rate (ZCR) receives negligible importance for both channels. This is expected because photodiode waveforms are typically positively biased and remain above zero, such that sign changes are rare and ZCR carries limited discriminative information.

Model training was performed using the top three ranked features (Table 4.10). This choice provides a compact and interpretable input space while preserving most of the discriminative power indicated by the mRMR ranking. A range of supervised classifiers was initially screened, and the three best-performing and algorithmically diverse models were retained for hyperparameter optimisation; their performance is summarised in Table 4.11, where *Before* and *After* denote results obtained prior to and following hyperparameter tuning, respectively.

The top three classifiers retained after screening were a bilayer neural network (NN Bilayered), a Coarse Tree, and a Quadratic Discriminant classifier. Their confusion matrices are reported in Fig. 4.13, while the corresponding accuracies are summarised in Table 4.11. In Table 4.11, *Before* indicates the baseline model trained

Table 4.10 Photodiode Features Ranking (Plasma & Back Reflection) after Class Balancing

| **Rank (#)** | **Feature** | **Score (%)** |
|---|---|---|
| 1 | $r_{IQR}$ | 8.6957 |
| 2 | $r_{kurt}$ | 8.0884 |
| 3 | $p_{kurt}$ | 7.7865 |
| 4 | $p_{MAD}$ | 7.1932 |
| 5 | $r_{mode}$ | 7.1566 |
| 6 | $p_{skew}$ | 6.9408 |
| 7 | $p_{median}$ | 6.2013 |
| 8 | $r_{skew}$ | 5.9405 |
| 9 | $p_{mode}$ | 4.8956 |
| 10 | $p_{IQR}$ | 4.7765 |
| 11 | $r_{\sigma}$ | 4.6586 |
| 12 | $p_{STE}$ | 4.5193 |
| 13 | $r_{STE}$ | 4.4280 |
| 14 | $p_{\sigma}$ | 4.2354 |
| 15 | $r_{MAD}$ | 4.0536 |
| 16 | $p_{mean}$ | 3.8941 |
| 17 | $r_{median}$ | 3.5885 |
| 18 | $r_{mean}$ | 2.9475 |
| 19 | $p_{ZCR}$ | 0.0000 |
| 20 | $r_{ZCR}$ | 0.0000 |

with default hyperparameters, whereas *After* reports the performance obtained after hyperparameter optimisation and re-training.

Overall, all three models achieve high cross-validated accuracy and comparable test-set accuracy, suggesting that the selected top-$k$ features capture a substantial portion of the class-discriminative information in the photodiode signals. However, the effect of hyperparameter optimisation is not uniformly beneficial on the hold-out test set. For instance, the NN Bilayered model exhibits a slight increase in CV accuracy after optimisation, but a small decrease in test accuracy; similarly, the Coarse Tree shows a noticeable drop in test performance after tuning. Such discrepancies can arise when the optimisation procedure improves average robustness across CV folds, while the held-out test split represents a slightly different sample realisation. This behaviour is common in limited-size experimental datasets and underscores why both CV and independent test metrics should be reported when discussing generalisation.

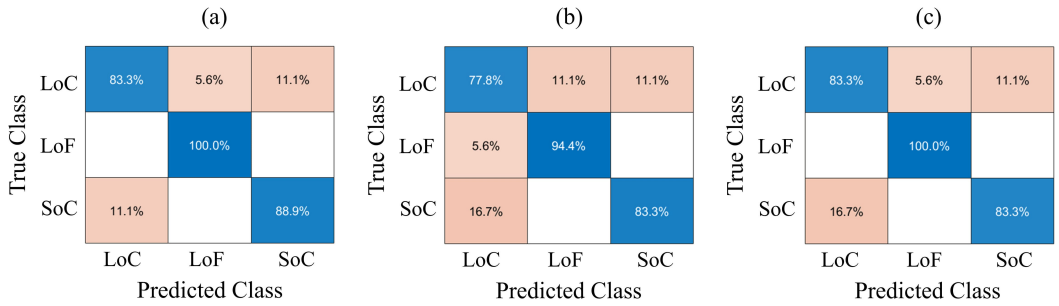


Fig. 4.13 Confusion matrices for the best-performing photodiode-only models: (a) NN Bilayered; (b) Coarse Tree; (c) Quadratic Discriminant.

Table 4.11 Top three photodiode ML models (using the top-ranked features).

| **Model** | **Before** | | **After** | |
|---|---|---|---|---|
| | **CV (%)** | **Test (%)** | **CV (%)** | **Test (%)** |
| NN Bilayered | 92.60 | 91.67 | 93.03 | 90.74 |
| Coarse Tree | 92.59 | 90.74 | 92.13 | 85.19 |
| Quadratic Discriminant | 91.20 | 88.89 | 91.20 | 88.89 |

### 4.6.2 Acoustic features: classification performance

This subsection reports the supervised classification results obtained using only the acoustic-emission features extracted from the optical microphone signal. After class balancing (as described in the previous section), the acoustic feature set was ranked using the mRMR criterion; the resulting ranking is reported in Table 4.12. In contrast to the photodiode-only case, a larger subset of features was retained for model training (top 10 features) in order to capture both distribution-shape descriptors and band-limited energy metrics that encode complementary aspects of the acoustic signature. The top-ranked feature is the filtered sound-power metric

Table 4.12 Microphone Features Ranking after Class Balancing

| **Rank (#)** | **Feature** | **Score (%)** |
|---|---|---|
| 1 | $s_{p,\text{filt}}$ | 10.9140 |
| 2 | $s_{skew}$ | 10.0270 |
| 3 | $s_{mode}$ | 9.9541 |
| 4 | $s_{mean}$ | 7.5379 |
| 5 | $s_{median}$ | 6.3760 |
| 6 | $s_{ZCR}$ | 6.3185 |
| 7 | $s_{STE}$ | 6.3082 |
| 8 | $s_{p,\text{8-26}}$ | 6.3082 |
| 9 | $s_{kurt}$ | 6.0804 |
| 10 | $s_{p,\text{0-8}}$ | 5.4073 |
| 11 | $s_{MAD}$ | 5.3199 |
| 12 | $s_{p,\text{26-}end}$ | 5.2794 |
| 13 | $s_p$ | 5.1161 |
| 14 | $s_\sigma$ | 4.8294 |
| 15 | $s_{IQR}$ | 4.2236 |

$s_{p,\text{filt}}$, which is consistent with the process-driven motivation discussed in Sec. 1.5: by excluding frequency bands dominated by non-informative components, $s_{p,\text{filt}}$

emphasises acoustic variations associated with regime changes (including transient events such as piercing) more effectively than the broadband power $s_p$. Several of the other highly ranked descriptors (e.g., $s_{skew}$, $s_{mode}$, $s_{mean}$, $s_{median}$, $s_{kurt}$) are partially correlated by construction because they quantify related properties of the same amplitude distribution. Similarly, the band-power features ($s_{p,0\text{-}8}$, $s_{p,8\text{-}26}$, $s_{p,26\text{-}end}$) can be mutually redundant when the spectral content shifts uniformly. The mRMR ranking is therefore useful because it promotes features that are simultaneously relevant to the class labels while discouraging redundant combinations, yielding a compact subset that preserves diversity across statistical and spectral representations.

Using the selected acoustic features, a range of supervised classifiers was screened and the three best-performing and algorithmically diverse models were retained for deeper analysis and hyperparameter optimisation. Table 4.13 summarises the performance of the selected models, where *Before* and *After* indicate results obtained prior to and following hyperparameter tuning, respectively; corresponding confusion matrices are reported in Fig. 4.14.

Table 4.13 Top three microphone ML models (using the selected acoustic features).

| **Model** | **Before** | | **After** | |
|---|---|---|---|---|
| | **CV (%)** | **Test (%)** | **CV (%)** | **Test (%)** |
| Coarse Tree | 92.59 | 90.74 | 93.03 | 94.44 |
| RUSBoosted Trees | 92.59 | 96.30 | 92.59 | 96.30 |
| Bagged Trees | 90.28 | 98.15 | 92.59 | 94.44 |

Overall, the acoustic-only models achieve high accuracy, with test-set performance ranging from 90.74% to 98.15% before tuning. Hyperparameter optimisation improves generalisation for the Coarse Tree (test accuracy increases to 94.44%), whereas the RUSBoosted Trees model remains stable, suggesting that its default configuration is already well-matched to the feature space and dataset size. In contrast, the Bagged Trees model shows a reduction in test accuracy after tuning despite improved CV accuracy, which is indicative of variance effects in limited-size datasets: optimisation favours configurations that perform more consistently across training folds, but may not coincide with the specific characteristics of a single hold-out split. For this reason, both CV and test metrics are reported and interpreted jointly; a detailed class-wise error analysis based on the confusion matrices is deferred to the dedicated discussion on false positives and false negatives.

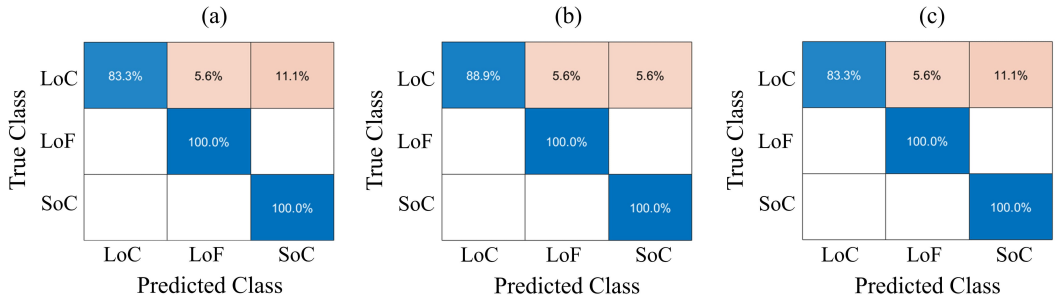


Fig. 4.14 Confusion matrices for the best-performing acoustic-only models: (a) Coarse Tree; (b) RUSBoosted Trees; (c) Bagged Trees.

### 4.6.3 Feature-level fusion: combined model performance

This section shows the results of feature-level fusion, to understand if weld-quality classification improves when combining photodiode-derived spectral descriptors and optical-microphone acoustic descriptors within a single feature vector. The mRMR ranking was computed *jointly* over the pooled feature set from both sensors, such that relevance and redundancy were assessed not only within each modality but also *across* modalities. The top-ranked fused features are reported in Table 4.14. Based on this ranking, the top 30 features were retained to train and compare a set of supervised classifiers using the same cross-validation and hold-out test protocol adopted in Secs. 4.6.2, 4.6.1.

The fused mRMR ranking highlights that the most informative predictors originate from *both* modalities.

The top position is occupied by the acoustic filtered sound-power metric $s_{p,\mathrm{filt}}$, consistent with the acoustic-only case and confirming its strong sensitivity to regime-dependent process dynamics. However, several photodiode descriptors are also selected among the highest ranks (e.g., $r_{mean}$, $p_{kurt}$, $p_{median}$, $r_{kurt}$), indicating that optical emissions provide complementary information that is not fully redundant with the acoustic statistics. Importantly, the joint mRMR selection mitigates the tendency to include multiple highly correlated descriptors (e.g., simultaneous inclusion of several dispersion metrics) by penalising redundant candidates; nevertheless, some residual redundancy is expected because both modalities respond to common physical drivers such as keyhole stability and plume behaviour. As observed previously, ZCR-related features for the photodiodes remain non-informative (scores equal to zero), whereas the acoustic ZCR retains non-negligible importance.

Table 4.14 Features Ranking (Fused Dataset)

| **Rank (#)** | **Feature** | **Score (%)** |
|---|---|---|
| 1 | $s_{p,\text{filt}}$ | 5.9965 |
| 2 | $r_{mean}$ | 5.7690 |
| 3 | $s_{mean}$ | 5.5810 |
| 4 | $s_{skew}$ | 4.8285 |
| 5 | $s_{mode}$ | 3.8774 |
| 6 | $p_{kurt}$ | 3.6315 |
| 7 | $p_{median}$ | 3.5432 |
| 8 | $r_{kurt}$ | 3.4140 |
| 9 | $p_{skew}$ | 3.3282 |
| 10 | $s_{p,\text{0-8}}$ | 2.9352 |
| 11 | $r_{\sigma}$ | 2.9005 |
| 12 | $p_{IQR}$ | 2.8468 |
| 13 | $s_{kurt}$ | 2.8183 |
| 14 | $p_{mode}$ | 2.7780 |
| 15 | $r_{skew}$ | 2.7491 |
| 16 | $r_{IQR}$ | 2.6466 |
| 17 | $r_{mode}$ | 2.6335 |
| 18 | $p_{STE}$ | 2.5510 |
| 19 | $s_{median}$ | 2.5305 |
| 20 | $s_{ZCR}$ | 2.5022 |
| 21 | $p_{MAD}$ | 2.4972 |
| 22 | $s_{STE}$ | 2.4944 |
| 23 | $s_{p,\text{8-26}}$ | 2.4944 |
| 24 | $r_{median}$ | 2.4377 |
| 25 | $p_{mean}$ | 2.3862 |
| 26 | $r_{MAD}$ | 2.3494 |
| 27 | $p_{\sigma}$ | 2.3240 |
| 28 | $s_{MAD}$ | 2.3146 |
| 29 | $s_{p}$ | 2.3119 |
| 30 | $r_{STE}$ | 2.2949 |
| 31 | $s_{p,\text{26-}end}$ | 2.2269 |
| 32 | $s_{\sigma}$ | 2.1961 |
| 33 | $s_{IQR}$ | 1.8115 |
| 34 | $p_{ZCR}$ | 0.0000 |
| 35 | $r_{ZCR}$ | 0.0000 |

The three best-performing and algorithmically diverse fused models are summarised in Table 4.15, while the corresponding confusion matrices are reported in Fig. 4.15. Hyperparameter optimisation is beneficial for the Bagged Trees classifier, improving both CV and test accuracy (up to 94.44% on the hold-out set), and it also increases the test accuracy of the linear SVM. Conversely, RUSBoosted Trees exhibits only marginal changes after tuning, suggesting limited sensitivity to hyperparameters within the explored search space for this dataset.

Table 4.15 Top three fused ML models ranking

| **Model** | **Before** | | **After** | |
|---|---|---|---|---|
| | **CV (%)** | **Test (%)** | **CV (%)** | **Test (%)** |
| SVM Linear | 93.52 | 90.74 | 92.59 | 92.59 |
| RUSBoosted Trees | 93.06 | 88.30 | 91.67 | 88.89 |
| Bagged Trees | 91.67 | 92.59 | 93.98 | 94.44 |

When comparing across modalities, feature-level fusion proves *beneficial relative to photodiode-only classification*, as it yields higher and more consistent test performance than the best photodiode-only models reported in Sec. 4.6.1. However, fusion does *not* surpass the best acoustic-only performance observed in Sec.4.6.2, where the microphone features already provide a highly discriminative representation of the weld-quality classes. This outcome is plausible for two reasons. First, when one modality is already near-sufficient for class separation, additional features may contribute limited incremental information and can instead increase model variance, especially under limited sample size. Second, feature-level fusion increases dimensionality and introduces cross-sensor correlations; although mRMR reduces redundancy, the added degrees of freedom can still favour models that fit subtle split-specific characteristics rather than improving true generalisation. In this sense, the fused results support a nuanced conclusion: multi-sensor integration enhances performance compared to using photodiode emissions alone, but the gain over acoustic-only monitoring is modest under the present experimental conditions and dataset size. A class-wise interpretation based on false positives/negatives and the confusion matrices is deferred to the dedicated error-analysis discussion.

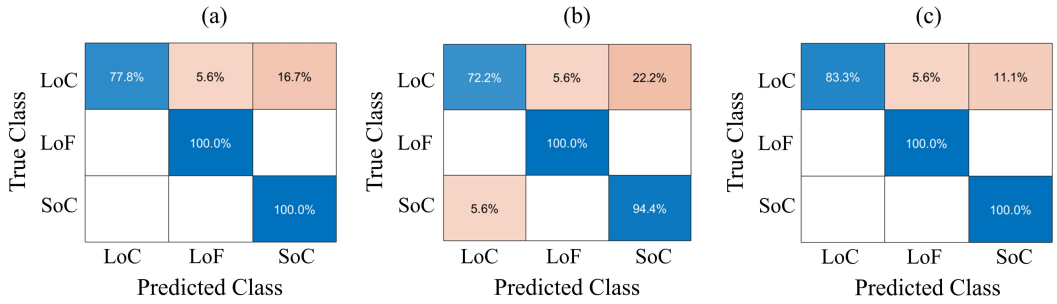


Fig. 4.15 Confusion matrices for the best-performing fused models: (a) SVM Linear; (b) RUSBoosted Trees; (c) Bagged Trees.

## 4.7 Conclusions

This case study assessed sensor-based monitoring of remote laser welding of 1 mm AA1050 overlap joints, representative of busbar-to-terminal connections in battery modules, using a membrane-free optical microphone and (in a second stage) photodiode-based spectral-emission sensing. The results demonstrate that process emissions can be leveraged to infer local keyhole condition and weld-event transitions across the conduction-to-keyhole spectrum, including the critical transition from a *blind* to a *passing-through* keyhole (piercing). This provides a process-scale link that complements the weld-section and component-scale perspectives addressed in the subsequent case studies.

A first key finding is that acoustic emissions evolve systematically with laser power and correlate with the onset of melting and stable penetration. At zero part-to-part gap, the total sound power $s_p$ increased with $P_L$, reflecting progressively stronger melt-pool/keyhole dynamics as the process transitions from lack of fusion to lack of connection and then to sound connection. Frequency-domain comparisons further supported this interpretation: the PSD-quotient analysis highlighted clear spectral separation between regimes and revealed characteristic contributions (including peaks in bands previously associated with keyhole dynamics), consistent with the emergence of stable keyhole behaviour as penetration becomes sufficient for a sound connection.

A second major contribution is the demonstration that the optical microphone can diagnose the transition from a blind to a passing-through keyhole. Dedicated tests at $P_L = 2000$ W (zero gap) produced piercing, confirmed via a check-surface positioned

below the joint. While broadband $s_p$ increased with power, isolating the response outside the 8–26 kHz band through the filtered metric $s_{p,\mathrm{filt}}$ revealed a clear *drop* at piercing. This behaviour is consistent with a loss of confinement and altered laser–material interaction when the keyhole breaks through, which reduces plume/pressure build-up above the surface and attenuates broadband acoustic activity. Importantly, the results indicate that different frequency bands do not respond uniformly at piercing, motivating band-selective metrics rather than reliance on a single broadband descriptor.

Part-to-part gap was shown to be another strong driver of acoustic response, with $s_{p,\mathrm{filt}}$ decreasing as gap increased, consistent with venting at the interface and weakened coupling/bridging. A two-way ANOVA confirmed that laser power, gap, and their interaction significantly influence $s_{p,\mathrm{filt}}$, reinforcing that monitoring strategies should account for coupled process effects rather than treating parameters independently. From a monitoring perspective, these results support the use of acoustic features as sensitive indicators of keyhole/melt-pool stability and of loss-of-confinement mechanisms shared by distinct fault modes (excessive gap and piercing).

Machine-learning classification and feature-level fusion provided a quantitative benchmark of defect discrimination capability. Photodiode-only models achieved high accuracy but were outperformed by acoustic-only models (test accuracy up to 98.15% with the optical microphone). Feature-level fusion improved performance relative to photodiodes alone (test accuracy up to 94.44%), confirming cross-modality complementarity; however, fusion did not exceed the best acoustic-only performance. This suggests that, for the present dataset and operating envelope, the microphone features already encode most of the separability among LoF/LoC/SoC, and that adding features may yield diminishing returns under limited sample size.

Several limitations define the boundary conditions of the present conclusions. To isolate the effects of laser power and gap, cross-jet was intentionally excluded and measurements were performed in a laboratory environment with moderate background noise; industrial deployment will require systematic evaluation under stronger acoustic disturbances (auxiliary equipment, ventilation, cross-jet flow) and robust real-time processing strategies that preserve weld-relevant content without suppressing informative bands. Moreover, while the study establishes experimentally grounded correlations between emissions and weld events (including piercing), the reported thresholds and classification performance should not be assumed universal:

they depend on sensor placement, optical configuration, material condition, and the explored parameter space, and should be re-qualified when transferring the approach to new setups.

Overall, this case study demonstrates that membrane-free optical-microphone sensing can provide practical indicators of keyhole condition and of transitions from conduction to blind keyhole welding and to passing-through keyhole (piercing).

# Chapter 5

# Case study 2 – Monitoring penetration depth in hybrid laser–arc welding using optical coherence tomography

## 5.1 Introduction

This chapter examines Optical Coherence Tomography (OCT) for in-process monitoring of hybrid laser–arc welding (HLAW) to measure keyhole penetration depth and behavior, with the aim of evaluating the sensor's reliability across different process conditions and configurations. This section establishes the industrial context by outlining the motivation for penetration-depth monitoring in hybrid welding of structural steels. It then reviews prior work on OCT-based monitoring in laser welding and frames the open challenges associated with extending OCT to hybrid laser–arc welding.

Hybrid laser–arc welding (HLAW) couples a high-energy laser with an arc source to deliver deep penetration at high travel speeds while the arc supplies filler and gap-bridging; in practice this means fewer passes, lower heat input and distortion, and better fit-up tolerance for medium- to thick-section steels used in long seams and girth welds [4]. More detailed explanationon HLAW is reported in 2.3. From an industrial KPI perspective, hybridization targets simultaneous gains in throughput, quality,

and resource efficiency at production scale. Reported projections for integrated hybrid systems include ∼15% shorter machining time, ∼25% lower filler wire usage, ∼15% savings in energy and shielding gas, ∼33% higher productivity, ∼15% fewer repairs, and ∼15% lower residual stresses—benefits that translate directly into cost, schedule, and dimensional-control advantages on long seams and girth welds [98]. As pipeline and panel welds are often produced in demanding onshore/offshore settings—and because hybrid laser–arc welding couples two heat sources whose parameters interact (e.g., laser power/focus, travel speed, arc current/voltage, wire feed, arc–laser distance, shielding, joint fit-up)—rigorous quality assurance is essential [4]. Accordingly, inline process monitoring can be used to provide continuous, weld-synchronous indicators of stability and penetration information, enabling prompt corrective action and reducing reliance on sampled, post-process inspection. The literature on monitoring in hybrid laser–arc welding (*HLAW*) remains sparse; the few available studies focus almost exclusively on imaging, which permits only surface inspection and provides no information about subsurface phenomena within the weld joint [28, 99].

In this context, Optical Coherence Tomography (OCT) is a strong candidate: integrated coaxially with the processing laser, it acquires high-rate, depth-resolved profiles that provide micrometer-resolution information on weld penetration and seam geometry, and its feasibility for laser deep-penetration welding has been demonstrated from laboratory to pilot scale [100]. More detailed explanation on OCT is reported in section 3.2.3 Mittelstadt et al. [101] employed otical OCT to measure the keyhole depth during the laser welding of 5083 aluminum alloy and mild steel. The research demonstrated that OCT measurements carry information from not only the keyhole bottom but also from other welding features that interact with the measuring beam, including keyhole opening, keyhole walls, keyhole waves, and multiple reflected measuring radiation. Test results revealed that materials with varying reflectivities produced distinct measurements, requiring specific filtering parameters for each material. A histogram evaluation method was employed to analyze the data, indicating that a greater local maximum correlates with a more robust measure. Schmoeller et al. [102] performed a preliminary investigation on how the material, the angle of incidence, and the shape of the joint affect the quality of the signal during laser welding using OCT. This was due to the different ways the materials melted and how they reflected and absorbed light. Statistical analysis showed that the OCT signal depended on all of the parameters that were looked

at. The findings were validated with single-mode fiber laser welding, where the processing beam and the OCT measuring beam had similar spot sizes ($\sim$55 $\mu m$). The results confirmed the feasibility of inline weld depth monitoring using OCT for both multimode and single-mode laser systems and underscored the sensitivity of the measurement system to material- and process-specific effects. Sokolov et al. [103] employed OCT to monitor the weld depth penetration during remote laser welding of Al-Cu battery tab connectors, using an adjustable ring mode (ARM) laser. The study applied the Keyhole Mapping method to solve the problem of precisely aligning the OCT measuring beam with the bottom of the keyhole, where the most accurate measurements can be made, even though the shape of the keyhole changes over time. The OCT beam was split in two—one aimed at the keyhole bottom and the other at the part surface. Results showed how the position of the beam with respect the laser TCP had a strong influence, with the best measurement window being only 20 $\mu m$ wide. The study additionally discussed how the shape of the keyhole changes depending on the material and how the oct signal changes accordingly due to different reflections of keyhole walls. Beck et al. [104] studied the use of OCT to measure the depth of a keyhole while microwelding copper with a green laser. The authors introduced a scanning pattern of the OCT beam parallel to the weld direction, measuring at multiple spatial locations. The results showed that the highest signal intensity and greatest measured depths were always seen in a position behind the laser beam. The findings showed how the trailing distance between the laser processing beam and the measuring beam depended on the process parameters and increased with the laser power and welding speed. In deep penetration welding, capillary depth showed a strong correlation with cross-sectional weld depth, with absolute differences ranging from 22 $\mu m$ to 62 $\mu m$ for welds between 200 $\mu m$ and 600 $\mu m$. Conversely, no reliable correlation was observed in heat conduction mode. Werner et al. [105] examined the influence of laser beam incidence angle on the precision of OCT measurements during steel overlap welding, obtaining good results for all the inclination angles in the range of $\pm$30°C. Moreover, a post-processing method was proposed to compensate for geometric distortions induced by the inclined setup. Their method involved transforming the depth data from the inclined coordinate system to the sheet orientation and a filtering algorithm based on histogram weighting.

While OCT has been increasingly adopted for in-process monitoring of LW, its application to HLAW remains unexplored. The complex interactions among the laser

beam, the electric arc, and the molten pool—together with the additional optical disturbances generated by arc plasma and metal vapor—raise uncertainty regarding the extent to which OCT can reliably measure keyhole depth during hybrid welding. Moreover, no studies have reported on the application of OCT for monitoring butt joint welds.

## 5.2 Objectvies

To address these gaps, the following study aim to demonstrate the feasibility of OCT-based monitoring in *HLAW* and to delineate the sensor's operational envelope. To the best of the author's knowledge, this is the first report of OCT applied to butt-joint welding and the first demonstration of a commercially available monitoring sensor integrated into a *HLAW* system.

## 5.3 Experimental program

The study comprised three experimental stages:

1. The first stage involved laser-only bead-on-plate welding, with the laser power ($P_L$) varied from 1 kW to 12 kW. This allowed a systematic evaluation of the OCT depth measurement capability, revealing a maximum reliable detection depth of approximately 6 mm—corresponding to $P_L$ of 6 kW—beyond which the signal became increasingly unstable.

2. The second stage consisted of bead-on-plate hybrid laser–arc welding (*HLAW*), with $P_L = 6$ kW changing the relative distance between the laser and the arc, and mantaining all the other parameters constant. Configurations were selected to span the range from fully hybrid operation to tandem welding, with both laser-leading and arc-leading arrangements tested. Furthermore, because variations in the laser–torch distance ($D_{LT}$) modify the underlying process physics, the sensitivity of the OCT measurements to these induced changes was evaluated.

3. In the third stage, the tests were repeated in a butt-joint configuration with the laser leading. By varying ($D_{LT}$) and $P_L$, three distinct conditions were deliberately produced, simulating defects such as lack of fusion, excessive

penetration, and root humping. This approach enabled an evaluation of OCT performance under more realistic and industrially relevant joint geometries.

## 5.4 Experimental Setup

The experimental setup for *HLAW* and *OCT* is shown in figure 5.1 and the details are reported in table 5.1. The welding experiments were conducted on S355 steel and comprised three stages, as reported in table 5.2: in stages 1 and 2, bead-on-plate configurations were employed, whereas in stage 3, the welds were performed in a butt-joint configuration. The laser source was an nLight CFL-12000 with a maximum power of 12 kW and a wavelength of $1070 \pm 10$ *nm* The original optical fiber had a core diameter of 100 µm, which was coupled to a 300 µm fiber using a fiber coupler, delivering the beam to an MPH Photonic Tools laser head with a magnification of 4. This configuration resulted in a laser spot diameter of 1.2 mm and a Rayleigh length of 28 mm, yielding a relatively large laser beam with low divergence. The GMAW setup employed a Fronius TPS500i and a fronius arc torch, mounted on a custom holder to ensure precise alignment and controlled distance with respect to both the laser beam and the workpiece. The OCT sensor used was the Lessmüller OCT scanner MRB, mounted coaxially to the laser beam. The OCT laser operated in the $840 \pm 10$ $\mu m$ wavelength range with an output power of 30 mW and, according to the manufacturer's specifications, produced a spot size of approximately 10 $\mu m$. The entire setup was mounted on a 6-axis Fanuc M-710iC/50 industrial robot. A Cavitar camera was used to record the welding process and qualitatively assess its dynamics; it served solely as a visual aid and was not used for further analysis.

To compare the OCT signal with the actual outcome, metallographic cross-sections were prepared from the specimens—sectioned, polished, and etched to reveal the weld zone. Macrographs were acquired by optical microscopy, and weld depth was measured from the top surface to the point of maximum penetration in each macrograph (see fig. 5.2-(a) )

For the butt-welding tests, the specimens were 8 mm thick and prepared with a single-V chamfer at 37.5 ° with a 2 mm root face, yielding an effective penetration thickness of 6 mm. The focal positions of both the processing laser and the OCT beam were set at the bevel root (i.e., the lowest point of the chamfer) (see Fig. 5.2-(b)).

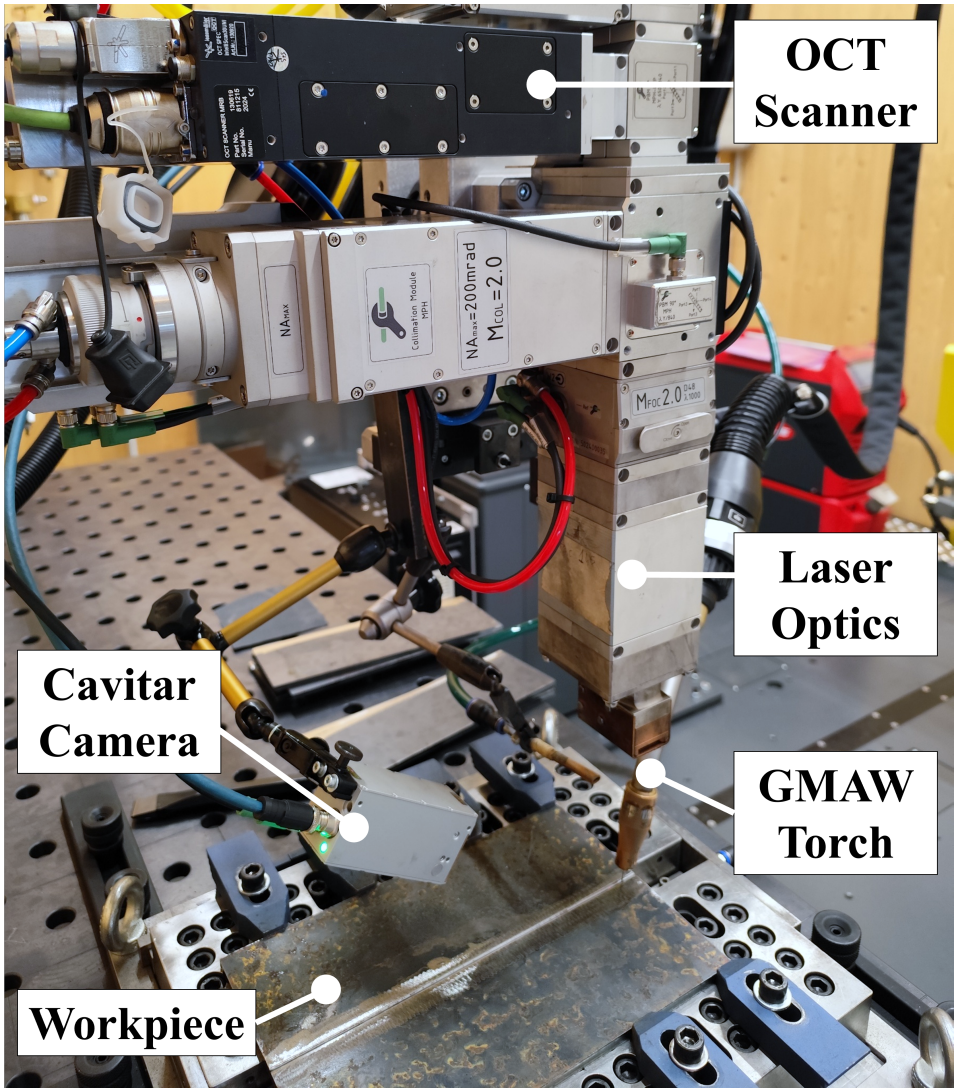


Fig. 5.1 Setup for Hybrid Laser-Arc Welding (HLAW) and Optical Coherence Tomography (OCT)

Table 5.1 Specifications of the HLAW and OCT system.

| **Laser welding setup** | | | |
|---|---|---|---|
| **Laser nLight CLF-12000** | | **Optic Photonic Tools M4** | |
| Maximum power | 12 kW | Max. allowed power | 20 kW |
| Wavelength | $1070 \pm 10$ nm | Collimation length | 100 mm |
| Fiber diameter | 100 $\mu$m | Focal length | 400 mm |
| Processing fiber diameter (exit of beam expander) | 300 $\mu$m | Rayleigh length | 28 mm |
| BPP | 11.5 mm $\cdot$ mrad | Spot size | 1200 $\mu$m |
| Laser mode | Multi-mode | | |
| **GMAW setup** | | | |
| **Arc source Fronius TPS 500i** | | **Torch Fronius** | |
| Maximum Current | 500 A | Filler wire | PURUS |
| Maximum Voltage | 400 V | Filler wire diameter | 1 mm |
| | | Shielding gas | M21 |
| **OCT setup - Lessmueller IntelliScan30UNI** | | | |
| Maximum power | | | 30 mW |
| Wavelength | | | $840 \pm 20$ nm |
| Maximum frequency rate | | | 250 kHz |
| Fiber core diameter | | | 5.5 $\mu m$ |

### 5.4.1 OCT Sensor setup

As explained in section 3.2.3 OCT can operate in static mode or scanning mode. In this study scanning mode is employed and the scanning strategy is illustrated in Figure 5.3. Two scanning paths were employed: one parallel to the welding direction (x-scan) and one perpendicular to it (y-scan). Each scanning line was 1 mm collecting 400 points per scan obtaining a local measurement resolution of 2.5 $\mu m$,and they both were centered on the laser TCP. The OCT surface measurement beam for the reference was positioned 5 mm ahead of the laser TCP.

A 10% brightest pixel threshold was applied in the software to filter out weak, low-confidence signals, and the surface scan was subtracted from the OCT data. Figure 5.4 presents an example of the scans from a laser welding test conducted at 6 kW laser power and a travel speed of 0.8 m/min, where each black point corresponds to a OCT measurement. To reveal the actual weld depth from the raw points post-processing is required.

Table 5.2 Materials and welding configuration

| Stage | Material | Configuration | Parameters |
|---|---|---|---|
| 1 | S355 - 200x100x15 mm | Bead-on-plate | • Laser only<br>• 12 runs<br>• 1 to 12 kW<br>• HLAW |
| 2 | S355 - 200x100x15 mm | Bead-on-plate | • 6 Runs<br>• Laser-leading<br>• Arc-leading<br>• Laser power 6 kW |
| 3 | S355 - 200x100x8 mm | Butt-joint | • HLAW<br>• 3 runs<br>• Laser-leading<br>• Laser power 6 kW |

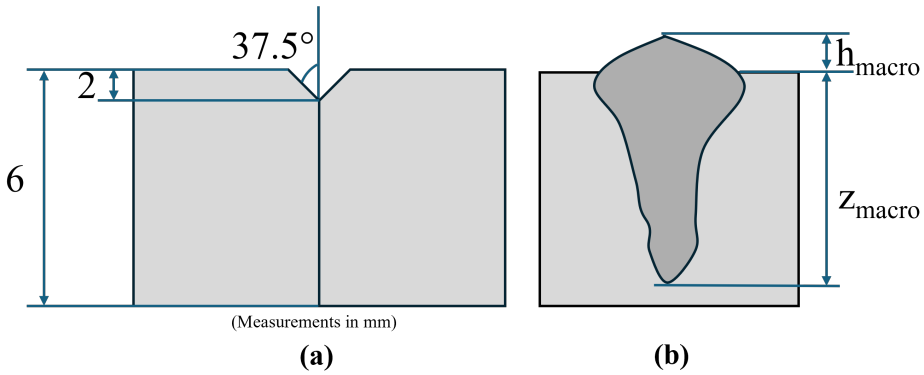


Fig. 5.2 **a)** Schematic (not in scale) of Welding configuration for butt-joint tests with 8 mm total thickness (2 mm chamfer with a 37.5 ° angle); **b)** Schematic of the measurements from the macrography specimen $z_{macro}$ measuring the weld depth from the top surface to the bottom of the welding and $h_{macro}$ measuring the excess weld metal.

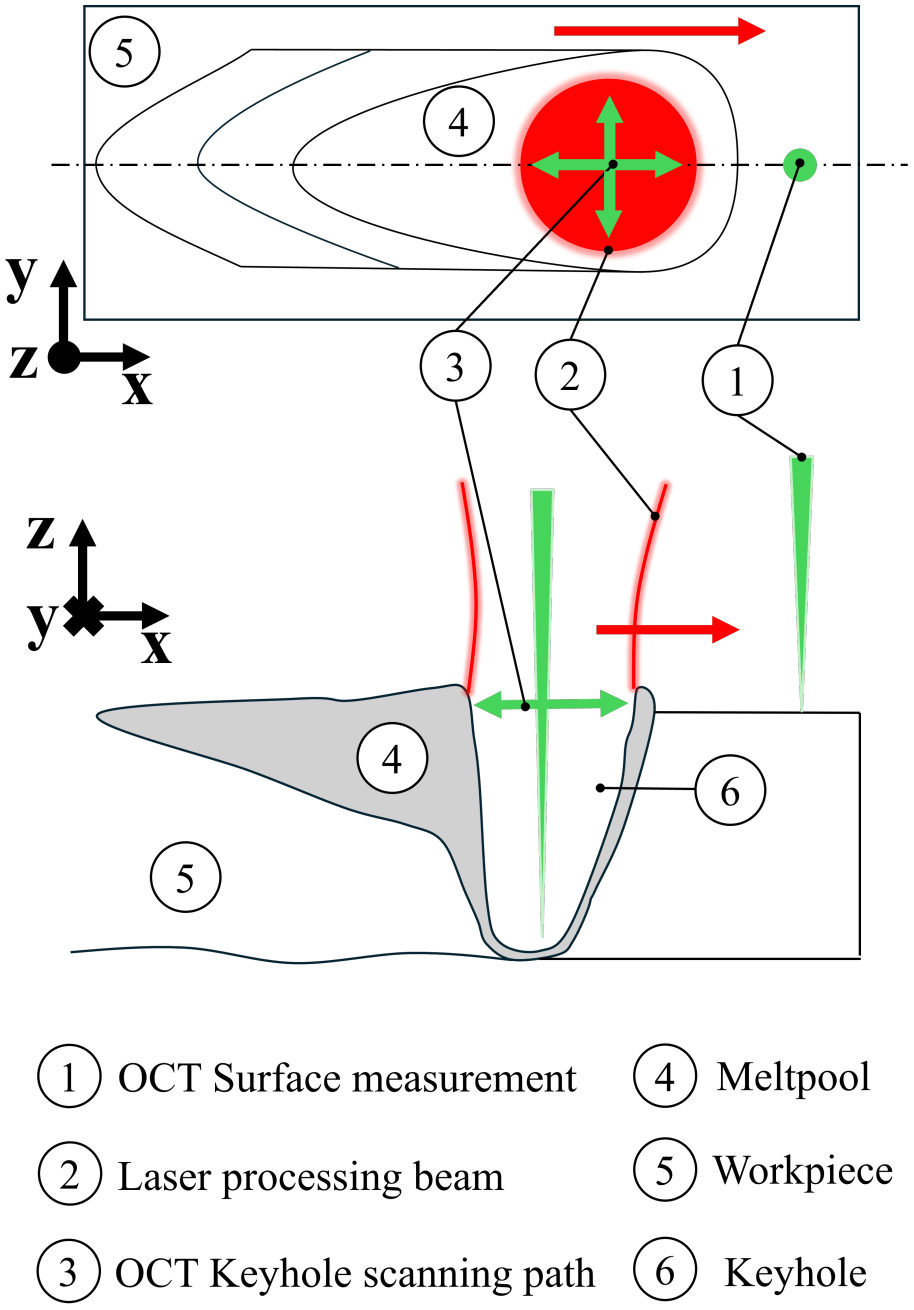


Fig. 5.3 OCT Scanning strategy during laser welding

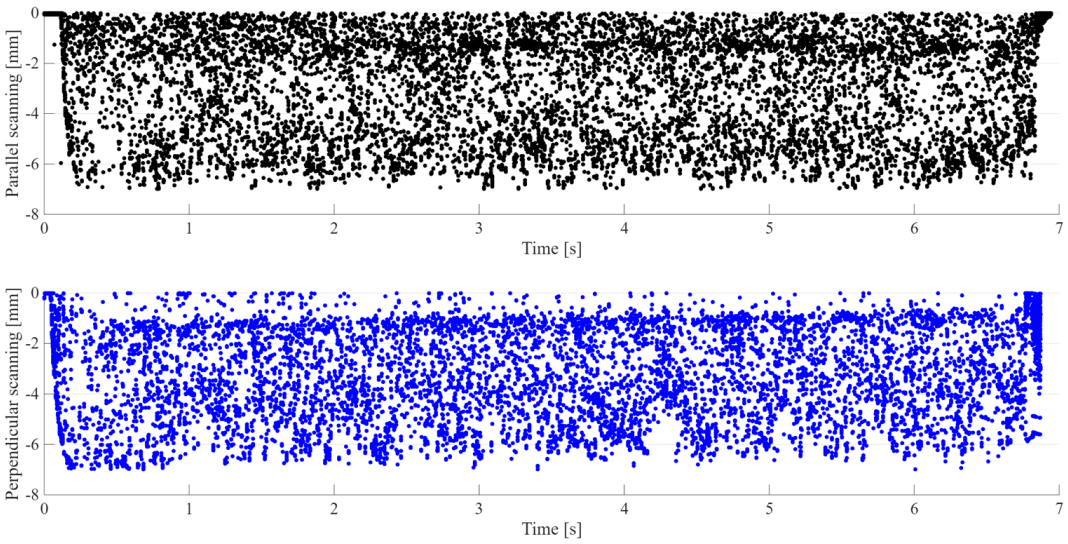


Fig. 5.4 Example of the two scans along parallel and perpendicular direction laser power 6 kW and travel speed 0.8 m/min

One practical challenge with OCT is defining the keyhole measurement location, which typically lies $\sim$ 0.2–0.5 mm behind the laser TCP, depending on focus position, travel speed, and plume dynamics. Determining this offset is usually iterative and requires several trial runs [100]. Adopting a one-dimensional, coaxial line-scan at the laser tool center point (TCP), implemented both parallel and perpendicular to the travel direction—addresses this limitation. The extended scan path maximizes the likelihood of intersecting the keyhole bottom (i.e., the point of maximum penetration), thereby capturing the true depth while mitigating errors due to minor system misalignment. In addition, it reduces the need for calibration trials based on destructive macrographic cross-sections, with corresponding savings in time and cost.

## 5.5 Signal Processing

### Local Support Window Algorithm

Each black point in Fig. 5.4 represent a measurement along the scan line of the oct sensor. Since the measurement beam travels through the keyhole bottom, the sidewalls, and the free surface, the detection set could include non-bottom echoes.

Plume-induced reflections, multiple scattering, and imaging artefacts (like auto-correlations and speckle-related white noise) are included in the raw signal [106, 107]. This problem gets more severe by long line-scan trajectories, which is why the dedicated filtering and tracking algorithms described below are needed.

Prior studies have employed density-based algorithms such as DBSCAN to cluster OCT returns and suppress noise. DBSCAN defines clusters as regions of sufficient point density, governed by a neighborhood radius $\varepsilon$ and a minimum number of samples ($min_{samples}$); points in low-density regions are labeled as noise. This makes it effective for discovering arbitrarily shaped clusters while rejecting sparse outliers [108, 109]. However, DBSCAN is poorly matched to the present objective—selecting, for each scan line, the keyhole bottom and verifying that it is not a side-wall or spurious echo. DBSCAN solves a clustering problem rather than a per-line extremum problem; it returns cluster labels with no guarantee that the cluster contains the line-wise deepest point. In addition, true bottoms can be intermittent and sparse, so valid detections may be labeled as noise when they fail a global $min_{samples}$ threshold. Finally, return density varies along long line scans; a single choice of $\varepsilon$ and $min_{samples}$ cannot accommodate this variability without either merging distinct structures or discarding valid sparse regions [110].

To address these issues, a *Local Support Window* (LSW) algorithm is introduced, tailored to line-scan OCT in welding. For each scan line $l(i)$: (i) select the candidate bottom $z^*$ as the most negative valid return along $l(i)$; (ii) construct a two-dimensional neighborhood $\Omega(\ l(i),\ z^*;\ \varepsilon)$: a disk of radius in the scan plane centered at the candidate; (iii) test for local support, requiring at least $k$ neighboring returns within $\Omega$ whose depths lie within a tolerance band around $z^*$ and remain below the surface reference; and (iv) optionally enforce temporal continuity across adjacent scans to suppress flicker. The candidate is accepted as the keyhole bottom only if the local-support criterion is met; otherwise, the algorithm evaluates the next deepest candidate [111].

A schematic representation of the method is shown in Figure 5.5, where the raw OCT depth signals are illustrated together with the selected keyhole trajectory. The figure demonstrates how local minima are initially identified within sliding windows and then validated through elliptical neighbor support.

Figure 5.6 shows the raw OCT data with the output of the proposed local-support filtering and tracking for both scanning directions. The post-processed set exhibits

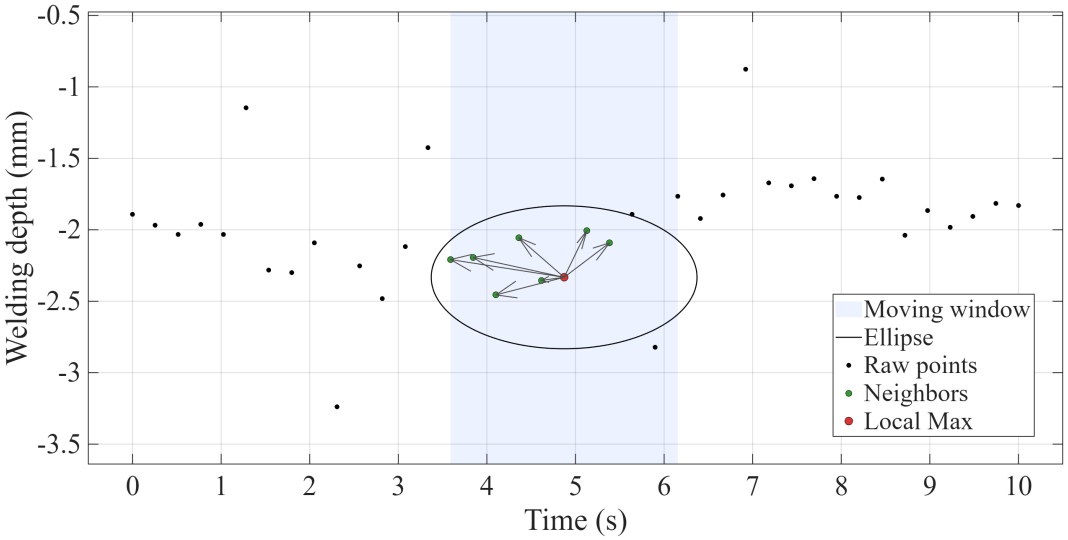


Fig. 5.5 Local Support Window (LSW) validation: an elliptical neighborhood in time–depth centered at the candidate $(t_i, z^\star(t_i))$.

markedly fewer points, with isolated side-wall and plume-induced echoes removed and a more continuous estimate of the bottom trajectory. While the reduction in point count yields a lighter data stream suited to online monitoring, it is crucial that the retained points preserve the true penetration signature rather than reflect a selection bias.

## Percentile Filtering

Following pre-processing to remove outliers, the final weld-depth trajectory is extracted using a nonlinear statistical filtering method—the percentile filter. This technique has been widely tested and assessed as the best for processing raw OCT signals [100].

Let $z^\star(t_i)$ denote the sequence of validated depth estimates at times $t_i$, $i = 1, \ldots, N_t$. For each sample $i$, a centered temporal window $\mathscr{H}_i$ of half–length $H$ is defined as

$$\mathscr{H}_i \;=\; \{\, z^\star(t_k) \mid \max(1, i-H) \le k \le \min(N_t, i+H) \,\}. \tag{5.1}$$

The filtered depth $\tilde{z}(t_i)$ is then given by the $P$-th percentile of the samples within the window:

$$\tilde{z}(t_i) \;=\; \text{percentile}\left(\mathscr{H}_i, P\right). \tag{5.2}$$

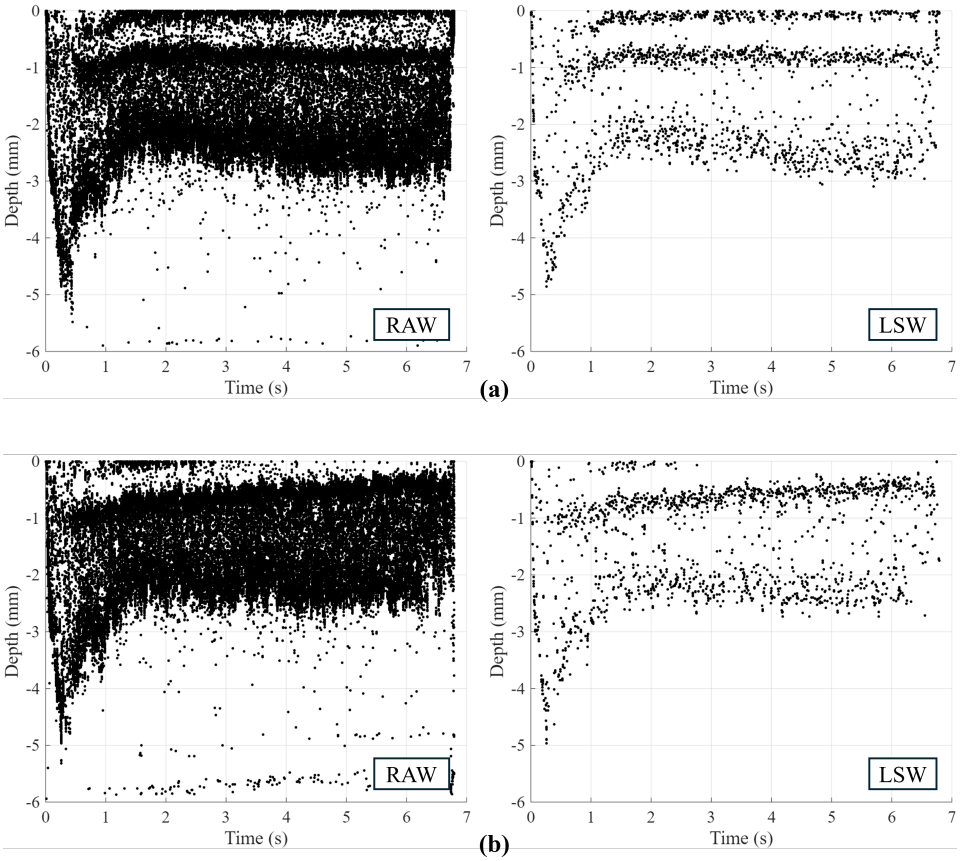


Fig. 5.6 Effect of local-support pre-processing on OCT depth point clouds (laser-only, 4 kW, v = 0.8 m/min). a: parallel scan. b: perpendicular scan.

Here percentile$(\cdot, P)$ denotes the order statistic corresponding to the $P$-th quantile, i.e. the value below which $P\,\%$ of the samples fall. In practice, the data inside $\mathscr{H}_i$ are sorted in ascending order and the element at rank $\lfloor P/100 \times |\mathscr{H}_i| \rfloor$ is returned.

In the present work, the parameters were set to $P = 91$ and $H = 61$, corresponding to a temporal support of $2H + 1 = 123$ samples. The choice of a high percentile ensures that the filter tracks the deeper part of the distribution, consistent with the negative–depth convention where the keyhole bottom corresponds to more negative values [108].

## Features extraction

From the depth curve quantitative features that can describe the weld penetration behaviour were extracted. Let $z(t)$ denote the final depth curve, expressed as negative values with respect to the sheet surface, and let $\mathscr{Z} = \{z(t_i)\}_{i=1}^{N}$ be the set of valid samples after all filtering stages. The following features were extracted:

**Lower Percentile Depth ($z_{p05}$)**: The $p$-th percentile of the depth distribution, with $p = 5$, is used to characterize the typical depth reached among the deepest values. This metric is defined as

$$z_{p05} = \text{quantile}(\mathscr{Z}, 0.05), \tag{5.3}$$

which corresponds to the depth value below which 5% of the samples lie. This feature is more robust than the absolute minimum and provides a conservative estimate of the keyhole bottom.

**Top-Decile Mean Depth ($z_{top10}$)**: The mean value of the deepest 10% of samples is computed as:

$$z_{\text{top10}} = \frac{1}{K} \sum_{j=1}^{K} z_{(j)}, \tag{5.4}$$

where $z_{(j)}$ are the $K = \lfloor 0.1N \rfloor$ most negative values of $\mathscr{Z}$. This measure emphasizes the persistent deep tail of the distribution while reducing sensitivity to outliers.

**Median ($z_{med}$)**:

$$z_{\text{med}} = \begin{cases} z_{\left(\frac{N+1}{2}\right)}, & \text{if } N \text{ is odd,} \\ \dfrac{z_{(N/2)} + z_{(N/2+1)}}{2}, & \text{if } N \text{ is even.} \end{cases} \tag{5.5}$$

**Lower-Envelope Median ($z_{\text{env,med}}$)**: The lower envelope of the depth is also computed to capture the oscillatory behavior of the keyhole bottom. Given the envelope signal $z_{\text{env,lo}}(t)$, the descriptor is defined as:

$$z_{\text{env,med}} = \text{median}\big(z_{\text{env,lo}}(t)\big), \tag{5.6}$$

which represents a robust estimate of the lower boundary of the depth oscillations.

**Median absolute deviation ($z_{MAD}$)**: The median of the absolute deviations from the sample median is calculated as:

$$z_{\text{env,med}} = \text{median}\big(z_{\text{env,lo}}(t)\big), \tag{5.7}$$

**Mean ($z_{mean}$)**: The mean is calculated as:

$$z_{\text{mean}} = \frac{1}{N}\sum_{i=1}^{N} z(t_i) \tag{5.8}$$

An additional subscript, x or y, is appended to each feature to indicate the scan direction (see Fig. 5.3).

## 5.6 Results and Discussion

### 5.6.1 Stage 1: Laser power variation

In this stage, bead-on-plate welds were produced using the laser only on 15-mm-thick S355 steel to compare OCT responses across laser powers from 1 to 12 kW at a travel speed of 0.8 m/min. The corresponding macrographs are shown in Figure 5.7. The weld depth is measured from the macro and compared to the measured depth from OCT sensor.

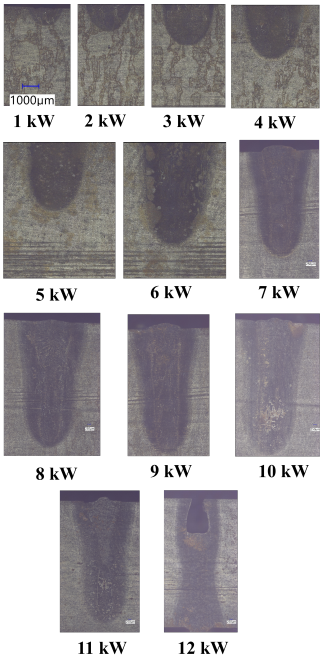


Fig. 5.7 Macro of bead-on-plate laser welds with laser power ranging from 1 to 12 kW at a travel speed of 0.8 m/min.

Figure 5.8 shows a comparison of the calcuated weld depth from oct signal of both scanning direction (parallel-x and perpendicular-y) compared to the measured from the macro section for the features: $z_{p05}$, $z_{top10}$, $z_{med}$, $z_{mean}$.

Across all statistics, the OCT-derived depth features reproduce the expected monotonic increase in penetration with laser power and therefore capture the global trend observed in the macro reference. The median $z_{med}$ shows the closest overall agreement with the macro depth across the full power range, with small and relatively constant bias and limited spread between scan directions. The mean $z_{mean}$ also follows the macro trend but exhibits a larger systematic underestimation—most evident at higher powers—and a wider separation between x- and y-scan results. The top-decile mean $z_{top10}$ tracks the macro reasonably well in the mid-power regime; however, it provides little advantage over the median and tends to increasingly underestimate depth as power rises. The lower-percentile depth $z_{p05}$ is the least consistent in absolute terms: while it mirrors the general increase with power, it displays large variability and occasional extreme values, particularly in the y-scan at low–mid powers. Regarding scan orientation, the x-scan curves are smoother and

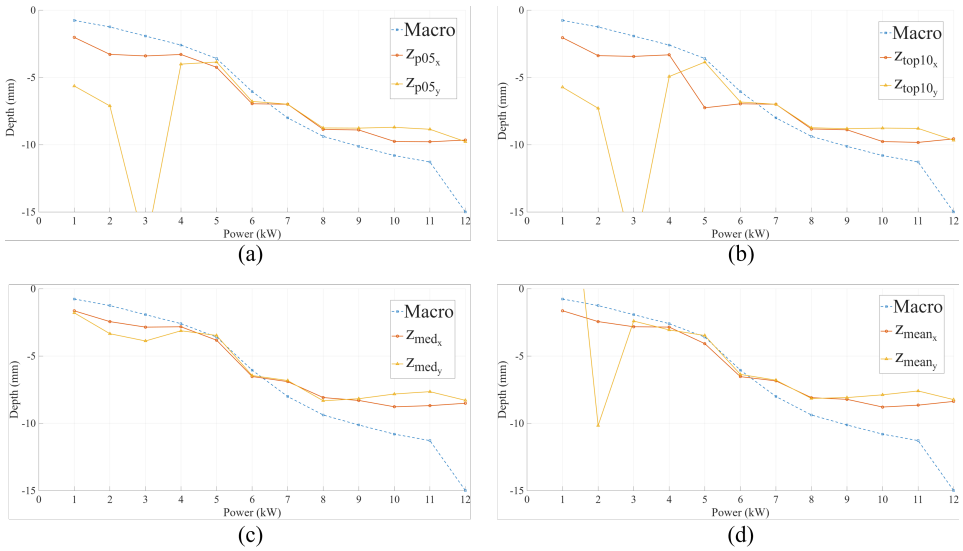


Fig. 5.8 Comparison between effective weld depth and features extracted from OCT signal for both scanning direction (x-parallel, y-perpendicular): a) Lower Percentile Depth $z_{p05}$; b) Top-Decile Mean Depth $z_{top10}$; c) Median $z_{med}$ d) Mean $z_{mean}$

.

more tightly clustered around the macro reference, whereas the y-scan retains the same global trend but with larger point-to-point scatter.

It is possible to observe pronounced deviations for $z_{p05}$, $z_{top10}$, and $z_{mean}$ in the y-scan between 2-4 kW, where unrealistically large negative depths appear. These excursions are caused by a small fraction of spuriously deep samples that persist after outlier removal. Under low-power, marginal-penetration conditions the keyhole is highly unstable; specular side-wall reflections, multiple internal reflections, plume attenuation, and brief misalignment of the transverse scan line with the keyhole axis lengthen the optical path and generate artefactual depths.

For $z_{p05}$, when such artefacts cluster to $\geq 5$ % of samples within a scan, the 5th percentile is dragged sharply downward, producing depths that exceed the physical plate thickness. For $z_{top10}$, the effect is even more direct: because it averages the deepest 10 % of samples, any concentration of these spurious returns dominates the statistic and yields very negative values. The $z_{mean}$ is also biased by the same asymmetric lower tail; although less extreme than the percentile-based metrics, the mean is pulled downward whenever the distribution contains even a modest number of these deep artefacts. Consequently, $z_{p05}$ and $z_{top10}$ are not reliable estimators

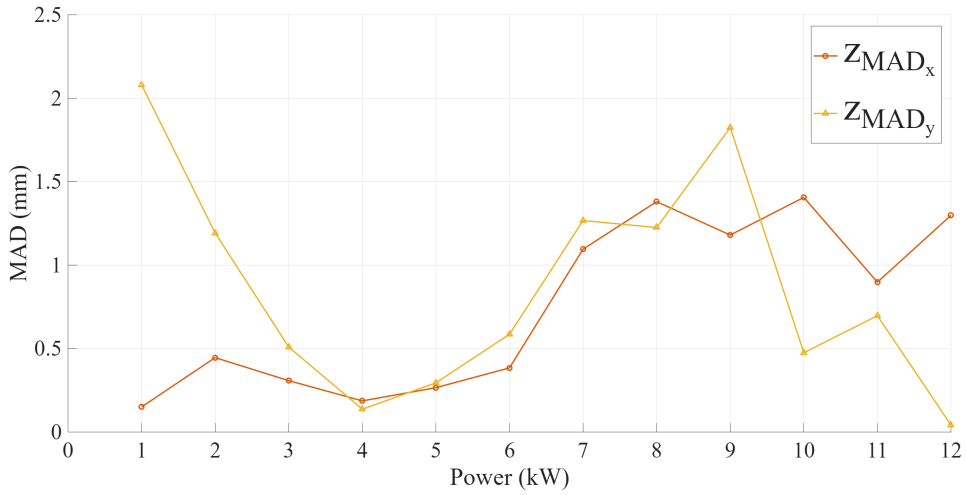


Fig. 5.9 Median absolute deviation (MAD) of the OCT depth signal for both scanning directions(x-parallel and y-perpendicular) across laser power levels.

of effective depth in the presence of keyhole/plume transients, and $z_{mean}$ exhibits a non-negligible negative bias in this regime.

The difference between scan directions is attributable to sampling geometry and process dynamics. In the x-scan, the beam repeatedly interrogates a line roughly aligned with the keyhole axis and therefore has a higher probability of intersecting the deepest region each cycle; temporal averaging along this path also mitigates oscillatory behaviour of the cavity. In the y-scan, the transverse pass samples different lateral sections of the pool; small lateral misalignments, bead wander, or oscillation phase lead to larger frame-to-frame variability and a greater propensity for percentile-based features to latch onto transient extremes. At higher powers, as penetration stabilizes, the discrepancy between x and y diminishes.

Agreement between OCT features and the macro reference is satisfactory up to approximately 6 kW. Beyond this point, all OCT curves plateau while the macro depth continues to increase, producing a systematic divergence. This behaviour reflects a measurement ceiling of the OCT setup: as penetration deepens, the useful axial range and signal-to-noise ratio are exceeded due to spectrometer bandwidth/spacing limits and strong attenuation/scattering inside the vapor–melt cavity. This is in accordance with previous findings which do not report measured depth greater than $\sim 6$ mm.

Figure 5.9 reports the median absolute deviation (MAD) of the OCT-derived depth versus laser power for the two scan orientations.

In the x-parallel scan ($x$-scan), MAD remains low ($\sim$ 0–0.5 mm) up to 6 kW, then exhibits a step increase to about 1 mm for $P \geq 7$ kW. This jump is consistent with the OCT range limit identified in Fig. 1.8: once penetration exceeds $\sim$6 mm, the lower portion of the keyhole lies outside the usable axial window, so depth samples become truncated/intermittently lost, broadening the sample distribution and elevating MAD.

In the y-transverse scan ($y$-scan), MAD is already large at low powers (1-3 kW). This reflects marginal keyhole formation with the 1.2 mm spot: in this power range the power density is not adequate for a stable keyhole formation . A transverse pass is therefore more likely to alternate between sampling the cavity and adjacent melt/solid regions within a cycle, producing large amplitude swings in the depth signal. The $x$-scan, by contrast, interrogates approximately along the seam centerline and is less sensitive to such lateral oscillations, hence the lower MAD in the same power range.

### DBSCAN and LSW Algorithm comparison

To compare the effectiveness of the pre-processing of raw OCT samples, Table 5.3 reports the average depth error (using the median feature) and the mean processing time for the two methods—DBSCAN and the Local Sliding-Window maximum (LSW)—considering only valid runs ($P_L = 3$–$6$ kW).

Table 5.3 Average error (with median) and average processing Time for different pre-processing methods for runs with $P_L = 3 - 6\ kW$

| | **DBscan** | | **LSW** | |
|---|---|---|---|---|
| **Scan direction** | Parallel | Perpendicular | Parallel | Perpendicular |
| **Average Processing Time (ms)** | 120,21 | 454,32 | 62,53 | 45,07 |
| **Average error (%)** | 6,68 | 7,87 | 5,63 | 9,34 |

Overall, LSW achieves substantially lower latency while preserving accuracy in the x-parallel scan and incurring a modest penalty in the y-perpendicular scan:

- **x-scan (parallel):** processing time decreases from 120.21 ms (DBSCAN) to 62.53 ms (LSW), a 48% reduction, with a simultaneous 15.7% relative improvement in error (6.68% $\rightarrow$ 5.63%).
- **y-scan (perpendicular):** processing time drops from 454.32 ms to 45.07 ms (approximately 90% reduction). Accuracy degrades from 7.87% to 9.34%

(+1.47 percentage points), indicating higher sensitivity of LSW to the larger lateral oscillations and intermittent keyhole formation typical of the transverse pass.

These results suggest that a simple sliding-window maximum is an attractive choice for *on-line* monitoring, where computational budget is critical: it reduces per-frame time by roughly one half in the x-scan and by an order of magnitude in the y-scan, while keeping errors within the 5–10% band reported as acceptable for OCT-based depth estimation in prior work ([108, 109]). The very large DBSCAN time in the y-scan is consistent with its parameter- and density-dependent complexity in the presence of many small clusters/noisy points.

In future work, the LSW approach should be evaluated under different optical configurations (smaller spots, alternative scan paths) to test generality and to determine whether its accuracy in the y-scan can be improved without sacrificing the latency benefit.

Overall, the x-parallel scan provides smoother trajectories and closer agreement with the macro reference than the y-transverse scan across the explored powers (Fig. 1.8). Among the tested statistics, the median depth $z_{\text{med}}$ is the most reliable estimator, while $z_{p05}$ and $z_{top10}$ are overly sensitive to transient artefacts and $z_{\text{mean}}$ shows a downward bias in the 2–4 kW range, especially in the y-scan. The dispersion metric corroborates this picture: MAD remains low ($\lesssim 0.5$ mm) up to 6 kW in the x-scan, is already large at 1–3 kW in the y-scan due to marginal/unstable keyhole formation, and rises again beyond 6 kW for both scans (Fig. 5.9). The growing mismatch above $\sim$6 kW reflects the OCT axial-range/SNR limit rather than a change in welding physics. Regarding pre-processing, the Local Sliding-Window maximum (LSW) achieves substantially shorter processing times than DBSCAN while preserving accuracy in the x-scan and incurring only a modest penalty in the y-scan, making it the preferable choice for on-line use (Table 5.3).

### 5.6.2 Stage 2: Laser-Arc Distance Variation

Having established the data-processing workflow, the sensor performance was evaluated in a Hybrid Laser–Arc Welding (HLAW) configuration. Bead-on-plate welds were produced in two torch arrangements laser-leading and arc-leading with a laser–torch separation $D_{LT} = 6,\ 11,$ and 16 mm, for a total of six tests. The process

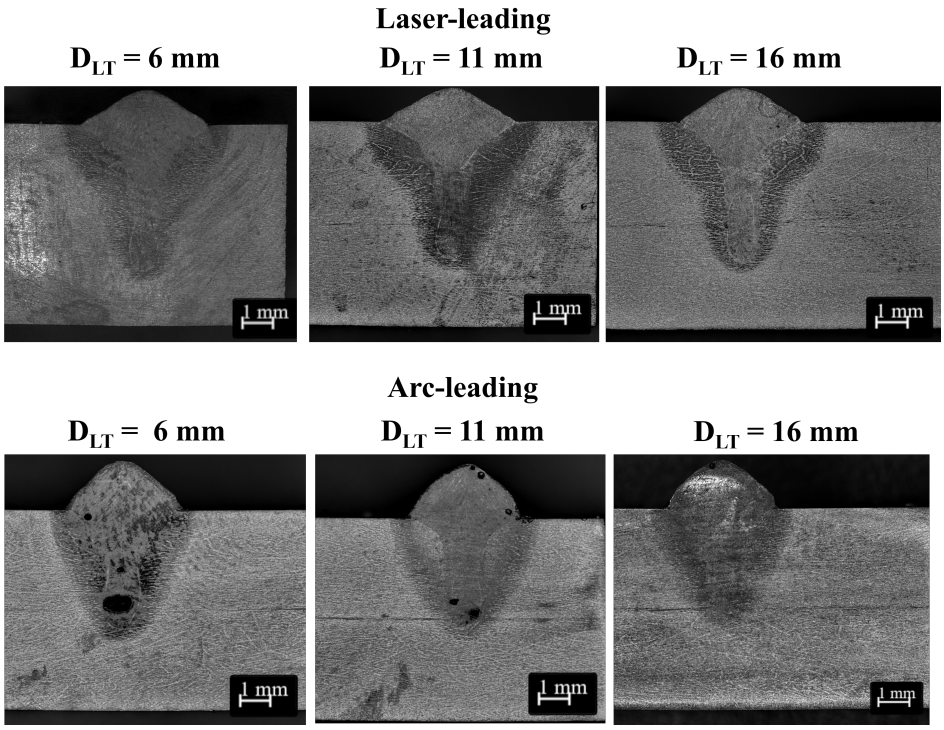


Fig. 5.10 Cross-section for bead-on-plate weldings with laser-leading and arc-leading

was monitored using the same OCT strategy as in Stage1, but the line scan was now applied only in the $x$-direction (parallel to the welding direction). The corresponding macrographs of the cross-sections are reported in Fig.5.10. This stage investigates how the leading sequence and the separation $D_{LT}$ affect the OCT-derived depth estimates and their agreement with metallographic measurements.

At fixed laser power (6 kW), the measurements exhibit a consistent dependence on the laser–torch separation $D_{LT}$: with increasing $D_{LT}$ the bead reinforcement (A) increases, whereas penetration (B) decreases, for both leading arrangements. This behaviour is characteristic of a progressive weakening of laser–arc coupling. As the heat sources are separated, the interaction between the laser-induced and arc plasmas diminishes and the process approaches “tandem-like” operation; energy is redistributed toward the upper weld pool, so that the arc increasingly governs surface melting and droplet deposition while the laser contributes less to keyhole stability and depth formation. Established studies on steels report that reducing the distance between the heat sources strengthens coupling and increases penetration, whereas excessive separation broadens the cap at the expense of depth, consistent with the present trend [112].

Table 5.4 Results for Laser- and Arc-leading configurations at three values of Laser-Torch Distance ($D_{LT}$).

| | | $D_{LT}$ | | |
|---|---|---|---|---|
| **Configuration** | **Measurement** | **6** | **11** | **16** |
| **Laser leading** | $h_{macro}$ | 1,337 | 1,394 | 1,340 |
| | $z_{macro}$ | 5,852 | 5,448 | 5,340 |
| **Arc leading** | $h_{macro}$ | 2,395 | 2,576 | 2,651 |
| | $z_{macro}$ | 5,768 | 5,402 | 4,697 |

Configuration effects observed here—systematically deeper welds for laser-leading at a given $D_{LT}$ and higher reinforcement for arc-leading—are consistent with the distinct roles of the two heat sources in steels: the laser, by virtue of its focused power density and keyhole mode, chiefly governs penetration, whereas the arc, as a more diffuse source with filler transfer and momentum, predominantly sets bead build and width. Consequently, when the laser precedes the arc, the keyhole is formed and stabilised ahead of arc heating, favouring depth; when the arc leads, preheating and metal transfer promote surface reinforcement but reduce laser effectiveness at the root. Studies on steel HLAW recognise that arc position (laser-leading versus arc-leading) modulates root stability and depth distribution in line with these mechanisms [113, 114].

Figure 5.11 compares the macro-derived depth ($z_{macro}$) with the OCT median feature ($z_{med}$) obtained with the $x$-scan at fixed laser power ($P_L = 6\,\text{kW}$) and three laser–arc separations $D_{LT} = \{6, 11, 16\}\,\text{mm}$.

In the *laser-leading* arrangement (Fig. 5.11a) the two curves are almost coincident across $D_{LT}$, yielding an average error of 0.98% and a maximum error of 1.11% at $D_{LT} = 16\,\text{mm}$. In the *arc-leading* case (Fig. 5.11b) the OCT median reproduces the same monotonic dependence on $D_{LT}$ but exhibits a systematic shallow bias with respect to the macro, more pronounced around $D_{LT} = 11\,\text{mm}$.

To investigate the reduced accuracy observed in the arc-leading configuration, the videos recorded by the Cavitar camera during welding were examined. Figure

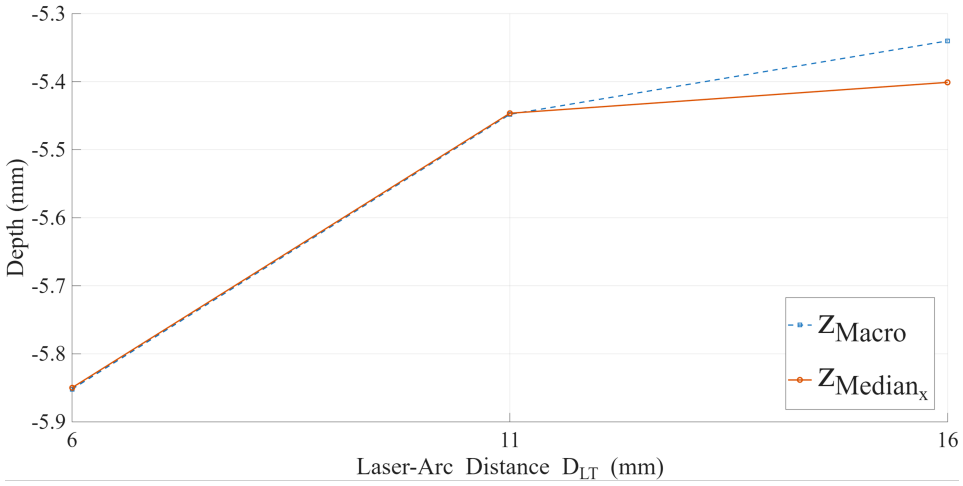


**(a)**

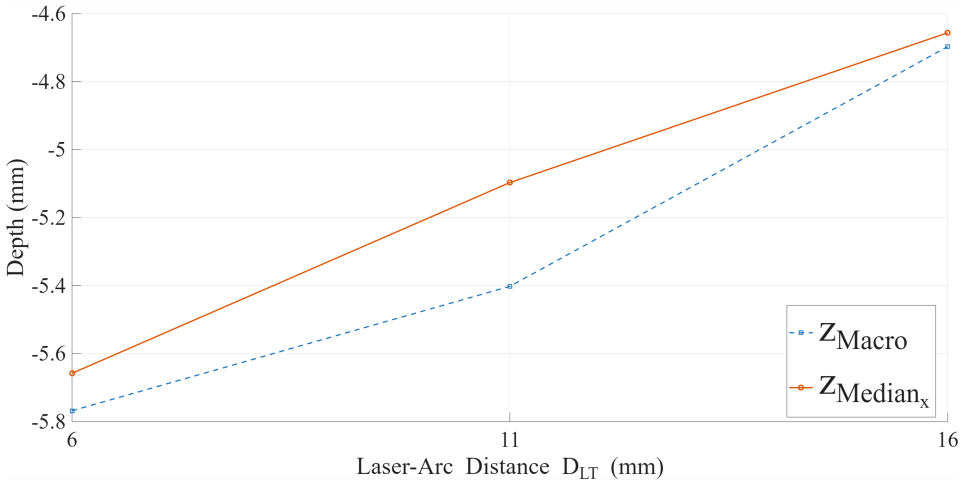


**(b)**

Fig. 5.11 Comparison between effective weld depth and median extracted from OCT signal for x-parallel scanning direction: a) Laser-leading configuration; b) Arc-leading configuration.

5.12 shows four representative phases during HLAW in bead-on-plate mode with arc-leading at $P_L = 6\,\text{kW}$ and $D_{LT} = 6\,\text{mm}$.

**Phase I:** initial ignition of the laser beam with the arc still off. The motion system remains idle for a short interval, producing locally deep penetration. **Phase II:** the travel motion starts and the electric arc ignites. **Phase III:** the process reaches a quasi-steady operating condition. **Phase IV:** the arc is extinguished, while the laser continues for a brief time.

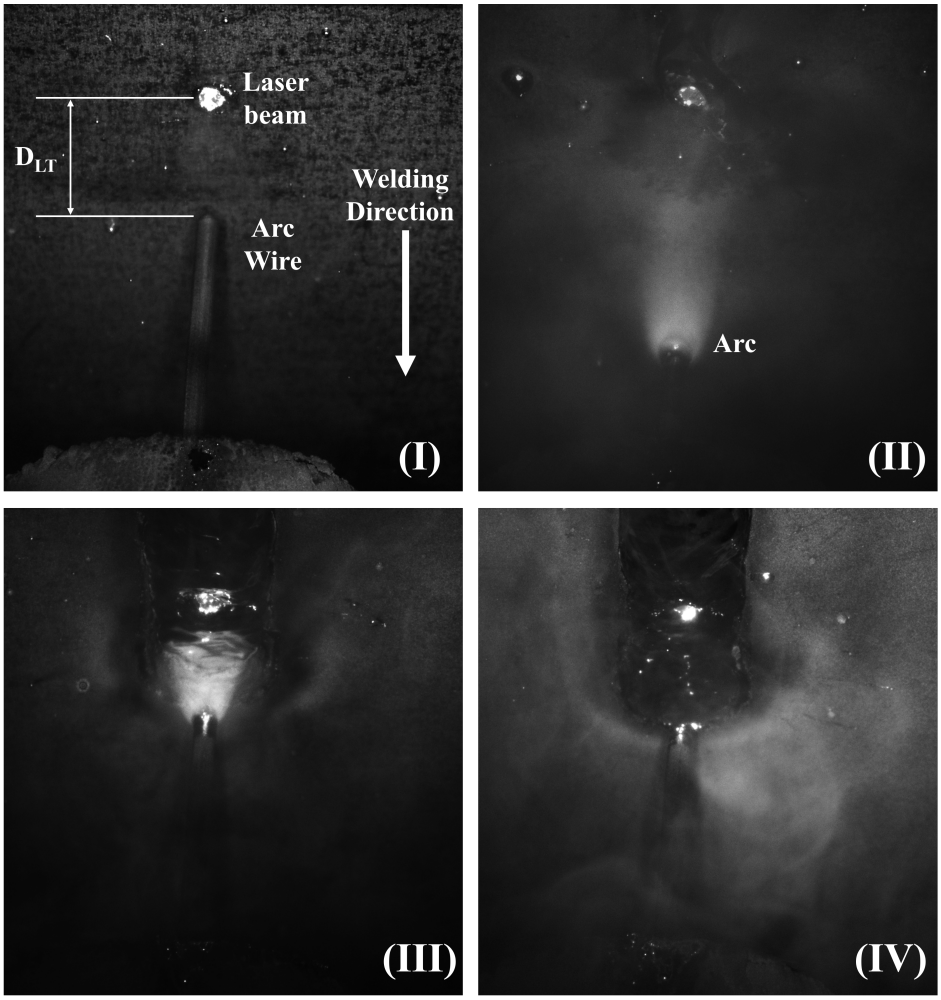


Fig. 5.12 Different phases during HLAW in bead-on-plate configuration with arc-leading, $P_L$ = 6 kW and $D_{LT} = 6mm$

The same phases identified in the Cavitar footage can be recognized in the OCT depth time series acquired with the $x$-scan. As shown in Fig. 5.13, the signal clearly reflects the sequence of events: after the initial laser idle (Phase I), the onset of

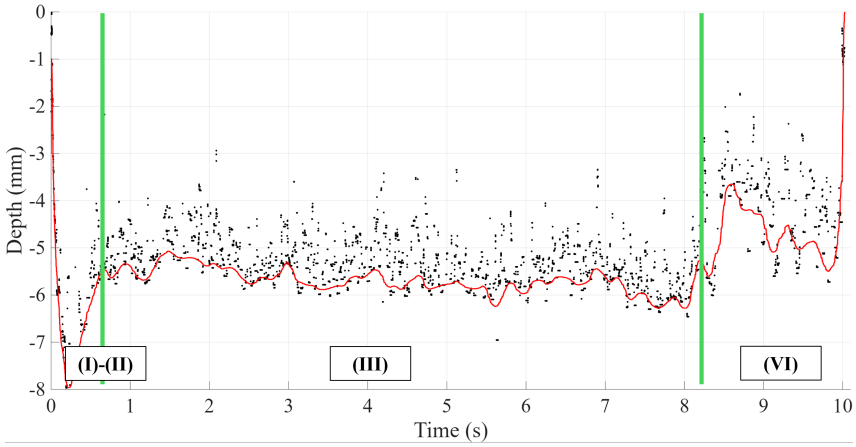


**(a)**

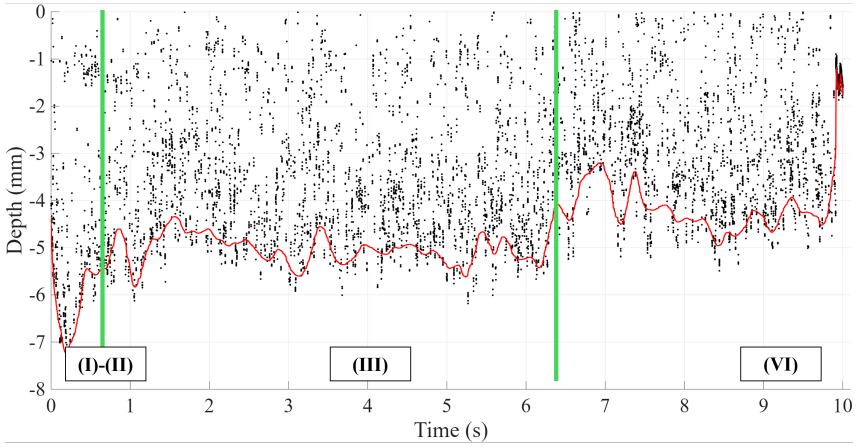


**(b)**

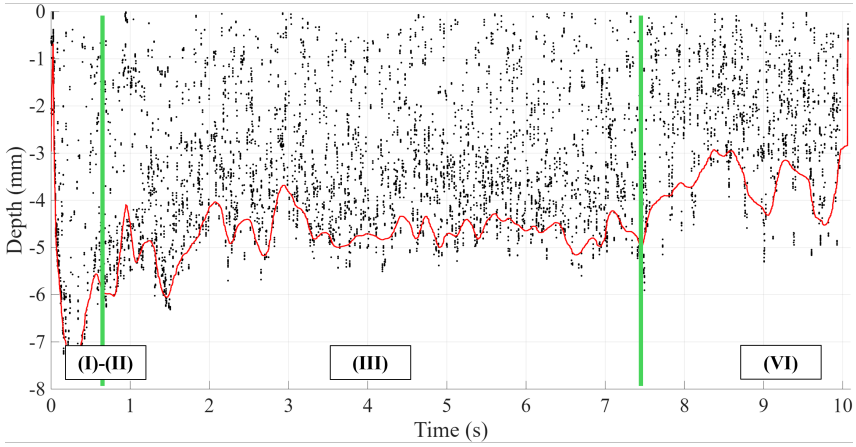


**(c)**

Fig. 5.13 OCT Signal (x-scan) acquired during HLAW in bead-on-plate configuration with arc-leading

travel and arc ignition (Phase II) produces a transition to a new operating level with increased short-time fluctuations; during steady operation (Phase III) the median depth remains approximately constant with bounded variability; finally, the extinction of the arc (Phase IV) is marked by a sudden drop of the estimated penetration toward the laser-only level. This behaviour is physically consistent with the removal of the arc's additional heat and pressure, which reduces energy coupling and narrows the keyhole, thereby decreasing the total penetration. Practically, these signatures enable in-line phase detection.

In the hybrid bead-on-plate trials, the $x$-scan OCT measurement reproduces the expected dependence on the laser–torch separation $D_{LT}$ observed in the macrographs (Fig. 5.10): as $D_{LT}$ increases at fixed $P_L = 6\,\mathrm{kW}$, reinforcement grows while penetration decreases. The laser-leading arrangement delivers the best agreement with metallography (Fig.5.11a), with sub-percent errors and no appreciable trend bias, confirming that the median feature remains a reliable estimator in this layout. In contrast, the arc-leading configuration follows the same monotonic trend but exhibits a shallow bias (Fig.5.11b), consistent with additional optical attenuation and surface disturbance introduced by the arc ahead of the laser. Analysis of Cavitar footage and the corresponding OCT time series (Figs.5.12–5.13) shows that the sensor distinctly captures start/ignition and arc-off transients, enabling in-line phase detection. Overall, with $x$-scan the OCT system is trend-accurate in both leading modes, quantitatively accurate in laser-leading, and requires configuration-dependent calibration or scan-path adjustment for arc-leading.

### 5.6.3 Stage 3: Butt-joining HLAW

In this final stage, three Hybrid Laser–Arc Welding (HLAW) tests were carried out on butt joints to challenge the OCT system under distinct penetration regimes and thus assess its validity across adverse conditions. All trials were executed in a laser-leading arrangement, with the OCT line scan applied in the $x$-direction (parallel to the welding direction).

The travel speed was kept constant at 0.8 m/min, and the arc parameters were held fixed throughout. The parameter sets were selected to purposely induce (run #1) partial penetration / lack of root fusion with $D_{LT} = 16\,\mathrm{mm}$ and $P_L = 4\,\mathrm{kW}$; (run #2) normal penetration with $D_{LT} = 16\,\mathrm{mm}$ and $P_L = 6\,\mathrm{kW}$; and (run #3) excessive

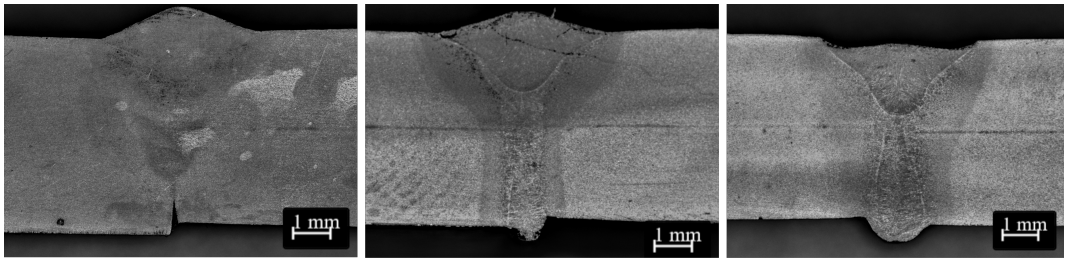


$D_{LT}$ = 16 mm - $P_L$ = 4 kW Run #1 | $D_{LT}$ = 16 mm - $P_L$ = 6 kW Run #2 | $D_{LT}$ = 6 mm - $P_L$ = 6 kW Run #3

Fig. 5.14 Cross-section of butt HLAW in laser-leading configuration

penetration—including root sagging and marginal incisions—with $D_{LT} = 6\,\text{mm}$ and $P_L = 6\,\text{kW}$. The resulting cross-sections are shown in Fig. 5.14. It is emphasised that these joints were designed to span controlled under-, nominal-, and over-penetration conditions for sensor evaluation, not to optimise weld quality.

Figure 5.15 compares the macro-derived depth with the OCT median ($x$-scan) for the three butt-joint runs. The average percentage error (APE) for Runs 1–3 is $[2.98\%, 2.07\%, 15.32\%]$, respectively. Thus, Runs 1 and 2 show good quantitative agreement, whereas Run 3 exhibits a marked underestimation by the OCT feature.

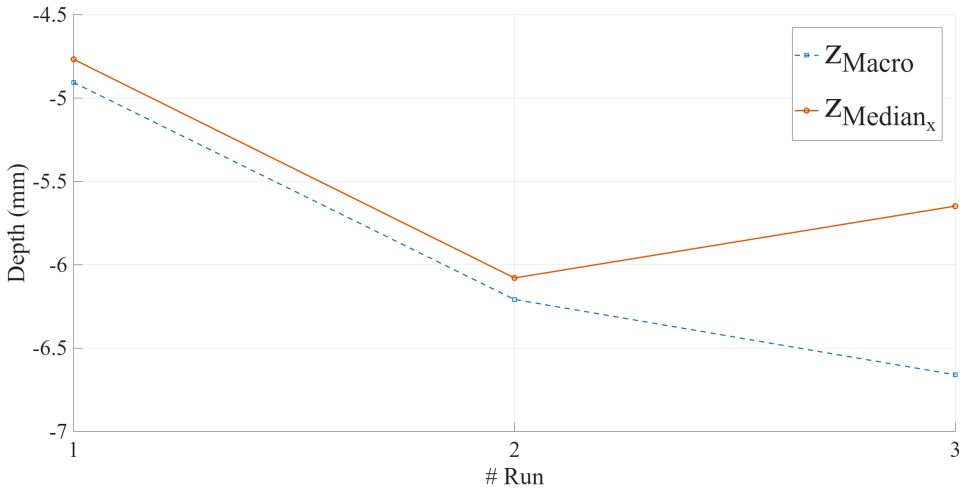


Fig. 5.15 Comparison between macro measuremetns and median feature from OCT sensor for butt-joining HLAW for the three runs

The poor result in Run3 is associated with the occurrence of humping during the first part of the weld and with a progressive opening of the butt-joint gap as welding proceeds.

In laser–arc hybrid welding, *humping* denotes a regular and approximately periodic sequence of local swellings (wave peaks) and depressions (wave troughs) of weld metal along the welding direction. Depending on thickness and process conditions, humping can manifest on the top surface (typically emphasized in thin-plate/high-speed regimes) or at the weld root (more common in medium- to thick-plate and deep-penetration regimes), where it is often observed as a series of solidified drops or bulges along the root line. From a mechanistic standpoint, the literature attributes root humping to melt-flow and force-balance instabilities at the bottom of the molten pool: liquid metal driven toward the root cannot be reabsorbed efficiently before the trailing region solidifies, so it accumulates and freezes into periodically spaced humps. This behaviour is consistently described in terms of (i) an imbalance between gravity and surface tension at the weld root, (ii) molten-metal flow rates at the bottom of the pool that exceed the travel speed, and (iii) process conditions that promote over-penetration and unstable melt redistribution. In hybrid welding, the interaction between the laser and arc heat sources is an additional controlling factor; accordingly, the laser–arc distance is reported as an influential parameter for root-humping formation. In the present study, humping was observed for the short laser–arc separation ($D_{LT} = 6\,\mathrm{mm}$), whereas it was not observed for the larger separation ($D_{LT} = 16\,\mathrm{mm}$), highlighting the strong sensitivity of this instability to the heat-source interaction in the employed parameter window [115, 116].

To further investigate the impact of humping on the OCT depth signal, the MAD feature was evaluated by computing it separately over the interval where humping is present and over the subsequent interval where humping disappears as the inter-plate gap increases.

As documented in Fig. 5.16, the weld alternates between segments with pronounced humping and segments where the bead becomes smooth as the inter-plate gap opens. The suppression of root humping by introducing a controlled butt gap is consistent with prior observations: an air gap can facilitate energy delivery toward the root and enlarge the effective molten region behind the keyhole, thereby increasing the likelihood that molten metal at the root is reabsorbed before it organizes into solidified drops [115, 116]. In the present experiment, once the gap becomes clearly visible in the camera frames (right-hand side of Fig. 5.16), the root morphology transitions to a smoother, more stable appearance and the humping pattern vanishes.

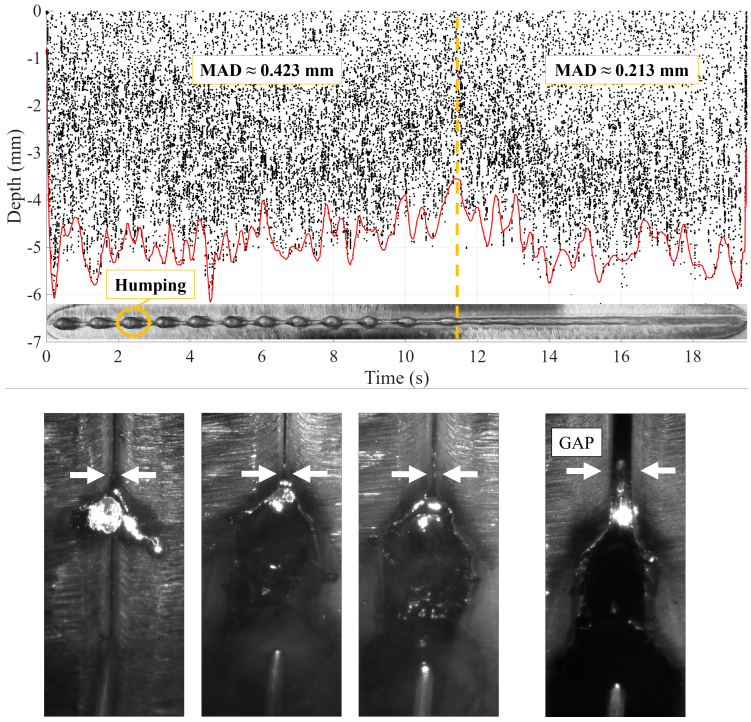


Fig. 5.16 OCT signal and camera screenshots during welding under a progressive gap increase, highlighting humping formation and mitigation

These morphological changes leave a clear signature in the OCT depth time series. Because humping is, by definition, a periodic swelling–collapse pattern along the welding direction, the tracked depth exhibits larger point-to-point variability during humping-affected intervals, producing a broader distribution of depth samples around the central tendency. This is captured quantitatively by the median absolute deviation: in Fig. 5.16, the humping segment shows a markedly larger dispersion (MAD $\approx 0.423$ mm) than the later, smooth-bead segment (MAD $\approx 0.213$ mm). Practically, these observations support using MAD as a stability indicator for OCT-based monitoring in butt HLAW: high MAD marks intervals associated with humping-affected bead formation, whereas low MAD corresponds to comparatively stable weld formation under an opened-gap condition.

This last result, however, requires further validation under additional process conditions that generate humping, together with a broader analysis of OCT signals, to confirm whether a quantitative dispersion metric (e.g. MAD) can reliably diagnose the occurrence of humping. This aspect was not addressed in the present work due to time and resource constraints.

## 5.7 Conclusion

This chapter set out to evaluate the feasibility and limits of Optical Coherence Tomography (OCT) for *in-line* monitoring of Hybrid Laser–Arc Welding (HLAW). The central question was whether a line-scan OCT configuration, coupled with a robust yet lightweight processing workflow, can deliver reliable weld-depth estimates across relevant process layouts, and under which conditions those estimates remain valid.

The study first established the behaviour of OCT on laser-only bead-on-plate trials. Using the same signal chain throughout, the *median* depth $z_{\mathrm{med}}$ emerged as the most reliable statistic, while lower-tail and top-tail metrics ($z_{p05}$ and $z_{\mathrm{top10}}$) proved overly sensitive to transient artefacts and $z_{\mathrm{mean}}$ showed a shallow bias at 2–4 kW. The $x$-parallel scan consistently produced smoother, macro-consistent trajectories compared with the $y$-transverse scan. A practical ceiling was identified: beyond $\sim$6 kW, OCT depths plateau whereas macro depths continue to rise, revealing an axial-range/SNR limitation of the present setup. The dispersion metric corroborated these trends: MAD remained $\lesssim 0.5$ mm in stable regimes and increased when the process became unstable or the range limit was approached.

To make the approach suitable for on-line use, two pre-processing strategies were compared. The proposed Local Sliding-Window maximum reduced latency substantially while retaining accuracy: in $x$-scan the mean processing time fell from 120.21 ms (DBSCAN) to 62.53 ms (LSW) with a simultaneous reduction in error (from 6.68% to 5.63%), and in $y$-scan time dropped from 454.32 ms to 45.07 ms with only a modest loss of accuracy. This balance of speed and fidelity motivates LSW as the default choice for embedded, real-time implementations.

The methodology was then exercised on hybrid bead-on-plate welds, scanned in the $x$-direction only. At fixed $P_L = 6$ kW, both macrographs and OCT captured the expected dependence on the laser–torch separation $D_{LT}$: reinforcement increased and penetration decreased as $D_{LT}$ grew, indicating weaker laser–arc coupling. Agreement was quantitatively strong in the laser-leading layout (average error $\approx 1\%$; maximum $\approx 1.1\%$ at $D_{LT} = 16$ mm), whereas a shallow bias appeared in arc-leading, plausibly due to arc-induced optical attenuation and surface disturbance upstream of the laser. Importantly, the OCT time series reproduced start/ignition and arc-off transients

visible in camera footage, showing that the sensor can also provide phase information without high-speed imaging.

Finally, butt-joint trials were designed to span partial, nominal, and excessive penetration. Average percentage errors were 2.98%, 2.07%, and 15.32% for the three runs, with the degradation in the third case linked to humping and progressive gap opening. These conditions caused truncated or off-axis A-lines and widened the depth distribution, biasing $z_{\mathrm{med}}$ shallow and pushing the system toward its axial-range limit. The MAD rose conspicuously during humping and returned toward baseline once the gap stabilised full penetration, supporting its use as a stability flag and a basis for segment-wise data gating.

Taken together, the results indicate that OCT can provide trend-accurate—and, in favourable configurations, quantitatively accurate—depth monitoring in HLAW. The most robust operating envelope combines $x$-scan, laser-leading, moderate $D_{LT}$, and median-based estimation with MAD-based quality checks. Within this envelope the method offers a practical blueprint for industrial integration: a computationally light pre-processing step (LSW), a robust central statistic (median), and a simple dispersion metric (MAD) for in-line stability assessment.

Several caveats frame these conclusions. The experiments were performed on S355 steel at a single travel speed with a specific optical setup, and the axial-range limit curtailed validation above $\sim$6 mm effective thickness. These constraints suggest clear directions for future work: extend the axial range through sensor/optics upgrades and test thicker sections; develop adaptive scan-path strategies to maintain alignment with the keyhole bottom—especially in arc-leading; formalise MAD-based gating with minimum-duration criteria to exclude unstable segments and enable segment-wise calibration; validate across materials, speeds, and $D_{LT}$; fuse OCT with complementary process signals to improve robustness to plume occlusion; and implement the full pipeline on embedded hardware to support real-time supervisory or closed-loop adjustments when instability is detected.

# Chapter 6

# Case study 3 – Monitoring welding-induced distortion in laser welding using infrared thermography and thermo-mechanical modelling

## 6.1 Introduction

This chapter investigates the integration of infrared (IR) thermography with thermo-mechanical finite-element modelling (FEM) to predict component-scale distortions during laser welding. The following section establishes the industrial relevance of welding-induced distortion and reviews state-of-practice approaches for distortion prediction and inspection, thereby motivating the use of infrared thermography as a means to support in-process monitoring of weld-induced distortions.

Laser welding is a cornerstone of lightweight manufacturing and is widely used to join aluminium alloys in the automotive sector due to its precision and throughput. The push toward lighter, fuel-efficient vehicles has increased the use of thin aluminium sheets [117]. However, welding of such sheets is challenging due to their heat-input sensitivity: poor heat control promotes distortion and undermines quality [118]. Aluminium's high thermal expansion and low elastic modulus, relative to carbon steels, amplify deformation and residual stresses that compromise product quality [8]. For thin-sheet assemblies, even small out-of-plane warping can violate

dimensional tolerances, degrade fit-up, and cause misalignment during downstream joining or automated assembly [119]. Corrective actions (e.g., straightening or stress relief) add cost and complexity and are often constrained by the alloy temper and assembly state, meaning that residual stresses and geometric deviations cannot always be fully recovered once the part is welded [117]. Since the magnitude and spatial distribution of distortion are primarily governed by the transient thermal field generated during welding, monitoring the thermal history (i.e., thermal cycles and gradients) provides a direct route to assess distortion propensity.

In industrial practice, distortion is commonly assessed offline, after welding, through dimensional inspection or profiling. While suitable for process qualification and auditing, offline inspection does not provide information during the thermal transient that generates distortion; as a result, it does not directly support in-process decisions (e.g., parameter adaptation, fixture strategy, or acceptance decisions) when production throughput and part complexity increase [119]. Infrared thermography is therefore particularly relevant, as it enables non-contact, time-resolved measurement of weld-zone temperatures from which thermal cycles can be extracted during the process. In parallel, FEM-based prediction is routinely used to anticipate thermal fields and distortions and to support process development [120]. A persistent bottleneck is that reliable distortion prediction depends on how accurately the model is thermally constrained, including the representation of heat input and heat losses [121]. Conventional calibration typically relies on iterative tuning supported by destructive cross-sections and expert judgement, which limits scalability and repeatability when multiple part variants, fixtures, or process windows must be managed [122].

Recent advances aim to address these issues through non-destructive testing and model-based identification, including automated calibration [123], inverse modelling [124], and emerging digital-twin frameworks [125]. However, practical deployment is often hindered by workflow complexity and sensitivity to boundary-condition uncertainty, which is particularly critical for thin sheets where clamping and contact conditions strongly affect distortion.

In this context, this chapter presents a thermography-assisted calibration strategy for thermo-mechanical FEM, denoted infrared-guided imposed thermal cycle (IR-ITC). The IR camera measures the transient surface temperature evolution during welding; a thermal cycle extracted from the measured field is then imposed as a

direct thermal constraint in the simulation. This enables distortion prediction driven by in-process thermal information, reducing reliance on destructive sectioning and extensive heat-source parameter tuning while maintaining the ability to predict welding-induced deformation.

Part of the information contained in this chapter is extracted from the paper: "P. Russo Spena, M. De Maddis, V. Razza, L. Santoro, H. Mamarayimov, **D. Basile**, *Infrared-guided thermal cycles in FEM simulation of laser welding of thin aluminium alloy sheets*, 2025" (reference [126]).

## 6.2 Objective

This chapter addresses **RQ3:** *Can infrared thermography constrain thermo-mechanical simulations to enable in-process prediction of welding-induced distortions, while reducing reliance on destructive and iterative heat-source calibration?* To answer RQ3, the study pursues the following objectives:

- Develop an infrared-guided imposed thermal cycle (IR-ITC) procedure to transfer thermography-derived thermal histories into a thermo-mechanical FEM framework;
- Define an experimental protocol for acquiring thermographic thermal cycles under controlled fixturing and welding conditions suitable for model constraint;
- Validate the resulting distortion predictions against experimental distortion measurements on thin aluminium sheet welds;
- Assess the extent to which thermography-based constraints reduce reliance on destructive calibration and iterative heat-source parameter tuning relative to conventional moving heat source workflows.

## 6.3 Experimental program

The experimental program comprises three stages:

1. First, butt-joint laser welding trials were performed under controlled fixturing and process conditions. During welding, the transient surface temperature field was acquired by an infrared (IR) camera. From the recorded thermograms, representative thermal cycles were extracted from regions adjacent to the molten zone and used to define the imposed thermal loading for the infrared-guided imposed thermal cycle (IR-ITC) simulations.

2. Second, post-weld distortions were measured experimentally and compared with the distortions predicted by the thermography-constrained FEM simulations, providing the primary validation of the proposed workflow.

3. Third, additional validation was performed using a conventional moving heat source (MHS) simulation with the same mesh configuration and model settings. Fusion-zone cross-sections and thermal histories were extracted from the MHS model, and the MHS-derived thermal cycles were used as input for a traditional imposed thermal cycle (T-ITC) simulation. Cross-sectional geometry and thermal histories were compared across experiment, MHS/T-ITC, and IR-ITC to further substantiate the thermography-based thermal constraint and the resulting distortion predictions.

## 6.4 Experimental setup

The laser source was a diode laser (Laserline LDF 4000-40) with a maximum power of 4 kW, emitting at 1020 and 1060 $\pm$10 nm. The welding head (Laserline OTS-5) was mounted on a 6-axis ABB IRB 2400 robot. Trials were performed on 1.5 mm Al 6061-T6 plates of size $150 \times 200$ mm in a butt configuration. Prior to welding, the joint region was abraded and polished to remove contaminants and then cleaned with acetone. The two plates were clamped to achieve a zero-gap fit-up, as shown in Figure 6.1. The beam was oriented normal to the surface, with the focal position set 3 mm above the plate, producing a 1.2 mm spot. No shielding gas or filler was used. The laser power was set to 2800 W. The two welding experiments differed only in travel speed: 35 and 50 $\mathrm{mm\,s^{-1}}$ for Sample 1 and Sample 2, respectively. Process parameters were selected from preliminary trials to generate appreciable distortion, thereby providing a demanding test case for model-based prediction.

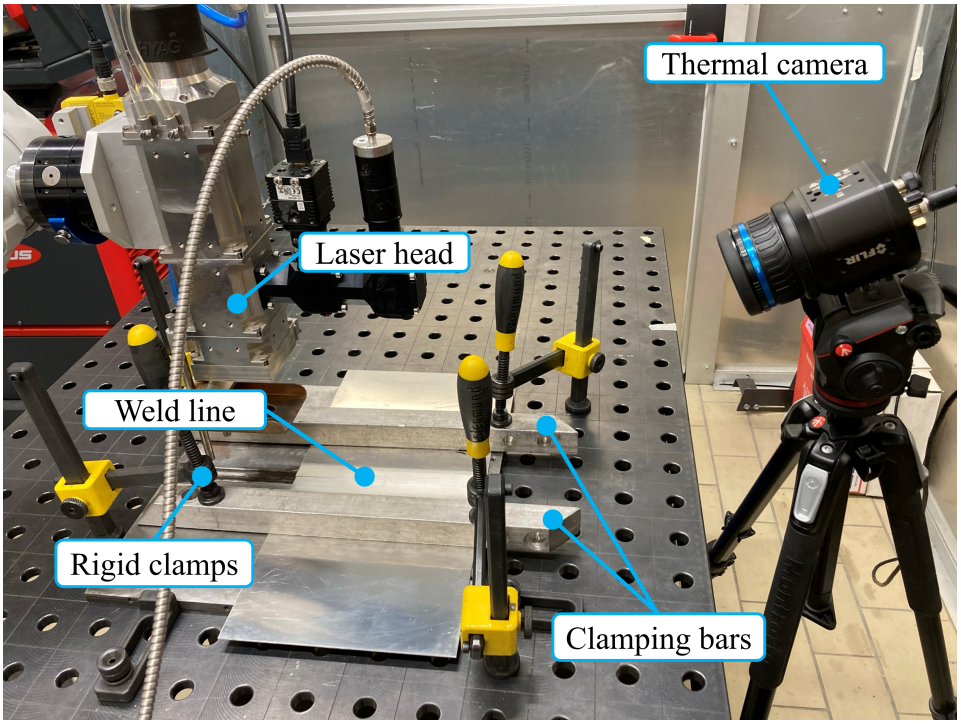


Fig. 6.1 Welding setup and thermal camera.

To characterize joint geometry and support model validation, cross-sections were obtained from the weld seam. Specimens were hot-mounted, polished, and etched with Keller's reagent for metallography. Images were acquired with an optical microscope (ZEISS Axiovert a1) and weld geometry was measured in ImageJ. Two reference measurements were considered: the maximum width near the mid-thickness of the cross-section ($w_1$) and the width at the bottom of the fusion zone ($w_2$), as shown in Figure 6.2(a). Post-weld distortion was quantified using a contact profilometer by measuring the distortion angle. One side of the sheet was fixed (Figure 6.2(b)), and the measurement path was oriented 90° to the seam at the sheet midpoint. The metric considered was the angular distortion $\alpha$. Symmetry of the angular distortion on the two sides of the joint was assumed.

### 6.4.1 Thermal-cycle monitoring by infrared thermography

The laser welding process was monitored using a FLIR A700 microbolometric infrared camera equipped with an FOL18H lens. The system employed a long-wave infrared (LWIR) sensor (7–14 µm), which is suitable for laser welding at $\sim 1\,\mu m$

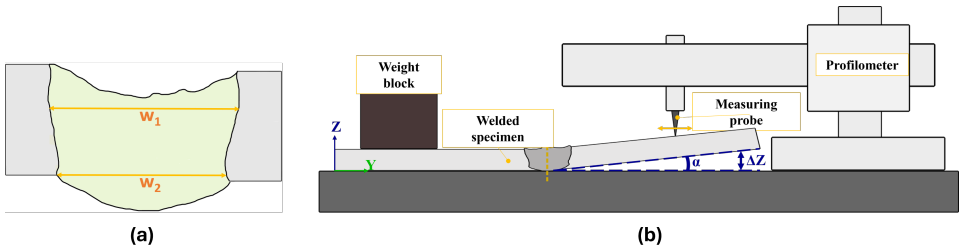


Fig. 6.2 Experimental measurements for (a) weld geometry; (b) distortion angle.

because the measurement band is spectrally separated from the laser emission. The camera was positioned at an oblique viewing angle of 40° with respect to the horizontal to maintain line-of-sight to the weld zone while minimizing occlusions from the fixture. The camera was mounted on a rigid stand and the acquisition geometry was kept constant across experiments to ensure comparable spatial sampling; the resulting IFOV was 676 mrad. The measurement range was set to 0–700 °C to capture the weld-zone thermal transient without changing calibration settings between runs. Thermograms were post-processed in FLIR Research Studio.

IR temperature retrieval depends on the assumed surface emissivity, which varies with temperature, surface condition, and oxidation. In this study, emissivity was set by identifying an isothermal plateau around the solid–liquid transition (approximately 650–670 °C) and cross-checking literature values for aluminium 6061/6082 [127]. The emissivity was set to 0.35. As the apparent temperature within the molten pool is additionally affected by emissivity changes and occasional pixel saturation, thermal-cycle extraction was performed in a region immediately outside the molten zone, where emissivity is comparatively more stable and the sensor response remains within range. The extraction location and ROI size were defined through preliminary trials to balance measurement robustness (avoiding saturation and strong emissivity transients) with spatial averaging to improve repeatability. Specifically, thermograms were inspected to locate the pool boundary and a consistent reference region adjacent to it; the thermal cycle was obtained as the mean radiometric temperature within this fixed ROI over time. The resulting thermal history was then used as the imposed thermal input for the IR-ITC model.

## 6.5 Numerical model

To evaluate how the thermal history drives mechanical distortion, thermo-mechanical models were solved with a two-stage FEM workflow: a thermo-metallurgical (thermal) step followed by a mechanical step [128]. The same mesh was used for both samples, varying only input parameters. Simulations were executed in SYSWELD. Material properties and model settings were selected from the SYSWELD database. The convective coefficient was set to $h_c = 25\ \mathrm{W\,m^{-2}\,K^{-1}}$, and the surface emissivity to $\varepsilon = 0.8$ (simulation-side radiative boundary condition).

Using Visual-Mesh (SYSWELD), the discretization comprised 54,400 8-node hexahedral linear 3D prism elements for the solid, 36,544 4-node linear 2D surface elements for environmental heat exchange, and 200 1D line elements defining the welding path and reference lines.

Figure 6.3 illustrates the model layout, clamp positions, and the Heat Affected Zone (HAZ) mesh. The axes are defined so that $x$ follows the travel direction, $y$ spans the width, and $z$ is through thickness (pool penetration). Mesh density was increased in thermally critical regions to balance accuracy and runtime: the HAZ used $0.25 \times 0.25 \times 1.0$ mm cells, transitioning to coarser center-concentric biased elements beyond the Fusion Zone (FZ). The Broyden–Fletcher–Goldfarb–Shanno (BFGS) algorithm ensured numerical stability and convergence [125].

Under identical welding conditions, thin plates exhibit pronounced longitudinal and transverse shrinkage and angular distortion due to thermal expansion/contraction [129]. Small-deformation formulations—where strain depends linearly on displacement—tend to underpredict such effects and cannot capture buckling arising from the interaction of large distortions. SYSWELD's nonlinear geometry option treats strain as a nonlinear function of displacement, improving fidelity, though some discrepancy with experiments can remain [130]. To better represent bending kinematics, the bending-optimized setting was used: standard hexahedra were replaced, except within the HAZ, by *type 2* incompatible-mode elements that include additional shape functions for bending [131]. This choice enhances the accuracy of the computed distortions.

In thermo-mechanical welding simulations, the transient temperature field is solved first and then used to drive the mechanical analysis. The thermal field is

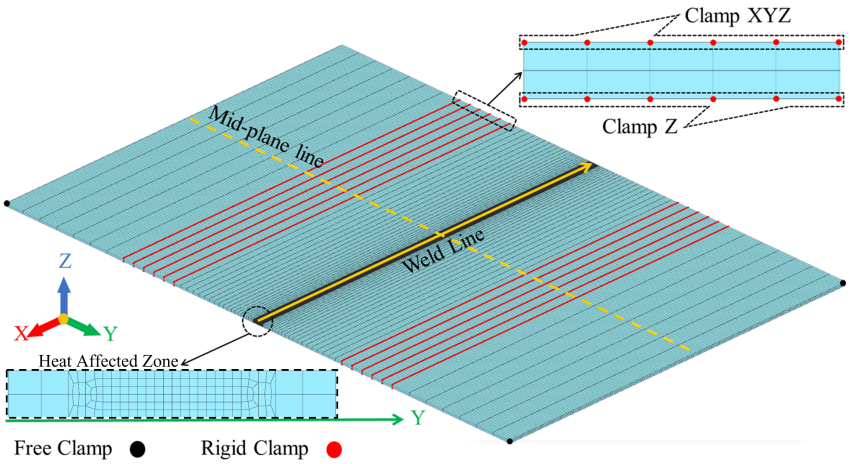


Fig. 6.3 Finite Element Model schematic and clamping positions.

governed by the classical heat diffusion equation [132]

$$\rho C_p \frac{\partial T}{\partial t} = \nabla \cdot (k \nabla T) + \dot{Q}, \tag{6.1}$$

where $\rho$ ($\mathrm{kg\,m^{-3}}$) is the material density, $C_p$ ($\mathrm{J\,K^{-1}\,kg^{-1}}$) is the specific heat capacity, $k$ ($\mathrm{W\,m^{-1}\,K^{-1}}$) is the thermal conductivity, $\dot{Q}$ ($\mathrm{W\,m^{-3}}$) is the internally generated heat per unit volume, and $T$ (K) is the temperature distribution. Solving Eq. 6.1 returns the transient distribution $T(x,y,z,t)$ over space and time, which is then mapped to the mechanical step.

Heat is also lost from the external plate surfaces by convection and radiation. In the model, skin elements exchange heat with the environment via Newton's cooling law and the Stefan–Boltzmann relation [132]. The initial temperature condition is

$$T(x,y,z,t)\big|t = 0 = T0, \tag{6.2}$$

where $T_0$ is set at room temperature. Convective and radiative heat losses result in the following boundary condition

$$k \nabla T \cdot \vec{\eta} = h_c (T - T_0) + \sigma \varepsilon (T^4 - T_0^4), \quad \forall (x,y,z) \in S, \tag{6.3}$$

where $S \subset \mathbb{R}^3$ is the set of plate surface points, $\vec{\eta}$ is normal vector to the surface point $(x,y,z)$, $h_c$ is the convection heat transfer coefficient, $\varepsilon$ is the emissivity, and $\sigma \approx 5.67 \cdot 10^{-8}\ \mathrm{W\,m^{-2}\,K^{-4}}$ is the Stefan-Boltzmann constant.

The computed temperature history $T(x,y,z,t)$ feeds the mechanical step, used to assess residual deformation and the stress state induced by the welding cycle. Temperature dependence of elastic–plastic properties and thermal expansion couples the thermal and mechanical problems.

The total strain at any node can be conceptually decomposed into elastic strain $\varepsilon_e$, plastic strain $\varepsilon_p$, thermal component $\varepsilon_{th}$, and strain from volumetric changes due to metallurgical phase transformations $\varepsilon_{phase}$:

$$\varepsilon = \varepsilon_e + \varepsilon_p + \varepsilon_{th} + \varepsilon_{phase}. \tag{6.4}$$

For aluminium sheet welding, deformation is dominated by elastic–plastic response and thermal dilatation; phase-transformation strains are negligible owing to the absence of significant solid-state changes [133]. Thermal strain is approximated as

$$\varepsilon_{th} = \alpha(T)(T - T_{ref})I, \tag{6.5}$$

where $T_{ref}$ is the reference temperature and $\alpha(T)$ is the temperature-dependent average coefficient of thermal expansion. Large thermal gradients cause non-uniform expansion and, upon cooling, differential contraction that leaves residual stress and distortion. When these effects are significant, geometric nonlinearity must be included. In that case, the Green–Lagrange strain tensor $E$ is employed to measure deformation relative to the undeformed configuration [134]:

$$E = \frac{1}{2}(F^T F - I), \tag{6.6}$$

where $I$ is the identity tensor, and $F$ is the deformation gradient tensor, mapping a material point from its initial position $p_0$ to its current position $p$, according to $p = \chi(p_0,t)$. Implementing these relations in an FEM framework enables solution of the coupled, nonlinear problem with temperature-dependent properties and appropriate constraints; post-processing yields residual stress fields and welding-induced distortions.

Clamping is represented with two node types (Figure 6.3). Three bottom-corner nodes act as free clamps to permit rigid-body motion. Rigid clamps emulate the test fixture: six rows of nodes on each plate's top surface are fully constrained in all directions, while six rows on the bottom surfaces are fixed only vertically [135]. All

clamps are active during melting; after fusion, rigid clamps are released, and free clamps remain until the end of the analysis.

For moving heat-source formulations in commercial FEM solvers such as SYSWELD, predictive accuracy typically relies on an iterative calibration step that reconciles the idealized source representation with the complexities of real welding.

A three-dimensional truncated-cone source with Gaussian intensity is commonly adopted for laser beams [136]. Figure 6.4 illustrates the geometric characteristics of the model, where $r_e$ and $r_i$ are the upper and lower radii of the cone, and $z_e$ and $z_i$ are the distances from the welding trajectory to the top and bottom surfaces of the heat source. The thermal energy delivered to the welding plates by a laser beam with power $P$ and absorption efficiency $\eta$ is defined in the laser reference system $(x_\ell, y_\ell, z_\ell)$ by [137]

$$\dot{Q}(x_\ell, y_\ell, z_\ell) = \frac{9\eta P \exp\left(3 - \frac{f_{las} r^2}{r_0^2}\right)}{\pi\left(1 - e^{-3}\right)(z_e - z_i)\left(r_e^2 - r_e r_i + r_i^2\right)}, \tag{6.7}$$

where $(x_\ell, y_\ell, z_\ell) = (0, 0, z_e)$ is the laser spot center, $f_{las} = 3$ is the heat source intensity factor [137], $r = \sqrt{x_\ell^2 + y_\ell^2}$ is the radial distance from the heat source center, and

$$r_0(z) = r_e - (r_e - r_i)\frac{(z_e - z_\ell)}{(z_e - z_i)}. \tag{6.8}$$

Assuming the laser moves at a velocity $v$ ($\mathrm{mm\,s^{-1}}$) along the $x$ direction in the global reference system, this results in

$$\begin{bmatrix} x \\ y \\ z \end{bmatrix} = \begin{bmatrix} x_0 + vt \\ y_0 \\ z_0 \end{bmatrix}, \tag{6.9}$$

where $(x_0, y_0, z_0)$ is the initial laser spot position.

Calibration proceeds by adjusting the heat-source parameters—upper and lower cone radii ($r_e$, $r_i$), cone height ($z_e - z_i$), and efficiency ($\eta$) [122]—and by defining the LOAD, i.e., the set of nodes instantaneously heated as the source traverses its prescribed path (Figure 6.5). The procedure is deemed successful when the simulated fusion-zone geometry (width, penetration depth, and asymmetry) reproduces metallographic cross-sections of the weld bead. Once this alignment is achieved, the

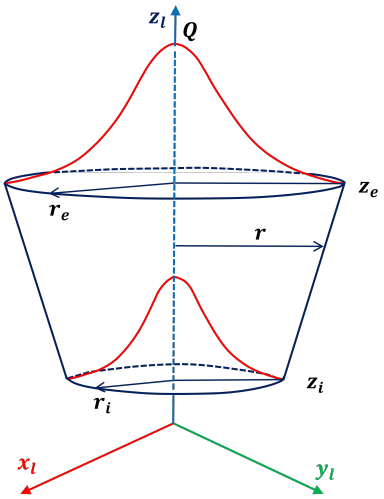


Fig. 6.4 3D Gaussian truncated conical heat source model.

model can be used to forecast temperature fields and mechanical distortion [136]. In practice, the workflow is operator-dependent and typically requires destructive specimen preparation and multiple simulation iterations.

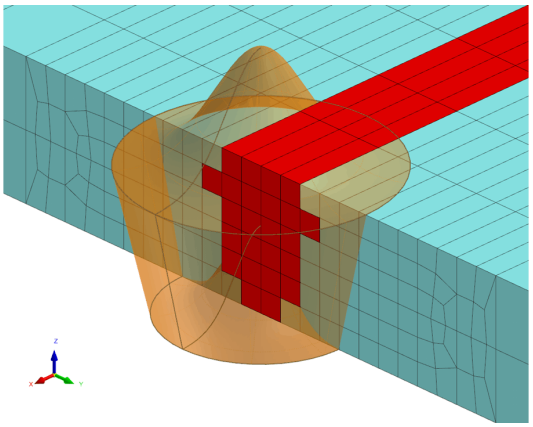

Fig. 6.5 Selected mesh elements (LOAD) heated by MHS.

### Imposed thermal cycle (T-ITC)

The moving heat source (MHS) formulation can provide high fidelity, but it becomes demanding for large or geometrically complex parts because it explicitly resolves a travelling heat source and the associated transient field. The Imposed Thermal Cycle (ITC) method is adopted as a pragmatic alternative with reduced modelling

complexity [138]. Rather than solving heat transfer from a travelling source, a prescribed thermal history is applied directly to selected regions of the model.

Although less physically explicit than MHS, ITC remains a practical option for studying mechanical deformation when a representative thermal cycle is available. Its effectiveness hinges on how well the thermal cycle and the affected region are defined; the reliability of thermo-mechanical predictions is therefore tightly coupled to the fidelity of the imposed temperature data. In the conventional ITC workflow (T-ITC), thermal cycles are extracted from a previously calibrated/validated MHS simulation [136]. The LOAD region is then chosen to replicate the melt-pool shape and dimensions obtained from the MHS model. As reported in [139], discrepancies between measured and simulated temperatures tend to grow near the weld line, primarily because the ITC scheme does not explicitly represent metal fusion. In SYSWELD's Visual-Viewer, temperature contour maps are used to delineate the molten zone; the nodes for the imposed cycles are taken along the outer boundary of this region (Figure 6.6). Extracted histories are pre-processed to remove offsets and any negative values, and to truncate the cooling tail—typically around 400°C for aluminium.

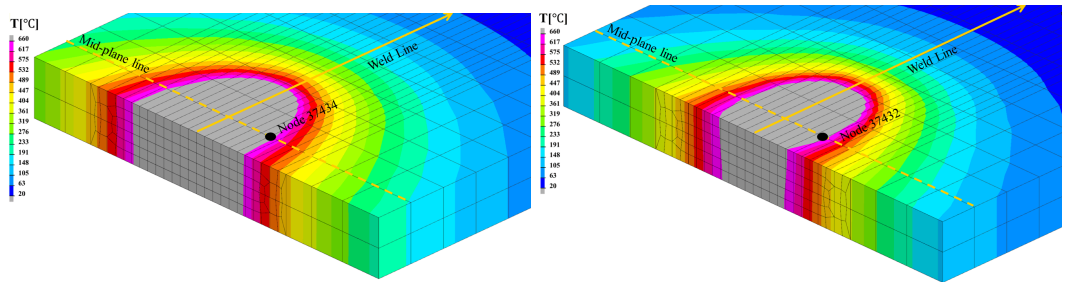


(a) (b)

Fig. 6.6 Thermal cycle extraction node positions from the moving heat source models: (a) Sample 1, (b) Sample 2.

### Infrared-guided imposed thermal cycle (IR-ITC)

In the T-ITC scheme, the imposed thermal history is typically extracted from a calibrated MHS simulation. It may also be obtained directly from experiments by measuring temperatures on the welded plates, commonly with contact thermocouples arranged along a line perpendicular to the seam to span the heat-affected zone [125, 136]. Thermocouples, however, provide sparse point measurements and require

physical contact and careful placement, which can be impractical for complex geometries or production environments.

In this study, an alternative approach is adopted: acquire the temperature field in real time with an infrared (IR) camera during welding. The measured thermal field is used to extract a representative thermal cycle outside the molten pool and to apply this cycle directly in the ITC model. Rather than calibrating heat-source parameters to match a macrography-driven melt-pool shape, the infrared-guided imposed thermal cycle (IR-ITC) uses thermography to constrain the thermal history that drives the mechanical response.

IR-ITC still requires selecting an appropriate LOAD (the region receiving the imposed cycle). Figure 6.7 illustrates three LOAD configurations used to study sensitivity.

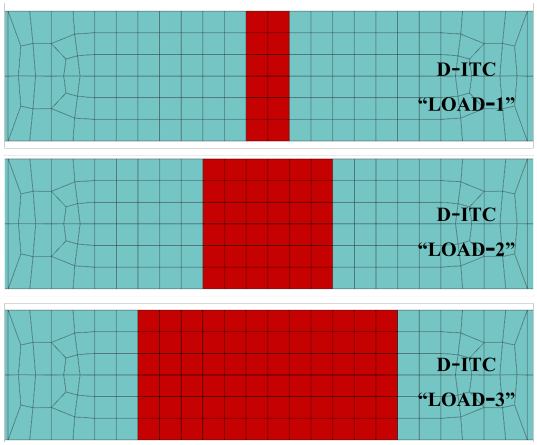


Fig. 6.7 Three different LOAD configurations for the IR-ITC method.

The three LOAD configurations were assessed in preliminary trials under the same experimental set-up. The narrowest LOAD-1 and LOAD-2 yielded the largest distortion errors in both samples, whereas the widest LOAD-3 produced the smallest errors. Based on this sensitivity analysis, LOAD-1 and LOAD-2 were not considered further and LOAD-3 was adopted for subsequent results. In the IR-ITC formulation, all elements within the LOAD are subjected to the same imposed thermal cycle throughout heating and cooling; therefore, the LOAD primarily controls the effective spatial footprint of the thermal loading and, consequently, the extent of thermal expansion/contraction and plastic strain that drives angular distortion. This trend indicates that overly localized thermal loading under-represents the effective

heated zone relevant to distortion, while a wider LOAD provides a more realistic approximation of the thermo-mechanically affected region adjacent to the weld.

## 6.6 Results and Discussion

### 6.6.1 Thermal analysis results

Thermal fields during welding were recorded by infrared thermography. A representative frame is reported in Figure 6.8 - (a).

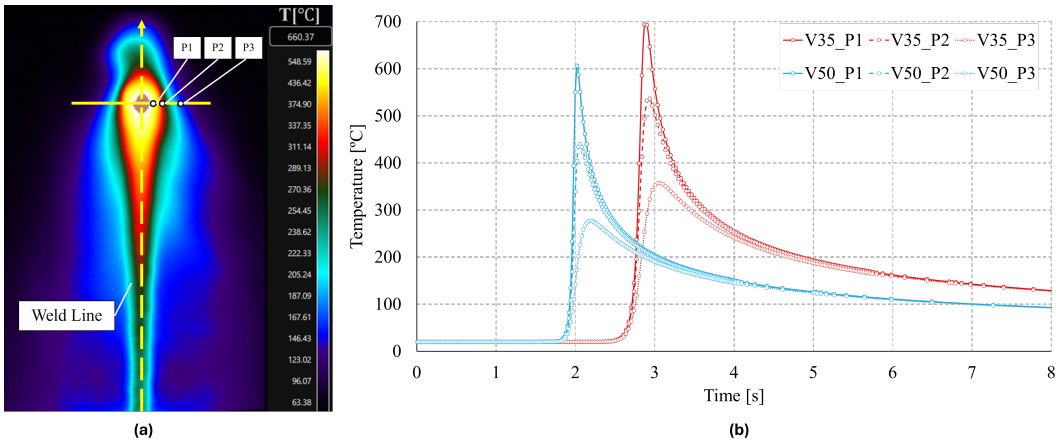


Fig. 6.8 (a) - Thermography map highlighting the weld pool; (b) - Temperature evolution at points P1–P3 along the central cross-section for Sample 1 and Sample 2.

From the temperature map, the melt-pool boundary can be inferred: the white area corresponds to temperatures at or above the melting point of aluminium, approximately 660 °C. Because IR temperature retrieval depends on emissivity—and emissivity varies with the material's state—the value for liquid aluminium differs from that of the solid, which can introduce error inside the weld pool. Despite this limitation, the frame shows a clear temperature gradient from the cooler outer edges (darker regions) toward the weld center (hotter, lighter), where the laser is focused (i.e., around 660 °C). The grey region at the center indicates pixel saturation at the camera's upper temperature limit. In this work, attention is placed on the thermal field just outside the molten zone but still within the joint, where emissivity is more stable and the measurements are considered more reliable.

More generally, laser welding can operate in a conduction regime (predominantly melting) or in a deep-penetration regime in which local vaporisation contributes to the formation of a keyhole, depending on the applied intensity. In thermographic maps, this transition is typically reflected by a more concentrated high-temperature core and steeper gradients near the interaction zone, while the surrounding field remains governed by heat diffusion into the base material [140]. For thin aluminium sheets, the temperature field is therefore expected to exhibit a narrow hot region around the weld line and a broader, rapidly decaying thermal footprint laterally, consistent with the high thermal conductivity of aluminium and the limited thickness available for through-thickness heat storage. The practical implication for IR-ITC is that thermal-cycle extraction should avoid the saturated/liquid core and target a repeatable location in the solid material adjacent to the pool boundary, where the measured history is less sensitive to emissivity transients and can be used as a robust thermal constraint.

The thermal cycles shown in Figure 6.8 - (b) were extracted from the thermograms at three locations (P1 $\sim$ 1.5 mm, P2 $\sim$ 2.55 mm, P3 $\sim$ 4.5 mm from the weld line), where the pixel-to-length conversion was obtained from the fixed acquisition geometry (camera IFOV and stand-off distance), accounting for the oblique viewing angle. It is possible to note the expected monotonic temperature decay with increasing distance from the weld centre, consistent with diffusive heat transport in the sheet. In addition, the temporal signatures reflect the different travel speeds: for the higher-speed case (Sample 2, v = 50 $mms^{-}1$) the temperature rise and peak occur earlier and the thermal transient is narrower, whereas the lower-speed case (Sample 1, v = 35 $mms^{-}1$) exhibits higher peak temperatures and a longer cooling tail, consistent with a higher linear heat input. As expected, P1 shows the steepest heating/cooling rates, while P2 and P3 display progressively smoother and delayed responses due to increased distance from the heat source.

The resulting thermal histories were subsequently imposed on the IR-ITC numerical models.

### 6.6.2 Distortion evaluation

During welding, the joint region is heated above the fusion temperature to ensure melting. The steep thermal gradients that develop during heating and subsequent

cooling drive volumetric expansion and contraction, which in turn generate plastic strain, residual stresses, and out-of-plane deformation—effects that are especially relevant in thin aluminium alloys. In thin sheets, the thermal field is highly non-uniform across both the width and the thickness: material near the weld line experiences large, localised heating, while colder surrounding regions and the fixture constrain free expansion. This restraint promotes compressive plastic strain during heating close to the weld line. Upon cooling, the same region undergoes contraction; because part of the strain is now plastic (irreversible), the contraction is not fully recovered elastically and tensile residual stresses remain near the weld, balanced by compressive stresses farther away. The resulting stress imbalance produces a bending moment that can drive angular distortion and, in extreme cases, buckling.

Angular distortion is a practical indicator because it condenses the global deformation state into a single metric that is directly linked to fit-up and dimensional tolerances. In this study, the mechanical performance of the numerical models was therefore evaluated by analysing the estimation errors between experimental and simulated distortion angles. To capture large-rotation effects and possible instability phenomena, all simulations were run with geometric nonlinearity enabled, in line with [130]. This choice is particularly important for thin-sheet welding, where small-deformation formulations can underpredict bending kinematics and may not reproduce the measured out-of-plane response when thermal loads are high and constraints are released.

Figure 6.9 shows the distortion angle extracted from the simulations and compared against profilometer measurements. The angle $\alpha$ was computed along a transverse section at the sheet midpoint, consistent with the experimental profilometer path, so that the simulated and measured metrics represent the same global deformation mode.

Table 6.1 Comparison of distortion angle results between IR-ITC simulation and experiments for Sample 1 and Sample 2.

| **Sample** | **Model** | **Angle** (°) | **Error** (%) |
|---|---|---|---|
| 1 | Simulation (IR-ITC) | 177.92 | 0.18 |
| | Experiment | 178.24 | |
| 2 | Simulation (IR-ITC) | 178.34 | 0.27 |
| | Experiment | 178.82 | |

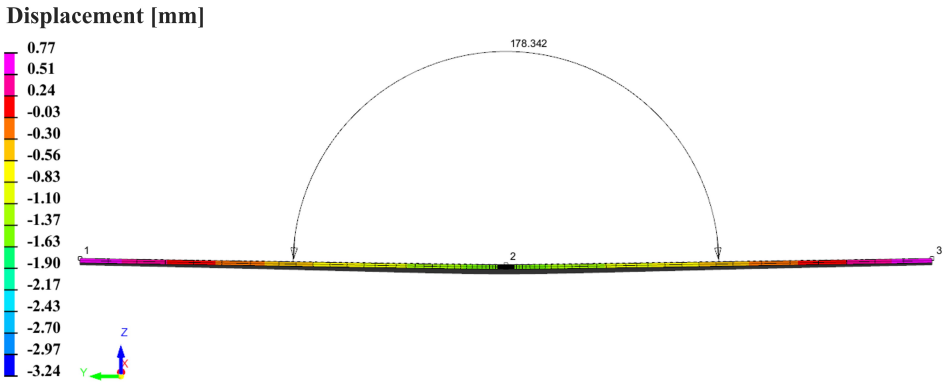


Fig. 6.9 Distortion angle measurement from numerical models.

Table 6.1 indicates close agreement between IR-ITC predictions and experimental measurements, with errors remaining below 0.3% for both samples. Overall, the agreement supports the premise of this chapter: thermography-derived thermal histories capture the dominant driver of distortion and can be used as a physically meaningful thermal constraint for component-scale distortion prediction.

### 6.6.3 Validation

To further validate the IR-ITC results, a moving heat source (MHS) simulation was performed using the same mesh configuration and model parameters. Fusion-zone cross-sections were extracted from the calibrated MHS model, and the thermal cycles predicted by MHS were used as input to a traditional imposed thermal cycle (T-ITC) simulation to compute distortions. Validation was therefore carried out at three levels: (i) comparison of cross-sectional geometry, (ii) comparison of thermal histories, and (iii) comparison of predicted distortions.

Figure 6.10 compares experimental cross-sections from Samples 1 and 2 with the corresponding MHS results. The Base Metal (BM) and Fusion Zone (FZ) are clearly discernible. Table 6.2 reports the fusion-zone dimensions obtained from the cross-sectional evaluation.

The smaller fusion zone in Sample 2 reflects the reduced linear heat input associated with the higher welding speed.

The low discrepancy between simulation and experimental cross-sections confirms that the MHS model is correctly calibrated for the investigated conditions.

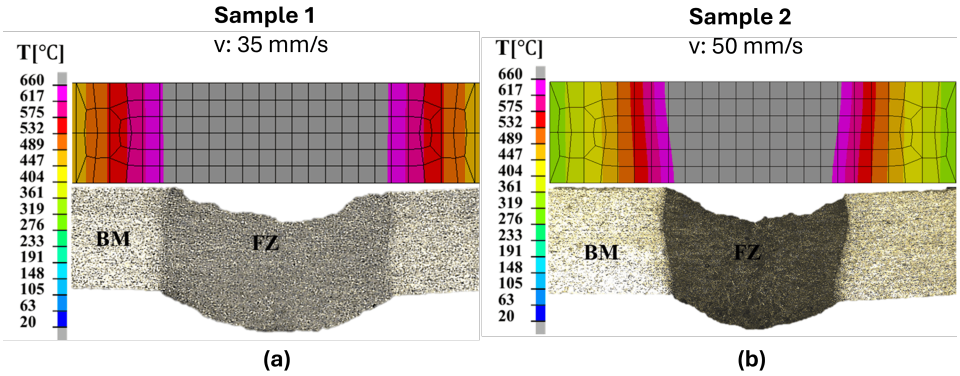


Fig. 6.10 Comparison of numerical and experimental fusion-zone morphology: (a) Sample 1, (b) Sample 2.

Table 6.2 Comparison of simulation and experimental weld pool dimensions.

| **Sample** | **Simulation (mm)** | | **Experiment (mm)** | |
|---|---|---|---|---|
| | $\mathbf{w_1}$ | $\mathbf{w_2}$ | $\mathbf{w_1}$ | $\mathbf{w_2}$ |
| 1 | 3.22 | 3.18 | 3.20 | 3.20 |
| 2 | 2.65 | 2.30 | 2.64 | 2.29 |

Thermal cycles were therefore extracted from the MHS simulation at three locations (P1 $\sim$ 1.5 mm, P2 $\sim$ 2.5 mm, P3 $\sim$ 4.5 mm from the weld line), selected to correspond to the locations used for thermography-based extraction.

To quantify how closely the constrained models reproduce measured temperatures at reference locations, instantaneous temperatures at P1–P3 were compared against experiment and an average difference ($Avg_{Diff}$) was computed as the mean absolute deviation across P1–P3.

Figure 6.12 further compares the thermal cycles imposed in the T-ITC and IR-ITC models for both samples. The close agreement supports that the thermography-derived constraint yields thermal histories that are consistent with those obtained from an MHS-based workflow.

Finally, Table 6.4 compares distortion angles obtained with T-ITC and IR-ITC against experiments for both samples. The comparable distortion errors indicate that, for the investigated cases, thermography-derived cycles provide constraints that are

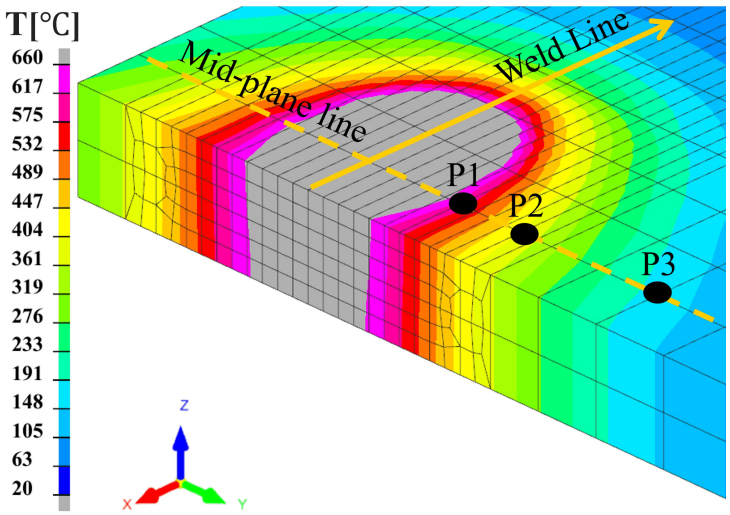


Fig. 6.11 Points of thermal cycle extraction from the MHS simulation.

Table 6.3 Comparison of simulated and experimental instantaneous temperatures at three selected locations (P1–P3) for different models and samples (units in °C).

| **Sample** | **Model** | **P1** | **P2** | **P3** | **Avg_Diff** (°C) |
|---|---|---|---|---|---|
| 1 | Experiment | 660 | 532 | 282 | – |
| | T-ITC | 695 | 521 | 245 | 35 |
| | IR-ITC | 655 | 506 | 248 | 32 |
| 2 | Experiment | 628 | 442 | 201 | – |
| | T-ITC | 620 | 431 | 159 | 29 |
| | IR-ITC | 600 | 435 | 168 | 31 |

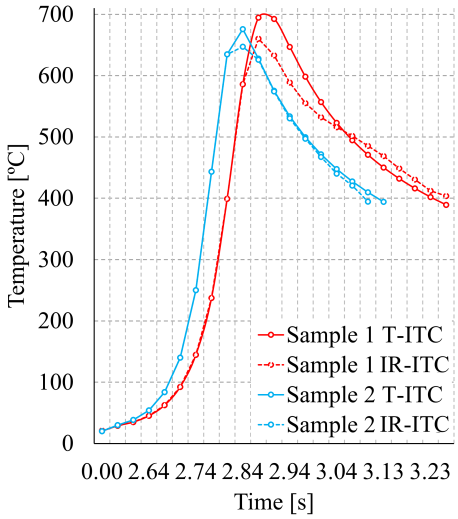


Fig. 6.12 Comparison between the thermal cycles imposed in the T-ITC model (MHS-derived) and the IR-guided thermal cycles (IR-ITC) for Sample 1 and Sample 2.

consistent with cycles extracted from an MHS-based workflow, supporting the use of IR-ITC as a thermography-driven route to distortion prediction.

Table 6.4 Comparison of distortion angle results between simulation models and experiments for Sample 1 and Sample 2.

| Sample | Model | Angle (°) | Error (%) |
|---|---|---|---|
| 1 | T-ITC | 177.97 | 0.15 |
| | IR-ITC | 177.92 | 0.18 |
| | Experiment | 178.24 | |
| 2 | T-ITC | 178.37 | 0.25 |
| | IR-ITC | 178.34 | 0.27 |
| | Experiment | 178.82 | |

“‘latex

## 6.7 Conclusion

This chapter presented a thermography-constrained thermo-mechanical FEM workflow to estimate welding-induced distortion in thin aluminium sheet laser welding. Infrared thermography provided time-resolved surface temperature fields during welding, and thermal cycles extracted from regions adjacent to the molten pool were

used to constrain the simulation input through an imposed thermal-cycle strategy (IR-ITC). For the investigated welding conditions and two travel speeds, the resulting angular-distortion estimates showed close agreement with profilometer measurements, supporting the feasibility of using in-process thermal sensing as a quantitative driver for component-scale distortion assessment.

From a process-monitoring perspective, the main implication is that the thermal history measured during welding contains actionable information on distortion propensity. By coupling thermography with a thermo-mechanical modelling pipeline, in-process thermal data can be translated into a physically grounded distortion indicator that can support distortion-risk flagging and structured evaluation of process settings and fixturing strategies at the component scale. Validation against an MHS/T-ITC workflow further substantiated the consistency of the thermography-derived thermal constraints with those obtained from a conventional, cross-section-calibrated moving-heat-source approach under the investigated conditions.

Several limitations must be acknowledged. Thermography-based temperature retrieval is sensitive to emissivity variation, pixel saturation, and line-of-sight constraints; therefore, thermal-cycle extraction should preferentially target solid regions outside the fully molten pool where emissivity is more stable and the sensor response remains within range. On the modelling side, predicted distortions remain sensitive to boundary conditions, particularly clamping and contact conditions, which must be represented consistently between experiments and simulations to ensure transferable distortion estimates.

Future developments should extend validation across broader process windows (travel speed, power, joint types) and more diverse fixturing conditions, and should investigate strategies to improve robustness of thermal-cycle extraction and interpretation (e.g., emissivity compensation, multi-region thermal features, and uncertainty quantification). More broadly, integrating thermography-driven thermal constraints with model-based distortion indicators provides a practical route toward in-line monitoring of distortion risk in laser-welded lightweight components. “‘

# Chapter 7

# Discussion and Industrial Implications

The thesis focused on in-process monitoring of laser welding and hybrid laser–arc welding, investigating three case studies in manufacturing-relevant contexts.

Each case study addresses monitoring at a different scale, ranging from local process stability during a single weld, to weld-section integrity, and ultimately to component-level dimensional quality. This multi-scale approach reflects the fact that weld quality is governed by different mechanisms at different scales; consequently, no single measurable quantity is sufficient for a comprehensive assessment. Transient instabilities in the laser–material interaction zone can initiate defects, deviations in penetration and fusion can compromise joint integrity, and the accumulation of residual stresses due to heat input can lead to distortion that is difficult to predict and control. For this reason, the three case studies should be interpreted as complementary rather than competing contributions, each providing information that is relevant at a specific decision level.

At the process scale, acoustic emissions measured by the optical microphone were sensitive to changes in keyhole behaviour during remote laser welding of thin aluminium overlap joints, including the transition from a blind keyhole to a passing-through keyhole associated with piercing. Photodiode spectral emissions provided complementary information, but their inclusion did not consistently improve discrimination beyond the acoustic channel within the investigated operating envelope.

At the weld-section scale, OCT enabled in-situ assessment of penetration depth in hybrid laser–arc welding of steel across the investigated process conditions, from pure hybrid synergy to more tandem-like behaviour. The primary constraint was the measurement capability of the OCT system, which limited the maximum usable depth estimate and could be further affected by optical disturbances.

At the component scale, infrared thermography provided in-process thermal histories that could be used as constraints for thermo-mechanical simulation, enabling reliable prediction of welding-induced distortion within the investigated thin-sheet aluminium conditions. The reliability of this link depends on the measurement configuration and on modelling assumptions, particularly those governing surface temperature interpretation.

Because the measured signals arise from coupled physical mechanisms, partial overlap in the conveyed information is expected across sensing modalities. The key point is therefore to exploit complementarity while avoiding unnecessary redundancy, which can increase model complexity without improving decision performance. A further step outside the scope of this thesis is the development of an integrated framework that combines outputs across the three scales into a unified assessment, validated against common acceptance criteria and decision rules.

## 7.1 Answers to Research question

**RQ1: What information on process stability and keyhole-regime transitions can be extracted from acoustic and optical emissions during remote laser welding of thin aluminium sheets?**

Acoustic emissions provided information on process stability and keyhole-regime transitions, including identification of the blind-to-passing-through keyhole transition associated with piercing. Photodiode spectral emissions were complementary, but their inclusion did not consistently improve discrimination beyond the acoustic channel within the investigated operating envelope.

**RQ2: Under which process conditions and configurations can optical coherence tomography provide accurate and reliable in-situ measurements of penetration depth during hybrid laser–arc welding of steels?**

OCT provided reliable in-situ penetration-depth measurements across the investigated process conditions, from pure hybrid welding where the two heat sources act in synergy to tandem welding where they act more separately. The main limitation was the maximum measurable penetration depth, which was constrained by the OCT system capability rather than by the welding process itself.

**RQ3: Can infrared thermography provide in-process thermal constraints that enable reliable thermo-mechanical prediction of welding-induced distortion?**

Infrared thermography provided in-process thermal histories that could be used as constraints for thermo-mechanical simulation, enabling reliable prediction of welding-induced distortion within the investigated thin-sheet aluminium welding conditions. The main limitations are linked to the measurement configuration and modelling assumptions, particularly emissivity and whether the measured surface temperatures adequately represent the through-thickness thermal field driving distortion.

**RQ: To what extent can acoustic, optical, and thermal sensing be translated into robust, quantitative, and industrially actionable indicators of weld quality and process stability in laser and hybrid laser–arc welding?**

Within the operating envelopes validated in this thesis, the sensing approaches provided quantitative outputs that are industrially actionable for monitoring and quality screening: acoustic features enabled weld-condition discrimination with test accuracy up to 98.15%, OCT penetration-depth estimates matched metallography at the percent level in favourable conditions (e.g. $\sim$1% average error in laser-leading configuration, up to an effective depth of $\sim$6 mm), and thermography-constrained simulations predicted angular distortion with errors below 0.3% against profilometry. The extent of this actionability is therefore high within the validated setups (process-state detection, penetration monitoring, and distortion-risk assessment), while broader transferability and progression toward closed-loop control remain constrained by configuration-dependent disturbances, sensor-specific limitations, and the need for further long-run validation under production variability.

## 7.2 Industrial applicability and scalability

To assess the practical relevance of in-process monitoring in industrial production—including its potential impact on cost, efficiency, and resource use—a scenario-based cost analysis was performed for the three application contexts considered in this thesis.

Table 7.2 provides a scenario-based estimate of the economic envelope for deploying a full monitoring framework across the three application contexts analysed in this thesis. In all three cases, the annualised monitoring cost remains small compared with the estimated defect-related costs, leading to positive net annual benefits across the considered ranges and payback times spanning months to a few years, depending on defect prevalence and on the contribution of late defect discovery. The spread of the estimates highlights that the business case is primarily driven by application-specific factors (production volume, number of stations, and the cost of rework, scrap, and late detection), and that monitoring solutions should therefore be selected and qualified against the decision needs and disturbance conditions of the target production environment.

Entries marked with * are scenario assumptions and/or model-derived quantities computed from assumed inputs. For BeV, the column is referenced to Tesla-style cylindrical-cell packs; published sources report that Tesla Model S–type packs comprise 16 modules and 7,104 18650 cells [141]. The weld-count range used here (28,000–57,000 welds/pack) remains a scenario input (marked with *), reflecting the fact that the number of welded connections depends on pack architecture and on the number of welds per connection.

The BiW volume (300,000 vehicles/year) is anchored to a representative OEM plant capacity (BMW Group Plant Spartanburg) [142]. For BiW, the weld count is treated as spot joining (i.e. laser spot / discrete spot-like joints rather than continuous seam welding); the range 5,000–7,000 joints per body is consistent with published values for typical body-in-white structures [143].

For piping, the campaign length (105 km) is anchored to the TAP offshore pipeline project (Adriatic Sea) [144]. The girth-weld density range (19–83 welds/km) reflects common offshore prefabrication strategies: approximately 83 joints/km for standard 12 m single joints and approximately 19 joints/km for quad-joint strings up to about 52 m, as reported in industrial documentation [144, 145]. The piping

Table 7.2 Monitoring costs analysis

| Metric | BeV | BiW | Piping |
|---|---|---|---|
| **Production volumes** | | | |
| Annual production | 85,133 | 300,000 | 105 (km/yr) |
| Welds per unit | 28,000–57,000 | 5,000–7,000 | 19–83 girth |
| Total annual welds | 2.4–4.9 billion | 1.5–2.1 billion | 1,995–8,715 |
| Stations to equip | ∼20–60* | 18–30* | 6–10* |
| **Baseline defect costs** | | | |
| Defect rate (per weld) | 0.05–0.10%* | ≤0.10%* | 1–3% |
| Annual scrap/rework | 2.7–7.2M* | 1.2–4.5M* | 0.06–1.20M* |
| Field-failure cost | 0.1–1.3M* | 0.0–0.5M* | 1–10M* |
| **Total annual defect cost (baseline)** | **2.8–8.5M*** | **1.2–5.0M*** | **1.1–11.2M*** |
| **Monitoring investment** | | | |
| CapEx (sensors) | 0.6–1.0M | 1.5–2.5M | 0.9–1.5M |
| OpEx (maintenance/yr) | 0.06–0.10M | 0.20–0.25M | 0.10–0.15M |
| 5-year total cost | 0.90–1.50M | 2.50–3.75M | 1.40–2.25M |
| **Annual savings with monitoring (gross)** | | | |
| Defect cost avoidance (assume 80% catch) | 2.2–5.7M* | 1.0–3.6M* | 0.05–0.96M* |
| Risk/field-failure reduction (assume 80% reduction) | 0.1–1.0M* | 0.0–0.4M* | 0.8–8.0M* |
| **Total annual saving (gross)** | **2.3–6.8M*** | **1.0–4.0M*** | **0.8–9.0M*** |
| **Return of Investment metrics** | | | |
| Annualised monitoring cost (CapEx/5 + OpEx) | 0.2–0.3M* | 0.5–0.8M* | 0.3–0.4M* |
| Net annual benefit (gross saving - annual cost) | 2.0–6.6M* | 0.2–3.5M* | 0.4–8.7M* |
| Payback period (CapEx/(gross saving - OpEx)) | 1.1–5.5 months* | 4.7–40.0 months* | 1.2–27.7 months* |
| 5-year ROI (net/cost) | 653–3667%* | 32–692%* | 89–3100%* |

repair-rate range (1–3%) follows typical weld repair rates reported by TWI based on an industry survey [146]. CapEx/OpEx sensor costs are based on distributor quotations (not publicly referenced by design).

Under the considered scenarios, Table 7.2 suggests annual gross savings on the order of $\sim$1–9 M€/yr depending on the application context, primarily through reduced scrap/rework and mitigation of late defect discovery. The magnitude of the benefit is therefore plausible, but it depends critically on how monitoring outputs translate into decisions and actions in production.

Scalability is considered here in terms of how effort and performance evolve when moving from a single monitored station to multiple stations, accounting for hardware cost, integration and maintenance burden, and the feasibility of real-time decision-making. Scalability is considered here in terms of how effort and performance evolve when moving from a single monitored station to multiple stations, accounting for hardware cost, integration and maintenance burden, and the feasibility of real-time decision-making. In particular, scalability is discussed by assessing whether the sensing concept and processing pipeline can move beyond laboratory conditions into production: whether the sensors can be integrated on industrial machines, whether acquisition and processing times are compatible with production cycle time, and whether deployment requires special setups, frequent recalibration, or extensive algorithm training and re-training.

Acoustic and spectral sensing have a relatively low per-station hardware cost, a small data footprint, and straightforward real-time processing, making them suitable for 100% inspection and screening at takt time. The main scaling challenge is not computation, but station-to-station variability (mounting repeatability, acoustic coupling, background noise, and optics contamination), which motivates standardised installation and shielding together with periodic baseline checks to manage drift.

Optical coherence tomography (OCT) is more expensive and more sensitive to alignment and optical-path disturbances, so scaling is most justified for high-value welds or when penetration is the dominant critical-to-quality variable. Practical deployment benefits from standardised optics protection and from stability metrics that gate the depth estimate, reducing the risk of acting on degraded signals and limiting nuisance alarms.

Infrared thermography can be scaled from a sensing perspective, but full thermo-mechanical simulation typically scales as a near-line (batch) workflow rather than as

inline control unless simplified. The approach remains scalable as a qualification tool, for process-window validation, or for distortion-risk flagging where minute-level latency is acceptable. Real-time closed-loop control at station level would likely require surrogate models or reduced-order representations, together with additional validation under production variability.

The economic figures in Table 7.2 should be interpreted as an upper-envelope estimate, because they implicitly assume that monitoring outputs can be translated into effective corrective actions with limited missed detections and limited nuisance alarms. In practice, the achievable benefit depends on the balance between false negatives (undetected defects) and false positives (unnecessary interventions), and on whether the production system can respond in time without creating disruption.

Even if sensing and classification performance were ideal, closing the loop is not trivial: real-time control requires low-latency acquisition, processing, and actuation, as well as a stable mapping between the monitored signature and the control variable under production variability. For this reason, the near-term industrial value of monitoring is often highest in screening and diagnostic use (early detection, targeted re-inspection, parameter-drift detection), while full closed-loop control typically requires additional engineering effort and validation beyond the monitoring layer.

Finally, achievable performance is bounded by sensor-specific constraints: acoustic monitoring is sensitive to station-dependent noise and coupling, OCT performance is limited by optical-path disturbances and by the usable measurement range of the system, and infrared thermography provides only surface temperatures, which must be interpreted through modelling assumptions when predicting through-thickness thermal effects and distortion.

# Chapter 8

# Conclusions

This thesis investigated in-process monitoring strategies for laser welding and hybrid laser–arc welding in three manufacturing-relevant application contexts. The work aimed to translate sensor signals into quantitative outputs that support weld-quality assessment at the process, weld-section, and component levels, and to clarify the conditions under which these outputs remain reliable.

## 8.1 Main findings and contributions

The thesis demonstrated that meaningful monitoring outputs can be obtained using complementary sensing approaches when the target decision and operating envelope are clearly defined. At the process scale, acoustic emissions measured by a membrane-free optical microphone provided sensitive signatures of process stability and keyhole-regime transitions in remote laser welding of thin aluminium overlap joints, including the transition from a blind to a passing-through keyhole associated with piercing. At the weld-section scale, OCT enabled in-situ penetration-depth monitoring in hybrid laser–arc welding of steel, with reliability dependent on process configuration and on the stability of the optical path. At the component scale, infrared thermography provided in-process thermal histories that could be used to constrain thermo-mechanical simulation, enabling prediction of welding-induced distortion in thin aluminium within the investigated conditions.

Beyond the individual case studies, a central contribution of the thesis is the demonstration of validated, application-oriented workflows that connect sensor

measurements to actionable monitoring outputs, together with a critical discussion of scalability, integration constraints, and the practical meaning of “actionable” monitoring in production.

## 8.2 Limitations

The results of this thesis should be interpreted within the boundaries of the investigated materials, joint types, and process conditions. Each monitoring workflow was validated over a limited range of parameters and under controlled experimental conditions; broader generalisation to other materials, surface conditions, shielding strategies, and shop-floor environments was not systematically investigated due to time and resource constraints. In particular, station-to-station variability, long-run drift, and the influence of disturbances typical of production (e.g. contamination of optics, changing acoustic backgrounds, and variability in fixturing and joint preparation) are expected to affect performance and require dedicated validation.

A further limitation is that the thesis did not implement a unified, end-to-end monitoring framework combining all sensing modalities into a single decision system. While each case study provides evidence at its own decision level, integrating acoustic, optical, OCT, and thermographic information into a coherent multi-sensor monitoring architecture—with common acceptance criteria, uncertainty handling, and decision logic—remains outside the scope of the present work.

## 8.3 Outlook and future developments

Future work should expand validation across a wider set of materials and industrial environments, with emphasis on long-run robustness, drift management, and quantification of false-alarm rates under production variability. A second priority is the development of an integrated monitoring framework that combines outputs from multiple sensors and decision levels in a principled manner (e.g. hierarchical decision fusion or confidence-gated logic), linking process signatures to weld geometry and ultimately to component performance.

Finally, progressing from monitoring to closed-loop control will require careful consideration of latency, actuation limits, and the stability of the mapping between

monitored signatures and control variables. In the near term, the most immediate industrial impact is expected from monitoring strategies that support screening and diagnostic functions, enabling earlier detection of instabilities, targeted re-inspection, and reduction of scrap and rework.

## 8.4 Closing remarks

Overall, the thesis provides experimentally validated workflows and evidence-based boundary conditions for deploying in-process monitoring in laser and hybrid laser–arc welding. These results support more reliable and economically sustainable welding operations, and they lay the groundwork for future production-ready monitoring and control systems.

# References


[1] American Welding Society (AWS) - Welding Excellence Worldwide.

[2] Global Market Insights. Welding Consumables Market Size & Share, Statistics Report 2034. Technical report, Global Market Insights, 2014.

[3] Junbo Feng, Peilei Zhang, Hua Yan, Haichuan Shi, Qinghua Lu, Zhenyu Liu, Di Wu, Tianzhu Sun, Ruifeng Li, and Qingzhao Wang. Application of Laser Welding in Electric Vehicle Battery Manufacturing: A Review. *Coatings 2023, Vol. 13, Page 1313*, 13(8):1313, 7 2023.

[4] Bappa Acherjee. Hybrid laser arc welding: State-of-art review, 2 2018.

[5] Seiji Katayama. *Fundamentals and Details of Laser Welding*. Topics in Mining, Metallurgy and Materials Engineering. Springer Singapore, Singapore, 2020.

[6] Ettore Carpene, Daniel Höche, Peter Schaaf, and E Carpene. *Fundamentals of Laser-Material Interactions*. Springer Nature, 2010.

[7] Ion N Mihailescu, Jörg Hermann, I N Mihailescu, and J Hermann. *Laser-Plasma Interactions*. Elsevier, 2006.

[8] Ivan Bunaziv, Odd M. Akselsen, Xiaobo Ren, Bård Nyhus, and Magnus Eriksson. Laser Beam and Laser-Arc Hybrid Welding of Aluminium Alloys. *Metals 2021, Vol. 11, Page 1150*, 11(8):1150, 7 2021.

[9] Dirk Petring and Christian Fuhrmann. Recent progress and innovative solutions for Laser-Arc Hybrid Welding. In Milan Brand and Erol Harvey, editors, *1st Pacific International Conference on Application of Lasers and Optics 2004*. Fraunhofer Institute for Laser Technology, 2004.

[10] H. Staufer. Laser Hybrid Welding and Laser Brazing at Audi And VW. *Welding in the World*, 50, 2006.

[11] U. Dilthey, U. Reisgen, and S. Olschok. Robot application for laser-GMA hybrid welding in shipbuilding. In *ICALEO 2007*, pages 308–315, 2007.

[12] Janusz Adamiec, Michał Wiecek, and Wojciech Gawrysiuk. Fibre laser usage in boiler elements' production for the power industry. *Welding International*, 24(11):853–860, 2010.

[13] Kai Li, Guangzhong He, Hongxiao Wang, and Chunsheng Wang. Hybrid laser-arc welding process of full penetration T joint in high speed railway vehicle bogie. *https://doi.org/10.1117/12.2544117*, 11333:174–182, 12 2019.

[14] J. Zhou, T.T. Zhang, H.L. Tsai, and P.C. Wang. Hybrid laser-arc welding in aerospace engineering. *Welding and Joining of Aerospace Materials*, pages 123–156, 1 2021.

[15] Zhang Shenghai, Shen Yifu, and Qiu Huijuan. The technology and welding joint properties of hybrid laser-tig welding on thick plate. *Optics & Laser Technology*, 48:381–388, 6 2013.

[16] Fanrong Kong, Junjie Ma, and Radovan Kovacevic. Numerical and experimental study of thermally induced residual stress in the hybrid laser–GMA welding process. *Journal of Materials Processing Technology*, 211(6):1102–1111, 6 2011.

[17] Ting Liu, Fei Yan, Sang Liu, Ruoyang Li, Chunming Wang, and Xiyuan Hu. Microstructure and mechanical properties of laser-arc hybrid welding joint of GH909 alloy. *Optics & Laser Technology*, 80:56–66, 6 2016.

[18] G. Casalino, S. L. Campanelli, U. Dal Maso, and A. D. Ludovico. Arc Leading Versus Laser Leading in the Hybrid Welding of Aluminium Alloy Using a Fiber Laser. *Procedia CIRP*, 12:151–156, 1 2013.

[19] M. Mazar Atabaki, M. Nikodinovski, P. Chenier, J. Ma, W. Liu, and R. Kovacevic. Experimental and numerical investigations of hybrid laser arc welding of aluminum alloys in the thick T-joint configuration. *Optics & Laser Technology*, 59:68–92, 7 2014.

[20] Paul Kah, Belinga Mvola, Jukka Martikainen, and Raimo Suoranta. Real time non-destructive testing methods of welding. In *Advanced Materials Research*, volume 933, pages 109–116. Trans Tech Publications, 2014.

[21] Masoud Shaloo, Martin Schnall, Thomas Klein, Norbert Huber, and Bernhard Reitinger. A Review of Non-Destructive Testing (NDT) Techniques for Defect Detection: Application to Fusion Welding and Future Wire Arc Additive Manufacturing Processes, 5 2022.

[22] Wang Cai, Jian Zhuang Wang, Ping Jiang, Long Chao Cao, Gao Yang Mi, and Qi Zhou. Application of sensing techniques and artificial intelligence-based methods to laser welding real-time monitoring: A critical review of recent literature. *Journal of Manufacturing Systems*, 57:1–18, 10 2020.

[23] John Stavridis, Alexios Papacharalampopoulos, and Panagiotis Stavropoulos. Quality assessment in laser welding: a critical review, 2 2018.

[24] D. Y. You, X. D. Gao, and S. Katayama. Review of laser welding monitoring. *Science and Technology of Welding and Joining*, 19(3):181–201, 4 2014.

[25] Yi Wei Huang, Xiang Dong Gao, Perry P. Gao, Bo Ma, and Yan Xi Zhang. Laser welding monitoring techniques based on optical diagnosis and artificial intelligence: a review. *Advances in Manufacturing*, 2024.

[26] Joseph M. Schmitt. Optical Coherence Tomography (OCT): a review. *IEEE Journal on Selected Topics in Quantum Electronics*, 5(4):1205–1215, 7 1999.

[27] Maryna Speka, Simone Matteï, Michel Pilloz, and Mariana Ilie. The infrared thermography control of the laser welding of amorphous polymers. *NDT & E International*, 41(3):178–183, 4 2008.

[28] Shanglu Yang, Rouzbeh Sarrafi, and Radovan Kovacevic. Monitoring of hybrid laser-arc welding of galvanized steels in a gapfree lap joint configuration. *ICALEO 2009 - 28th International Congress on Applications of Lasers and Electro-Optics, Congress Proceedings*, 102:71–78, 11 2009.

[29] H.-S. Kang and J.-W. Noh. Study on laser hybrid welding process monitoring. In *International Conference on Control, Automation and Systems*, pages 1388–1390, 2013.

[30] Dario Basile, Rehab Al Botros, Manuela De Maddis, Valentino Razza, and Pasquale Franciosa. Monitoring part-to-part gap and laser power effects in remote laser welding of 1050 aluminum busbar-to-terminal connections via optical microphone sensing. *Optics & Laser Technology*, 192:113494, 12 2025.

[31] T. Klein, M. Vicanek, J. Kroos, I. Decker, and G. Simon. Oscillations of the keyhole in penetration laser beam welding. *Journal of Physics D: Applied Physics*, 27(10):2023, 10 1994.

[32] M. Geiger, K. H. Leitz, H. Koch, and A. Otto. A 3D transient model of keyhole and melt pool dynamics in laser beam welding applied to the joining of zinc coated sheets. *Production Engineering*, 3(2):127–136, 6 2009.

[33] Jörg Volpp and Daniel Freimann. Indirect measurement of keyhole pressure oscillations during laser deep penetration welding. *ICALEO 2013 - 32nd International Congress on Applications of Lasers and Electro-Optics*, pages 334–340, 10 2013.

[34] Klaus Schricker, Leander Schmidt, Hannes Friedmann, Christian Diegel, Marc Seibold, Peter Hellwig, Fabian Fröhlich, Jean Pierre Bergmann, Falk Nagel, Peter Kallage, Alexander Rack, Herwig Requardt, and Yunhui Chen. Characterization of keyhole dynamics in laser welding of copper by means of high-speed synchrotron X-ray imaging. In *Procedia CIRP*, volume 111, pages 501–506. Elsevier B.V., 2022.

[35] Zhongyi Luo, Leshi Shu, Ping Jiang, Shaoning Geng, Deyuan Ma, and Di Wu. Study on the keyhole oscillation mechanism of laser welding based on electro-mechano-acoustical analogy theory. *Journal of Materials Processing Technology*, 331, 10 2024.

[36] Yi Luo, Liang Zhu, Jingtao Han, Xiaojian Xie, Rui Wan, and Yang Zhu. Study on the acoustic emission effect of plasma plume in pulsed laser welding. *Mechanical Systems and Signal Processing*, 124:715–723, 6 2019.

[37] M. Bastuck. *In-Situ-Uberwachung von LaserschweiBprozessen mittels hoherfrequenter Schallemissionen*. PhD thesis, universität des saarlandes, 2016.

[38] Petr Horník, Hana Šebestová, Jan Novotný, and Libor Mrňa. Visualization of laser back-reflection distribution during laser welding. *IOP Conference Series: Materials Science and Engineering*, 1135(1):012015, 11 2021.

[39] Xudong Zhang, Wuzhu Chen, Eiji Ashida, and Fukuhisa Matsuda. Relationship between weld quality and optical emissions in underwater Nd: YAG laser welding. *Optics and Lasers in Engineering*, 41(5):717–730, 5 2004.

[40] Yuan Li, Junyu Guo, and Erkan Caner Ozkat. Photodiode Signal Patterns: Unsupervised Learning for Laser Weld Defect Analysis. *Processes 2025, Vol. 13, Page 121*, 13(1):121, 1 2025.

[41] S. Bagavathiappan, B. B. Lahiri, T. Saravanan, John Philip, and T. Jayakumar. Infrared thermography for condition monitoring – A review. *Infrared Physics & Technology*, 60:35–55, 9 2013.

[42] Gerhard Kramm and Nicole Mölders. Planck's blackbody radiation law: Presentation in different domains and determination of the related dimensional constants. Technical report.

[43] Eric Wasilewski, Nikolay Doynov, Ralf Ossenbrink, and Vesselin Michailov. Investigations on the thermal conditions during laser beam welding of high-strength steel 100Cr6. *Advances in Industrial and Manufacturing Engineering*, 6:100118, 5 2023.

[44] Chao Hu and Xi Zhang Chen. A review and preliminary experiment on application of infrared thermography in welding. *Advances in Intelligent Systems and Computing*, 363:351–359, 2015.

[45] Adam Sajek and Jerzy Nowacki. Comparative evaluation of various experimental and numerical simulation methods for determination of t8/5 cooling times in HPAW process weldments. *Archives of Civil and Mechanical Engineering*, 18(2):583–591, 2 2018.

[46] Balthasar Fischer. Optical microphone hears ultrasound. *Nature Photonics*, 10(6):356–358, 6 2016.

[47] Nicolas Authier, Enzo Touzet, Fabian Lücking, Ryan Sommerhuber, Vincent Bruyere, and Patrick Namy. Coupled membrane free optical microphone and optical coherence tomography keyhole measurements to setup welding laser parameters. In *High-Power Laser Materials Processing: Applications, Diagnostics, and Systems IX*, page 8. SPIE-Intl Soc Optical Eng, 3 2020.

[48] PHOTODIODE BASICS – Wavelength Electronics.

[49] David Huang, Eric A. Swanson, Charles P. Lin, Joel S. Schuman, William G. Stinson, Warren Chang, Michael R. Hee, Thomas Flotte, Kenton Gregory, Carmen A. Puliafito, and James G. Fujimoto. Optical Coherence Tomography. *Science*, 254(5035):1178–1181, 11 1991.

[50] Thibault Bautze and Markus Kogel-Hollacher. Keyhole Depth is just a Distance. *Laser Technik Journal*, 11(4):39–43, 9 2014.

[51] Thibault Bautze, Rüdiger Moser, Matthias Strebel, and Markus Kogel-Hollacher. Use of inline coherent imaging for laser welding processes: Process control and beyond. Technical report, Precitec GmbH & Co. KG, 2015.

[52] The Differences Between SWIR, MWIR, and LWIR Cameras.

[53] Nikolay Doynov. Large-scale distortion analysis of the welding and thermal straightening process chain. *Machines. Technologies. Materials.*, 19(2):57–61, 2025.

[54] Joris Jaguemont and Fanny Bardé. A critical review of lithium-ion battery safety testing and standards. *Applied Thermal Engineering*, 231:121014, 8 2023.

[55] Junbo Feng, Peilei Zhang, Hua Yan, Haichuan Shi, Qinghua Lu, Zhenyu Liu, Di Wu, Tianzhu Sun, Ruifeng Li, and Qingzhao Wang. Application of Laser Welding in Electric Vehicle Battery Manufacturing: A Review. *Coatings 2023, Vol. 13, Page 1313*, 13(8):1313, 7 2023.

[56] M. F.R. Zwicker, M. Moghadam, W. Zhang, and C. V. Nielsen. Automotive battery pack manufacturing – a review of battery to tab joining. *Journal of Advanced Joining Processes*, 1:100017, 3 2020.

[57] Gökan May and Dimitris Kiritsis. Zero Defect Manufacturing Strategies and Platform for Smart Factories of Industry 4.0. *Lecture Notes in Mechanical Engineering*, pages 142–152, 2019.

[58] Giovanni Chianese, Pasquale Franciosa, Jonas Nolte, Darek Ceglarek, and Stanislao Patalano. Characterization of Photodiodes for Detection of Variations in Part-to-Part Gap and Weld Penetration Depth During Remote Laser Welding of Copper-to-Steel Battery Tab Connectors. *Journal of Manufacturing Science and Engineering, Transactions of the ASME*, 144(7), 7 2022.

[59] M. F. M. Yusof, Mahadzir Ishak, and Mohd Fairusham Ghazali. Acoustic methods in real-time welding process monitoring: Application and future potential advancement. *Journal of Mechanical Engineering and Sciences*, 15(4):8490–8507, 12 2021.

[60] Milad Hamidi Nasab, Giulio Masinelli, Charlotte de Formanoir, Lucas Schlenger, Steven Van Petegem, Reza Esmaeilzadeh, Kilian Wasmer, Ashish Ganvir, Antti Salminen, Florian Aymanns, Federica Marone, Vigneashwara Pandiyan, Sneha Goel, and Roland E. Logé. Harmonizing sound and light: X-ray imaging unveils acoustic signatures of stochastic inter-regime instabilities during laser melting. *Nature Communications*, 14(1), 12 2023.

[61] Charlotte de Formanoir, Milad Hamidi Nasab, Lucas Schlenger, Steven Van Petegem, Giulio Masinelli, Federica Marone, Antti Salminen, Ashish Ganvir, Kilian Wasmer, and Roland E. Logé. Healing of keyhole porosity by means of defocused laser beam remelting: Operando observation by X-ray imaging and acoustic emission-based detection. *Additive Manufacturing*, 79:103880, 1 2024.

[62] Camilo Prieto, Roberto Fernandez, Carlos Gonzalez, Marcos Diez, Jorge Arias, Ryan Sommerhuber, and Fabian Lücking. In situ process monitoring by optical microphone for crack detection in Laser Metal Deposition applications. In *LANE*, 2020.

[63] Christian Lutz, Cemal Esen, and Ralf Hellmann. Layer detection in ultrashort pulsed multilayer laser ablation by analyzing ultrasonic process emission. *Journal of Laser Applications*, 37(2), 5 2025.

[64] Christian Lutz, Ryan Sommerhuber, Matthias Kettner, Cemal Esen, and Ralf Hellmann. Towards process control by detecting acoustic emissions during ultrashort pulsed laser ablation of multilayer materials. In *Laser-based Micro- and Nanoprocessing XVIII*, page 51. SPIE-Intl Soc Optical Eng, 3 2024.

[65] Andreas Krämer. Influence of the airborne sound sensor position on the detectability of acoustic emissions during deep penetration laser welding. In *13. Mittweidaer Lasertagung*, 2024.

[66] Markus Omlor, Johannes Reith, Andreas Breitbarth, Cornelius Benedikt Hake, and Klaus Dilger. Inline Process Monitoring of Hairpin Welding Using Optical and Acoustic Quality Metrics. In *2022 12th International Electric Drives Production Conference, EDPC 2022 - Proceedings*. Institute of Electrical and Electronics Engineers Inc., 2022.

[67] Johannes Heilmeier, Michael K. Kick, Sophie Grabmann, Tatek Muschol, Franz Schlicht, Felix von Hundelshausen, Hans-Georg von Ribbeck, Tony Weiss, and Michael F. Zaeh. Inline failure detection in laser beam welding of battery cells: Acoustic and spectral emission analysis for quality monitoring. *Journal of Laser Applications*, 36(2), 5 2024.

[68] Andreas Krämer, Insa Henze, Ronald Pordzik, and Tim Radel. Inline detection of process anomalies during laser deep penetration welding of hidden T-joints. In *Procedia CIRP*, volume 124, pages 526–529. Elsevier B.V., 2024.

[69] Lazar Tomcic, Armin Ederer, Sophie Grabmann, Michael Kick, Johannes Kriegler, and Michael F. Zaeh. Interpreting acoustic emissions to determine the weld depth during laser beam welding. *Journal of Laser Applications*, 34(4), 11 2022.

[70] Christian Geiger, Pawel Garkusha, Christian Bernauer, Simon Mehrl, Pascal A. Schirmer, and Michael F. Zaeh. Acoustic process monitoring during the structuring of the diffusion media for fuel cells with Ultrashort Laser Pulses. *Procedia CIRP*, 124:51–56, 1 2024.

[71] Guiqian Liu, Xiangdong Gao, Deyong You, and Nanfeng Zhang. Prediction of high power laser welding status based on PCA and SVM classification of multiple sensors. *Journal of Intelligent Manufacturing*, 30(2):821–832, 2 2019.

[72] Yanxi Zhang, Deyong You, Xiangdong Gao, Nanfeng Zhang, and Perry P. Gao. Welding defects detection based on deep learning with multiple optical sensors during disk laser welding of thick plates. *Journal of Manufacturing Systems*, 51:87–94, 4 2019.

[73] Yanxi Zhang, Deyong You, Xiangdong Gao, Congyi Wang, Yangjin Li, and Perry P. Gao. Real-time monitoring of high-power disk laser welding statuses based on deep learning framework. *Journal of Intelligent Manufacturing*, 31(4):799 – 814, 4 2020.

[74] Deyuan Ma, Ping Jiang, Leshi Shu, and Shaoning Geng. Multi-sensing signals diagnosis and CNN-based detection of porosity defect during Al alloys laser welding. *Journal of Manufacturing Systems*, 62:334–346, 1 2022.

[75] Tine Brežan, Pasquale Franciosa, Matija Jezeršek, and Dariusz Ceglarek. Fusing optical coherence tomography and photodiodes for diagnosis of weld features during remote laser welding of copper-to-aluminum. *Journal of Laser Applications*, 35(1), 2023.

[76] Longchao Cao, Jingchang Li, Libin Zhang, Shuyang Luo, Menglei Li, and Xufeng Huang. Cross-attention-based multi-sensing signals fusion for penetration state monitoring during laser welding of aluminum alloy. *Knowledge-Based Systems*, 261:110212, 2 2023.

[77] Giovanni Chianese, Pasquale Franciosa, Tianzhu Sun, Dariusz Ceglarek, and Stanislao Patalano. Using photodiodes and supervised machine learning for automatic classification of weld defects in laser welding of thin foils copper-to-steel battery tabs. *Journal of Laser Applications*, 34(4):42040, 11 2022.

[78] Tianzhu Sun, Pasquale Franciosa, and Dariusz Ceglarek. Effect of focal position offset on joint integrity of AA1050 battery busbar assembly during remote laser welding. *Journal of Materials Research and Technology*, 14:2715–2726, 9 2021.

[79] S. Arzanpour, J. Fung, J. K. Mills, and W. L. Cleghorn. Flexible fixture design with applications to assembly of sheet metal automotive body parts. *Assembly Automation*, 26(2):143–153, 2006.

[80] Haibo He, Yang Bai, Edwardo A. Garcia, and Shutao Li. Adaptive Synthetic Sampling Approach for Imbalanced Learning. In *World Congress on Computational Intelligence*. IEEE, 2008.

[81] Tony Weiss, Jonas Werner, Christian Geiger, and Michael F. Zaeh. Acoustic process monitoring during the laser beam welding of stainless-steel foils using an adjustable ring mode laser beam source. *Journal of Laser Applications*, 36(4), 11 2024.

[82] Tao Ji and Norzalilah Mohamad Nor. Deep Learning-Empowered Digital Twin Using Acoustic Signal for Welding Quality Inspection. *Sensors*, 23(5), 3 2023.

[83] Wei Huang and Radovan Kovacevic. Acoustic monitoring of weld penetration during laser welding of high strength steels. *ICALEO 2009 - 28th International Congress on Applications of Lasers and Electro-Optics, Congress Proceedings*, 102:630–637, 11 2009.

[84] Alan V. Oppenheim. *Discrete-time signal processing*. Prentice Hall signal processing series. Pearson, Upper Saddle River, third edition. edition, 2010.

[85] Peter D. Welch. The Use of Fast Fourier Transform for the Estimation of Power Spectra: A Method Based on Time Averaging Over Short, Modified Periodograms. *IEEE Transactions on Audio and Electroacoustics*, 15(2):70–73, 1967.

[86] Hanchuan Peng, Fuhui Long, and Chris Ding. Feature selection based on mutual information: Criteria of Max-Dependency, Max-Relevance, and Min-Redundancy. *IEEE Transactions on Pattern Analysis and Machine Intelligence*, 27(8):1226–1238, 8 2005.

[87] A. Blug, F. Abt, L. Nicolosi, A. Heider, R. Weber, D. Carl, H. Höfler, and R. Tetzlaff. The full penetration hole as a stochastic process: Controlling penetration depth in keyhole laser-welding processes. *Applied Physics B: Lasers and Optics*, 108(1):97–107, 7 2012.

[88] Jonas Wagner, Christian Hagenlocher, Rudolf Weber, and Thomas Graf. The change of the absorptance at the transition from partial- to full-penetration laser welding. *International Journal of Advanced Manufacturing Technology*, 134(1-2):497–509, 9 2024.

[89] L. Li and W. M. Steen. Non-contact acoustic emission monitoring during laser processing. In *LIA (Laser Institute of America)*, volume 75, pages 719–728. Publ by Laser Inst of America, 1993.

[90] Wei Wei, Qiancheng Kong, Guichao He, Huaping Li, Jin Ren, Nianchun Deng, Zhaotao Chen, and Yu Long. A novel monitoring method based on the fusion of sound and image signals for laser welding penetration status. *Proceedings of the Institution of Mechanical Engineers, Part B: Journal of Engineering Manufacture*, 2024.

[91] Jie Li, Yi Zhang, Wen Liu, Bin Li, Xuni Yin, and Cong Chen. Prediction of penetration based on plasma plume and spectrum characteristics in laser welding. *Journal of Manufacturing Processes*, 75:593–604, 3 2022.

[92] Yiming Huang, Shanshan Li, Jiahui Li, Huabin Chen, Lijun Yang, and Shanben Chen. Spectral diagnosis and defects prediction based on ELM during the GTAW of Al alloys. *Measurement*, 136:405–414, 3 2019.

[93] Yi Zhang, Fazhi Li, Zhichao Liang, Yeyong Ying, Qida Lin, and Haiying Wei. Correlation analysis of penetration based on keyhole and plasma plume in laser welding. *Journal of Materials Processing Technology*, 256:1–12, 6 2018.

[94] Yi Luo, Liang Zhu, Jingtao Han, Jie Xu, Chengyang Zhang, and Dong Chen. Effect of focusing condition on laser energy absorption characteristics in pulsed laser welding. *Optics and Laser Technology*, 117:52–63, 9 2019.

[95] R D Rawlings and W M Smen. Acoustic emission monitoring of surface hardebing by laser. *Optics and Lasers in Engineering*, 2:173–188, 1981.

[96] Giovanni Chianese, Sharhid Jabar, Pasquale Franciosa, Dariusz Ceglarek, and Stanislao Patalano. A multi-physics CFD study on the part-to-part gap during remote laser welding of copper-to-steel battery tab connectors with beam wobbling. In *Procedia CIRP*, volume 111, pages 484–489. Elsevier B.V., 2022.

[97] Pasquale Franciosa, Armando Serino, Rehab Al Botros, and Darek Ceglarek. Closed-loop gap bridging control for remote laser welding of aluminum components based on first principle energy and mass balance. *Journal of Laser Applications*, 31(2), 5 2019.

[98] I. Bunaziv, X. Ren, and V. Olden. A comparative study of laser-arc hybrid welding with arc welding for fabrication of offshore substructures. In *Journal of Physics: Conference Series*, volume 2626. Institute of Physics, 2023.

[99] Wolfgang Fiedler, Alexander Drenker, and Stefan Kaierle. Process monitoring and control during hybrid laser-ARC welding of medium section steel sheets. *29th International Congress on Applications of Lasers and Electro-Optics, ICALEO 2010 - Congress Proceedings*, 103:78–84, 9 2010.

[100] Di Wu, Peilei Zhang, Haichuan Shi, Qinghua Lu, Zhishui Yu, and Yuze Huang. Advancements and prospects of OCT-enabled all-process monitoring and inline quality assurance in laser keyhole welding: A critical review, 10 2025.

[101] Christoph Mittelstädt, Thorsten Mattulat, Thomas Seefeld, and Markus Kogel-Hollacher. Novel approach for weld depth determination using optical coherence tomography measurement in laser deep penetration welding of aluminum and steel. *Journal of Laser Applications*, 31(2), 5 2019.

[102] M. Schmoeller, C. Stadter, S. Liebl, and M.F. Zaeh. Inline weld depth measurement for high brilliance laser beam sources using optical coherence tomography. *Journal of Laser Applications*, 31(2), 2019.

[103] Mikhail Sokolov, Pasquale Franciosa, Tianzhu Sun, Dariusz Ceglarek, Vincenzo Dimatteo, Alessandro Ascari, Alessandro Fortunato, and Falk Nagel. Applying optical coherence tomography for weld depth monitoring in remote laser welding of automotive battery tab connectors. *Journal of Laser Applications*, 33(1), 2 2021.

[104] Tobias Beck, Christoph Bantel, Meiko Boley, and Jean Pierre Bergmann. Oct capillary depth measurement in copper micro welding using green lasers. *Applied Sciences (Switzerland)*, 11(6), 3 2021.

[105] Matthias Werner, Jonas Wagner, Florian Ribbeck, Simon Hensel, Klaus Goth, Thomas Graf, and Gerson Meschut. Influence of the incident angle on the OCT measurement during remote laser beam welding. In *Procedia CIRP*, volume 111, pages 513–517. Elsevier B.V., 2022.

[106] Andrea Curatolo, Brendan F. Kennedy, David D. Sampson, and Timothy R. Hillman. Speckle in optical coherence tomography. *https://doi.org/10.1117/1.429925*, 4(1):95–105, 1 1999.

[107] Ruikang K. Wang and Zhenhe Ma. A practical approach to eliminate autocorrelation artefacts for volume-rate spectral domain optical coherence tomography. *Physics in Medicine & Biology*, 51(12):3231, 6 2006.

[108] Guanming Xie, Sanhong Wang, Yueqiang Zhang, Biao Hu, Yu Fu, Qifeng Yu, and You Li. An Efficient Method for Laser Welding Depth Determination Using Optical Coherence Tomography. *Sensors*, 23(11), 2023.

[109] Guohua He, Xiangdong Gao, Laiming Li, and Pengyu Gao. OCT monitoring data processing method of laser deep penetration welding based on HDBSCAN. *Optics and Laser Technology*, 179:111303, 12 2024.

[110] Martin Ester, Hans-Peter Kriegel, Jiirg Sander, and Xiaowei Xu. A Density-Based Algorithm for Discovering Clusters in Large Spatial Databases with Noise. *kddm*, pages 226–331, 1996.

[111] Kuk Jin Yoon and In So Kweon. Adaptive Support-Weight Approach for Correspondence Search. *IEEE Transactions on Pattern Analysis and Machine Intelligence*, 28(4):650–656, 4 2006.

[112] B. Ribic, T. A. Palmer, and T. DebRoy. Problems and issues in laser-arc hybrid welding. *International Materials Reviews*, 54(4):223–244, 2009.

[113] Guo Tang, Xu Zhao, Rendong Li, Ying Liang, Yishuai Jiang, and Hui Chen. The effect of arc position on laser-arc hybrid welding of 12-mm-thick high strength bainitic steel. *Optics & Laser Technology*, 121:105780, 1 2020.

[114] Ivan Bunaziv, Cato Dørum, Steen Erik Nielsen, Pasi Suikkanen, Xiaobo Ren, Bård Nyhus, Magnus Eriksson, and Odd M. Akselsen. Laser-arc hybrid welding of 12- and 15-mm thick structural steel. *International Journal of Advanced Manufacturing Technology*, 107(5-6):2649–2669, 3 2020.

[115] Simone Peli, Federico Bonaldo, and Marco Riva. Welding of 20 mm thick EH40 steel by means of a single-pass hybrid laser-arc welding technique. *Procedia CIRP*, 124:394–398, 1 2024.

[116] Torbjörn Ilar, Ingemar Eriksson, John Powell, and Alexander Kaplan. Root Humping in Laser Welding-an Investigation based on High Speed Imaging. *Physics Procedia*, 39:27–32, 2012.

[117] Dario Basile, Raffaella Sesana, Manuela De Maddis, Luca Borella, and Pasquale Russo Spena. Investigation of Strength and Formability of 6016 Aluminum Tailor Welded Blanks. *Metals 2022, Vol. 12, Page 1593*, 12(10):1593, 9 2022.

[118] Ahmad Aminzadeh, Joys Silva Rivera, Pedram Farhadipour, Anas Ghazi Jerniti, Noureddine Barka, Abderrazak El Ouafi, Fatemeh Mirakhorli, François Nadeau, and Marc-Olivier Gagné. Toward an intelligent aluminum laser welded blanks (ALWBs) factory based on industry 4.0; a critical review and novel smart model. *Optics and Laser Technology*, 167(December 2022):109661, 2023.

[119] Mariasofia Parisi and Guido Di Bella. Joining Technologies and Extended Producer Responsibility: A Review on Sustainability and End-of-Life Management of Metal Structures. *Metals 2026, Vol. 16, Page 49*, 16(1):49, 12 2025.

[120] Andrés Anca, Alberto Cardona, José Risso, and Víctor D. Fachinotti. Finite element modeling of welding processes. *Applied Mathematical Modelling*, 35(2):688–707, 2 2011.

[121] Gaizka Urretavizcaya Uranga, Maialen Areitioaurtena Oiartzun, Mario Javier Cabello, Carlos Molpeceres, and Miguel Morales. General Methodology for Laser Welding Finite Element Model Calibration. *Processes 2024, Vol. 12, Page 2687*, 12(12):2687, 11 2024.

[122] Yu Zhang and Tomasz Kik. Calibration of Heat Source Models in Numerical Simulations of Welding Processes. *Metals 2024, Vol. 14, Page 1213*, 14(11):1213, 10 2024.

[123] O. Murua, J. I. Arrizubieta, A. Lamikiz, and H. I. Schneider. Numerical simulation of a laser beam welding process: From a thermomechanical model to

the experimental inspection and validation. *Thermal Science and Engineering Progress*, 55:102901, 10 2024.

[124] T. R. Walker and C. J. Bennett. An automated inverse method to calibrate thermal finite element models for numerical welding applications. *Journal of Manufacturing Processes*, 47:263–283, 11 2019.

[125] Anand Mohan, Pasquale Franciosa, Dan Dai, and Dariusz Ceglarek. A novel approach to control thermal induced buckling during laser welding of battery housing through a unilateral N-2-1 fixturing principle. *Journal of Advanced Joining Processes*, 10:100256, 11 2024.

[126] Pasquale Russo Spena, Manuela De Maddis, Valentino Razza, Luca Santoro, Husniddin Mamarayimov, and Dario Basile. Infrared-Guided Thermal Cycles in FEM Simulation of Laser Welding of Thin Aluminium Alloy Sheets. *Metals 2025, Vol. 15, Page 830*, 15(8):830, 7 2025.

[127] An Wang, Yu-Cun Zhang, and Qun Li. Aluminium alloy emissivity correction model based on photon-phonon coupling and wavelength weight optimization. *Infrared Physics & Technology*, 154:106376, 3 2026.

[128] Eva S.V. Marques, Francisco J.G. Silva, and António B. Pereira. Comparison of Finite Element Methods in Fusion Welding Processes—A Review. *Metals 2020, Vol. 10, Page 75*, 10(1):75, 1 2020.

[129] H. Long, D. Gery, A. Carlier, and P. G. Maropoulos. Prediction of welding distortion in butt joint of thin plates. *Materials and Design*, 30(10):4126–4135, 12 2009.

[130] A. Vinoth and R. Sivasankari. Numerical Simulation Studies in Tungsten Inert Gas Welding of Inconel 718 Alloy Sheet. *Journal of Materials Engineering and Performance 2024 34:14*, 34(14):14832–14845, 10 2024.

[131] Ivica Kožar, Tea Rukavina, and Adnan Ibrahimbegović. Method of incompatible modes - Overview and application. *Gradjevinar*, 70(1):19–29, 2018.

[132] Frank Incorpera. Fundamental of Heat and Mass Transfer 7th Edition. *John Wiley & Sons*, 33(112):1–27, 2016.

[133] Xiaohu Tian, Juan Liao, Peng Cheng, and Yi Ling. Element Simulation of Welding Residual Stresses and Distortion in 5083 Incorporating Metallurgical Phase Transformation. pages 164–168, 11 2017.

[134] B. Schieck and H. Stumpf. Deformation analysis for finite elastic-plastic strains in a lagrangean-type description. *International Journal of Solids and Structures*, 30(19):2639–2660, 1 1993.

[135] Tiago R. Lima, Sérgio M.O. Tavares, and Paulo M.S.T. de Castro. Residual stress field and distortions resulting from welding processes: numerical modelling using Sysweld. *Ciência & Tecnologia dos Materiais*, 29(1):e56–e61, 1 2017.

[136] Tomasz Kik. Computational Techniques in Numerical Simulations of Arc and Laser Welding Processes. *Materials 2020, Vol. 13, Page 608*, 13(3):608, 1 2020.

[137] Anoop K. Unni and M. Vasudevan. Computational fluid dynamics simulation of hybrid laser-MIG welding of 316 LN stainless steel using hybrid heat source. *International Journal of Thermal Sciences*, 185:108042, 3 2023.

[138] Francesco Raffaele Battista, Giuseppina Ambrogio, Luca Giorgini, Massimo Guerrini, Stefano Costantino, Filippo Ricciardi, and Luigino Filice. Prediction of the keyhole TIG welding-induced distortions on Inconel 718 industrial gas turbine component by numerical-experimental approach. *The International Journal of Advanced Manufacturing Technology 2024 134:9*, 134(9):4593–4608, 9 2024.

[139] Javier A. Vargas, Jaime E. Torres, Jovanny A. Pacheco, and Roque J. Hernandez. Analysis of heat input effect on the mechanical properties of Al-6061-T6 alloy weld joints. *Materials & Design (1980-2015)*, 52:556–564, 12 2013.

[140] Boonrit Keawprachum and Pornsak Srisungsitthisunti. Real-time process monitoring of laser welding by infrared camera and image processing. *Key Engineering Materials*, 856 KEM:160–168, 2020.

[141] Xin Li and Yan Ma. A method for simplified modeling and capacity, state of charge, current distribution analysis based on arbitrary topology connection battery pack. *Journal of Energy Storage*, 57:106206, 1 2023.

[142] BMW. Press Kit BMW Group Production.

[143] Gorti Janardhan, Goutam Mukhopadhyay, and Krishna Dutta. Failure behaviour of Spot-welds on automotive steel sheets. *Materials Today: Proceedings*, 62(P10):6120–6124, 1 2022.

[144] Trans Adriatic Pipeline. TAP Offshore Pipeline Construction (project factsheet).

[145] Saipem. Offshore Pipelines (Saipem brochure).

[146] Typical repair rates for welded products - TWI.